Millimeter-Scale and Energy-Efficient RF Wireless System

by

Yao Shi

A dissertation submitted in partial fulfillment
of the requirements for the degree of
Doctor of Philosophy
(Electrical Engineering)
in The University of Michigan
2018

Doctoral Committee:

Professor David Blaauw, Co-Chair
Associate Professor David Wentzloff, Co-Chair
Associate Professor Nikolaos Chronis
Assistant Professor Hun-Seok Kim

Yao Shi

yaoshi@umich.edu

ORCID iD: 0000-0001-6235-5091

To all the people in my life

TABLE OF CONTENTS

LIST OF FIGURES

Figure

ABSTRACT

This dissertation focuses on energy-efficient RF wireless system with millimeter-scale dimension, expanding the potential use cases of millimeter-scale computing devices. It is challenging to develop RF wireless system in such constrained space. First, millimeter-sized antennae are electrically-small, resulting in low antenna efficiency. Second, their energy source is very limited due to the small battery and/or energy harvester. Third, it is required to eliminate most or all off-chip devices to further reduce system dimension. In this dissertation, these challenges are explored and analyzed, and new methods are proposed to solve them. Three prototype RF systems were implemented for demonstration and verification. The first prototype is a 10 mm^3 inductive-coupled radio system that can be implanted through a syringe, aimed at healthcare applications with constrained space. The second prototype is a 3x3x3 mm^3 far-field 915MHz radio system with 20-meter NLOS range in indoor environment. The third prototype is a low-power BLE transmitter using 3.5x3.5 mm^2 planar loop antenna, enabling millimeter-scale sensors to connect with ubiquitous IoT BLE-compliant devices. The work presented in this dissertation improves use cases of millimeter-scale computers by presenting new methods for improving energy efficiency of wireless radio system with extremely small dimensions. The impact is significant in the age of IoT when everything will be connected in daily life.

CHAPTER I

Introduction

1.1 Evolution of Computer and Emerging Applications

Computing devices has changed our lives significantly over the past several decades. In 1972, Golden Bell defined a computer class as a cluster of computing devices that share a similar structure, technology, cost and dimension [8]. Bell's Law states that a new computer class forms roughly every decade, with new classes resulting in new applications and new industries. The evolution of computer classes over time has shown a 100x reduction in the volume of computing devices per decade since the mainframe computers of the 1960s, as in Figure 1.1. This miniaturization of computing devices aligns well with Bell's Law. According to this trend, the next generation of computing devices will be millimeter-scale in terms of system volume and able to perform functions in diverse emerging applications.

Millimeter-scale computers, also known as smart dusts or smart motes [3], are very tiny in volume and thus can be deployed in a large number, forming a wireless sensor network when connected through wireless communication. Meanwhile, they could connect with other computer classes such as smart phones, wearable devices, or gateways, moving us one step forward with respect to the Internet of Things (IoT) [4]. Moreover, the application space of such millimeter-scale computing systems is unlimited and appealing.

A millimeter-scale computer can be deployed in circumstances where the space is constrained, such as in healthcare or biomedical applications. Here are several examples: 1) an intraocular pressure monitor with 1.5mm^3 fits into the eye, allowing real-time detection of eye diseases, such as glaucoma [14]; 2) a tiny system that can be injected through a 14-gauge syringe needle (inside diameter is 1.55mm) makes implantation surgery much less invasive [16] [59]; 3) a miniaturized system with chemical and molecular sensors or drug-delivery actuators implanted in the inner ear can help with the diagnosis and treatment of hearing loss and other disorders [50]; 4) a millimeter-scale implanted neural sensor with wireless communication enables a long-term and more robust brain-machine interface [51]. Beyond those space-constrained applications, a millimeter-scale computer could bring benefits to daily life with emerging applications. For example, a millimeter-scale and almost invisible GPS logger would make small objects trackable [38]. Beyond tracking, such systems could monitor environmental conditions, providing interfaces with humans, and perform efficient local computing. Such possibilities motivate the research efforts focused on the development of millimeter-scale computers from various perspectives (systems, circuits, devices, antennas and etc.).

1.2 Advances in Millimeter-scale Computers

The concept and idea for millimeter-scale computers, also known as smart dusts, was proposed by scholars at the University of California, Berkeley around the year 2000 [3] [65]. Since then, it has been a promising research area. The true breakthrough was made by scholars from the University of Michigan, where complete and systematic studies on millimeter-scale computers were conducted [23] [13] [14] [44]. The resulting computing system is called the Michigan Micro Mote (M^3), which is considered the worlds smallest computer and is now exhibited in the Computer History Museum in California. Besides M^3, there have been other works presented by other universities

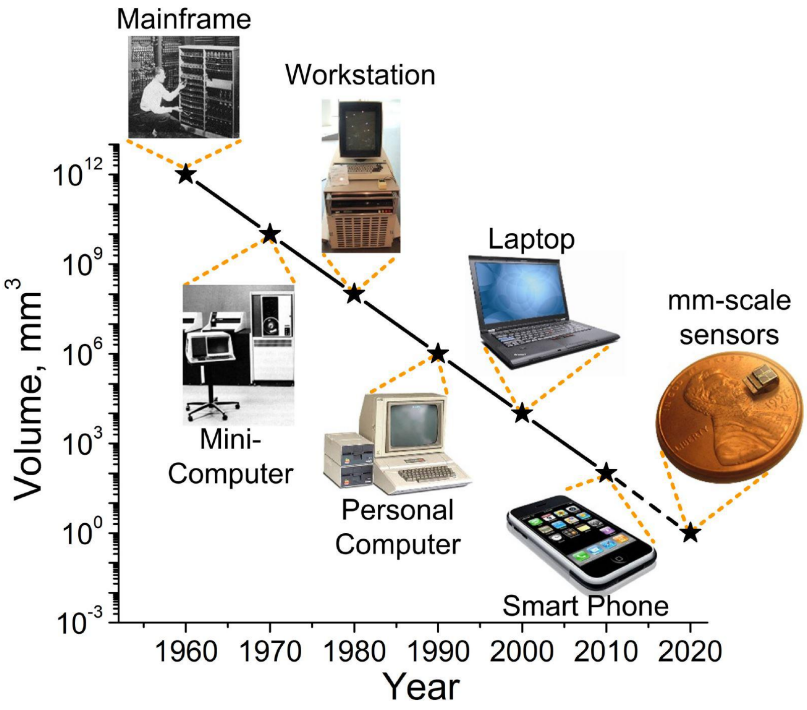

Figure 1.1: Evolution of computers shows 100x volume reduction of computing devices per decade

or research institutes [66] [63] [31].

The development of millimeter-scale computers is possible thanks to research focused on designing novel, ultra-low-power, area-efficient integrated circuit in state-of-the-art semiconductor technologies [7] [43] [53] [39] [34] [68] [36]. For the M^3, the chips (less than 1mm x 2mm in size) are stacked and connected together through wire bonding technology, as shown in Figure 1.2. The complete system consists of multiple functional layers, such as solar cells, rechargable thin-film batteries, microprocessor, various types of sensors, memory and a radio (wireless communication).

Among the functional layers in a computing device, the radio frequency (RF) layer for wireless communication is one of the most important ones because it is critical for data exchange with other devices in a wireless network. Its communication range determines the use cases of computing devices. Obviously, a long range is desired. However, a long range is accompanied by higher energy consumption, presenting extreme challenges for the power budget of a millimeter-scale system with a very

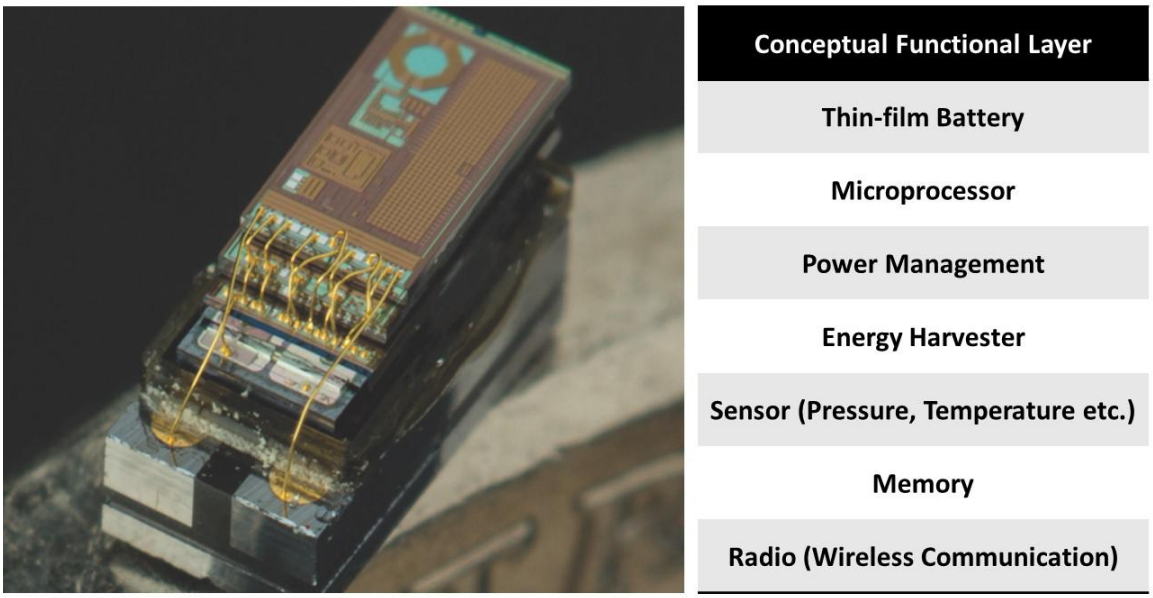

Figure 1.2: Michigan Micro-Mote:a complete millimeter-scale computing system containing multiple functional layers

limited energy source [41]. Moreover, RF communication usually dominates system power consumption compared to other circuit blocks [37] [22]. Therefore, a low-power RF block in a system would improve system lifetime significantly.

1.3 Millimeter-scale RF Wireless Systems

This dissertation focuses on RF wireless system for millimeter-scale computer. To integrate into such small form factor, the hardware for RF system must be miniaturized as well, resulting in unique challenges and special considerations.

1.3.1 Communication Link

As shown in Figure 1.3, a communication link can be categorized as asymmetrical or symmetrical. In an asymmetrical link, the two wireless nodes have different power budgets and system volumes and thus different processing and communication

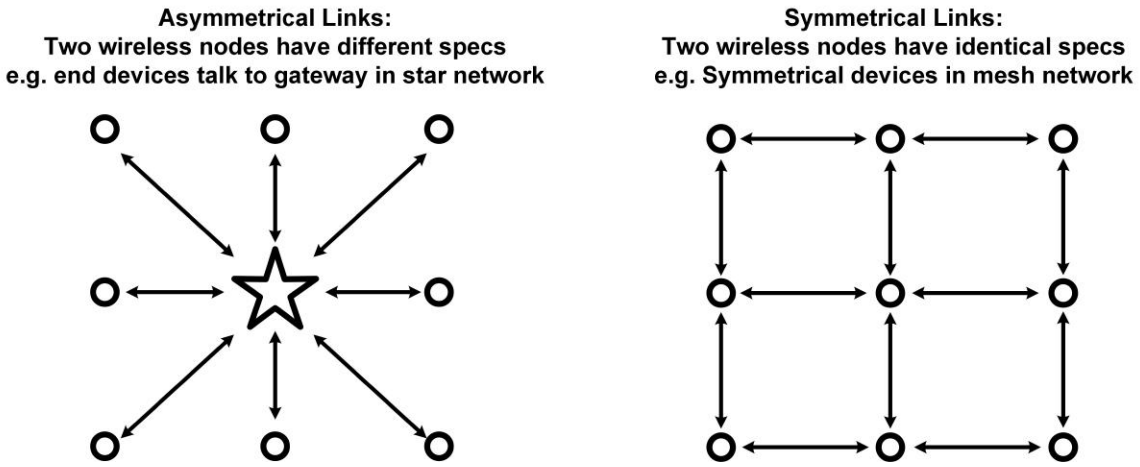

Figure 1.3: Asymmetrical and symmetrical links shown in general wireless networks

abilities. Commonly, asymmetrical links are utilized in a star network, where a large number of end devices talk to a single hub or gateway. Thanks to the asymmetric nature, a millimeter-scale wireless sensor node can be designed to have weaker receiver sensitivity or transmitter output power than the gateway, resulting in lower power consumption for the millimeter-scale node. Moreover, a high-power geteway can assist the synchronization with a crystal-less millimeter-scale radio and perform calibration of carrier frequency or symbol frequency offset, enabling power reduction and volume reduction of millimeter-scale computers. Conversely, a symmetrical link is established between two nodes with identical performances, which is mostly seen in a mesh network. The asymmetrical link is utilized in the proposed designs in this dissertation.

The general organization of the radio layer in a wireless node or a computing devices is shown in Figure 1.4. It consists of an antenna, matching network and transceiver (RF front-end and baseband processor). In modern radio implementation, the transceiver and matching network are realized by integrated circuit (chip) with many off-chip electronic components. Scaling of semiconductor technology makes it possible to fabricate a transceiver chip as small as several millimeters.

However, off-chip components often dominate the overall system volume. To realize millimeter system volume, off-chip components should be eliminated as many as possible. For example, antennas are usually off-chip since on-chip antennas suffer from significant loss due to low resistivity of silicon substrate, which is usually less than $10\Omega \cdot cm$ [6]. In this work, custom designed millimeter-scale antennas are fabricated using technology such as printed circuit board or glass substrate instead of semiconductor technology to achieve a decent communication range. Other off-chip components are mainly passive devices such as capacitor and inductor, which must be off-chip if the value is too large to integrate into the chip. For example, as a rule of thumb, capacitors larger than 10 nF and inductors larger than 1 μH can only be implemented as off-chip components. Moreover, off-chip crystals as an accurate frequency reference are critical in wireless systems, mainly for two purposes: 1) calibration of RF local oscillator (LO) center frequency by phase-locked loop and 2) as timing clocks for baseband processing [54]. For example, Bluetooth standards specify that the baseband clock accuracy should be better than 50 ppm across all environmental variations [10]. Until now, crystal references have been the best candidates due to their commercial availability. Unfortunately, crystal dimensions are bulky, with dimensions larger than 1x1 mm^2. One alternative approach is to use an MEMS resonator as reference. But access to MEMS devices is very limited. In this work, the crystal is eliminated by proposing a custom communication method that enables the usage of an on-chip CMOS timer with lower accuracy than a crystal oscillator.

1.3.2 Millimeter-scale Antenna and Carrier Frequency

There are many unique challenges for millimeter-scale systems. One such challenge is that the antenna dimension is strictly constrained to several millimeters. Because this dimension is much smaller than the wavelength below 10 GHz, the antenna gain is very poor, limiting the maximum achievable communication range, which is one

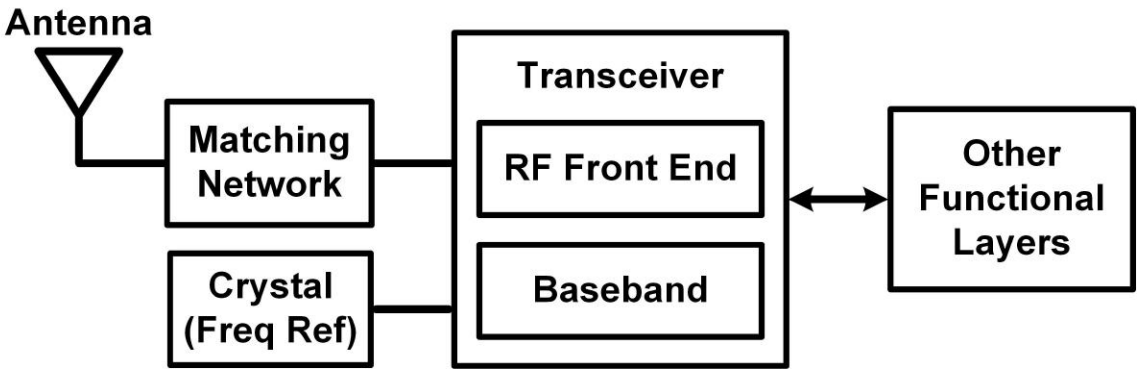

Figure 1.4: Organization of radio layer in a wireless sensor node

of the most critical properties for millimeter-scale computers deployed in real-life applications. The communication range depends on the path loss and antenna gain given a specific transmitter output power and receiver sensitivity. Besides antenna gain, the path loss is also highly dependent on the carrier frequency. The famous Friis equation quantifies the relationship between wavelength and path loss:

$$\frac{P_(R)}{P_(T)} = \frac{A_R A_T}{d^2 \lambda^2} \tag{1.1}$$

where P_R is the received power, P_T is transmitted power, d is communication distance, λ is wavelength of the radio frequency, A_R and A_T are receiver and transmitter antenna gain respectively [24]. It is worth noting that Equation (1.1) is valid for free-space far-field radiation. Other modified equations are required for different conditions. For example, in an indoor environment where radio propagation experiences more attenuation due to obstacles and blockage, ITU indoor propagation model quantifies the path loss more accurately [58].

Given the above knowledge, one key point of this work is that the antenna and carrier frequency are co-optimized to achieve the optimum communication range given the antenna dimension. In chapter II, a near-field implantable radio is presented where frequency and antenna are co-optmized to achieve optimum communication range. In

chapter III, ITU indoor model is utilized to optimize the carrier frequency for a 3x3x3 millimeter-scale sensor node deployed in indoor environment.

1.3.3 Range: Near- and Far-field Regions

The Friis transmission equation and ITU indoor model apply to far field radiation. But near-field communication proves useful in certain applications such as card reader or implanted sensor. Antenna field regions can be divided into near-field and far-field based on the distance between the radiation source or the transmitting antenna [29][52]. For near-field communication, the electromagnetic field is reactive or inductive instead of radiative, and the power strength is decreased by an inverse fourth-power (static field) and sixth-power (inductive field). Beyond the boundary, (1.1) shows that the power at the terminal of receiver antenna decreases by the inverse-distance squared in free space. For electrically-small antennas whose dimension are much less than the wavelength, the boundary is commonly given as $\lambda/2\pi$[52]. The antenna regions and boundary expression are shown in Figure 1.5. Based on the antenna boundary, we can categorize radio system into near-field and far-field radio. A near-field implantable radio utilizing inductive-coupling link is presented in chapter II. Two far-field radios, one at 915MHz and one at 2400MHz, are described in chapter III and chapter IV, respectively.

1.3.4 Antenna and Circuit Co-design

From the perspective of circuit design, antenna impedance is a critical consideration for transceiver design. In general, the interface between transceiver circuits and antenna is the matching network as shown in Figure 1.4. The matching network performs impedance transformation. At radio frequency, due to electromagnetic wave effect, impedance matching is necessary to ensure signal is not reflected back at the interface between circuit and antenna. In most actual applications, for an antenna

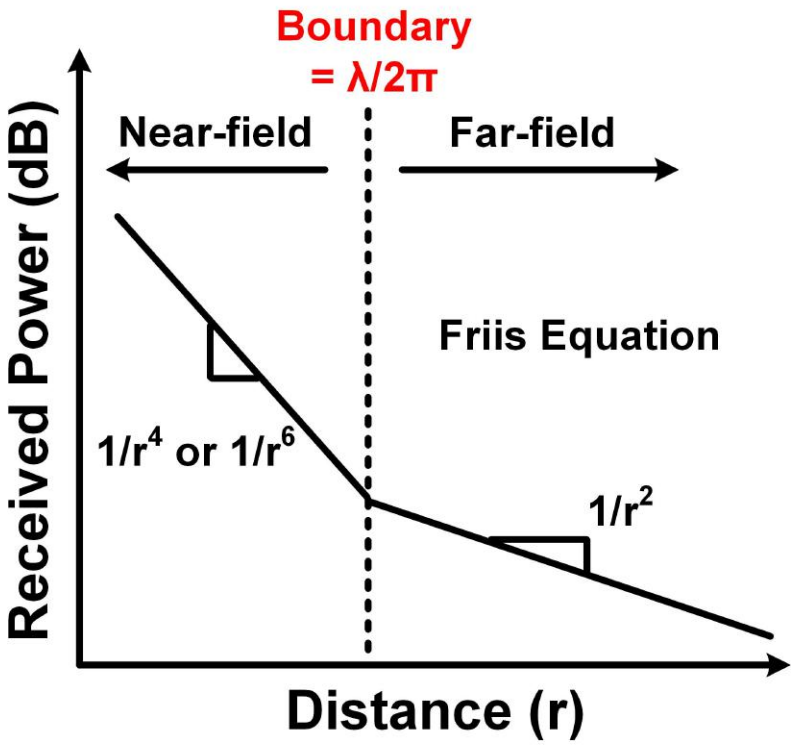

Figure 1.5: Near-field and far-field regions of a transmitting antenna

and RF transceiver package placed on the same circuit board, the distance could be long compared to the wavelength. It is common sense for antenna manufacturers to build antennas with 50Ωat the desired frequency and for RF board designers to build transmission lines with 50Ωcharacteristic impedance. Thus, RF transceiver is assumed to interface with 50Ωtransmission line. However, for millimeter-scale systems, the antenna and transceiver chip are physically spaced by approximately 1 millimeter (length of bonding wire) such that the RF signal wavelength is below 10 GHz, making it unnecessary to design antennas and matching network for 50Ω. Given this special circumstance, antenna and transceiver co-design would result in better overall RF efficiency within millimeter-scale system. Magnetic antennas and co-designed circuits are proposed in this dissertation, as shown in Figure 1.6. In transmitter, magnetic antenna and parallel capacitor functions as resonator for RF generation,which is called power oscillator. Theoretical analysis of such power oscillator is shown in

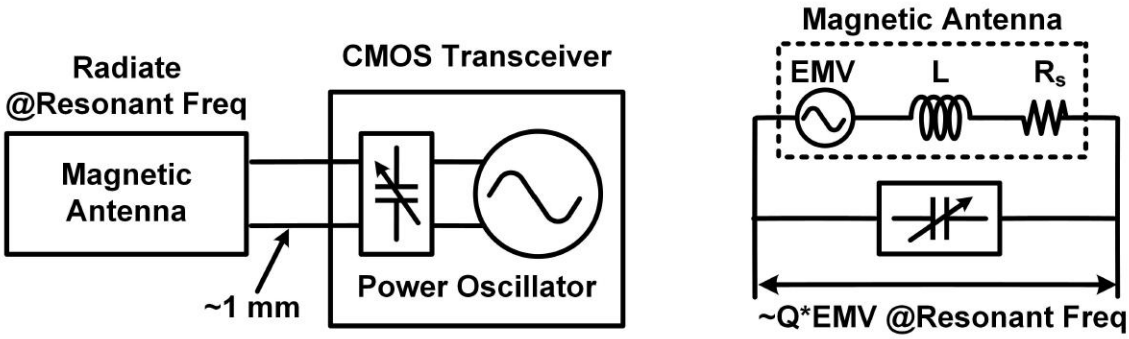

Figure 1.6: Co-design of magnetic antenna and front-end circuits: transmitter (left) and receiver (right)

Section 4.3.2. In receiver, quality factor of the resonator provides passive gain for received signal at magnetic antenna.

1.3.5 Energy and Power Constraint

Another challenge is the extreme energy and power constraints imposed on the millimeter-scale systems. For better integration with other chips, a Cymbet thin-film lithium battery with 1x2.2 mm^2 in size and 0.2mm thickness is used in a stacked millimeter-scale system [13]. However, its energy capacity is only 2 μAh. Moreover, its peak power is less than 50 uW due to the high intrinsic resistance. These limitations present a challenge in designing radio transceiver circuits due to battery sourcing limitations. For transceivers consuming more power, millimeter-scale batteries with larger dimension could be used, resulting in system size to approach $1cm^3$. For example, a Seiko cell battery with size of 4.8x4.8 mm^2 has 1mAh capacity and only 100 Ω internal resistance. To solve those issues, circuit or system power reduction techniques have to be implemented. Bit-level duty-cycled pulsed transmission is utilized to solve the issue of peak power limitation in designs proposed in chapter II and chapter III. Moreover, system level duty cycling at packet level is used in all the proposed designs.

1.4 Wireless Communication Protocols

A communication standard defines radio physical layer specifications, packet organization and synchronization method between wireless nodes in a network. There are many communication standards suitable for energy-efficient wireless system, such as cellular, WiFi, Bluetooth, RFID, NFC, LPWAN and Zigbee. There are also standards designed for certain applications such Wireless Body Area Network (WBAN) and Medical Implant Communication Service (MICS). Each standard represents a trade-off between power consumption, range, and bandwidth, and each has its own limitations. For example, RFID or NFC features passive sensor node transceiver, limiting the communication range. Thus, the selection should be based on requirement of application. Some popular standards are summarized in Table 1.1. It is clear that most IoT radios utilize carrier frequencies lower than 10 GHz, mainly because a radio with such as frequency has better non-line-of-sight performance than a millimeter-wave radio.

	Frequency Band (MHz)	Data Rate (kbps)	Target Range
WiFi	2400,5000	54000,450000	Long
Bluetooth	2400	1000,2000	Medium
Zigbee	2400	250	Long
	868	20	Long
NFC	13.56	106,212,424	Short
MICS	402-405	100	Short

Table 1.1: Typical communication standards for energy-efficient wireless.

Beyond those communication standards, custom communication protocols are also possible and prove useful such as the following: 1) when power consumption exceeds system budget in order to comply standard requirements such as center frequency accuracy and interference rejection; 2) when carrier frequency is not optimum based on antenna specifications and link budget; and 3) when the existing standards either specify an unnecessarily high data rate or are not able to meet data rate requirement of application. However, the choice of carrier frequency and radiation power must

be compliant to Federal Communications Commission (FCC) requirements [20]. The most popular frequency bands for custom protocols are located at the industrial, scientific and medical (ISM) radio bands, especially 915MHz and 2400MHz. In this work, a custom sensor initiation synchronization is proposed to eliminate crystal reference, as described in II and chapter III.

1.5 Dissertation Contribution and Organization

This work contributes to the development of millimeter-scale and energy-efficient wireless systems that solve the challenges described in Section 1.3. This dissertation presents three works in detail.

In Chapter II, I present an inductive-coupled near-field radio for a 10 mm^3 sensor node that is implantable through a 14-gauge syringe needle. An asymmetric inductive link was modeled and optimized for maximum range given limited antenna dimension. The carrier frequency and antenna were designed based on optimization results. We demonstrate energy-efficient active near-field wireless communication between the millimeter-scale sensor node and a base station device through RF energy-absorbing tissue. The wireless transceiver, digital baseband controller, wake-up controller, on-chip baseband timer, sleep timer, and MBUS controller are all integrated on a single chip. In transmitter, a novel pulse-inject H-bridge power oscillator was proposed and co-designed with proposed magnetic antenna, achieving 1.67x efficiency. A 1x8 mm^2 antenna printed on glass substrate and an 11x11 cm^2 base station antenna printed on FR4 circuit board are co-designed to form an asymmetric inductive link between the sensor node and base station. The transceiver, co-designed with the 1x8 mm^2 sensor antenna, consumes 43.5 μW average power at 2 kbps, while the receiver power consumption is 36 μW with -54 dbm sensitivity at 100 kbps. The radio can operate on a millimeter-scale battery that has a stringent 50 μW peak power constraint. The system was measured to achieve a range of 50 cm for the sensor transmitter and 20

cm for receiver. This work enables wireless communication for the implanted smart devices, increasing their potential use cases in healthcare applications.

In Chapter III, we present a 915MHz asymmetrical radio co-designed with a 3D loop antenna, integrated within a 3x3x3mm sensor node, demonstrating stand-alone bi-directional 20m NLOS wireless communication with variable data rates of 30bps to 30.3kbps for TX and 7.8kbps to 62.5kbps for RX. First, by simultaneously considering the magnetic dipole efficiency, frequency-dependent path loss, and wall penetration loss, we found that a 915MHz carrier frequency is optimal for a 3x3x3mm sensor node in NLOS asymmetric communication with a gateway. Second, for far-field radiation, we found that a magnetic dipole antenna achieves better efficiency at an electrically-small size than an electric dipole, when the antennas are resonated with off-chip lumped components. In addition, the high reactive part of electrically-small electric dipoles (4k compared to 10 for the magnetic antenna) requires an impractically large off-chip inductor to resonate. Third, the transmitter is co-designed with loop antenna, generating -26.9 dBm equivalent isotropically radiated power (EIRP) consuming 2 mW power with 32% effiency. Finally, a sparse pulse position modulation (PPM) combined with a sensor-initiation communication protocol shifts the power-hungry calibration of frequency offset to the gateway, enabling crystal-free radio design.

In Chapter IV, I present an energy-efficient Bluetooth Low Energy (BLE) transmitter that is co-designed with 3.5x3.5 mm^2 planar loop antenna. I proposed and designed a digitally controlled power oscillator (DCPO) incorporating a high-Q resonator to perform frequency generation and power delivery into antenna. A transformer-boost technique was proposed for the DCPO to achieve 1.2x output power level and 3.16x transmit efficiency compared to conventional fashion. A high-Q digitally controlled capacitor array (Q: 283 to 404) resonates with a high-Q loop antenna around 2.4GHz. Beyond high Q, its resolution and total range was designed to meet BLE specifications. By implementing a duty-cycled all-digital phase-locked loop (ADPLL),

open-loop GFSK modulation was realized to reduce overall energy consumption. The fully wireless system demonstrated 7-meter range communication to any commercial phone.

CHAPTER II

A 10 mm^3 Inductive-Coupled Near-Field Radio for Syringe-Implantable Sensor Node

2.1 Introduction

Implantable smart devices are gaining attention due to their potential uses in medical and healthcare applications that aim to improve the quality of human life. Beyond well-known applications such as pacemakers [2] and cochlear implants [71], we envision millimeter-scale smart implantable devices that can perform long-term sensing, local computation, real-time actuation, and data transfer. As shown in Figure 2.1, there has been a continuous trend to shrink the volume of implantable pacemakers [40]. While their volume has been reduced dramatically, their minimum size still remains around 1 cm^3, a size that requires invasive and more risky surgery for implantation. Meanwhile, passive RF tags are available with a much smaller volume approximately 12 mm^3 (a 83x volume reduction). These small devices can be implanted through a syringe needle, minimally affecting a patients everyday life. However, these implantable radio-frequency identification (RFID) tags are passive devices that are only powered when a reader is in proximity. This lack of an integrated power source makes RFID devices incapable of performing the complicated duties that we envision for implantable smart devices. In addition, injectable microstimulators

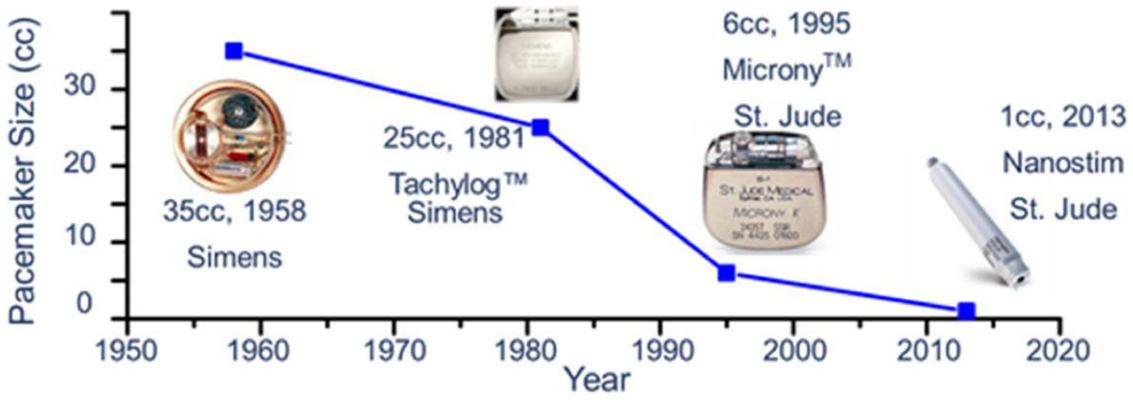

Figure 2.1: The long-term trend of implantable pacemaker size over years.

have been presented with active functions including neuromuscular stimulation and data communication [46] [72] [64]. However, to support complicated active operations, those implants typically incorporate a large chip, many off-chip components and a bulky battery, hindering further miniaturization.

The goal of this work is to enable the development of implantable smart devices that are much smaller than 1 cm^3 but still have the ability to perform autonomous medical functions with a restricted local power source. This idea has driven the proposed syringe-implantable smart sensor node, whose conceptual configuration is shown in Figure 2.2. The system is constructed from several layers (chips) that are stacked and connected through wire bonding [44]. The thickness of each layer is approximately 100 μm. All layers, including the radio, a processor, a thin-film battery and other peripherals, such as sensor layer and power management layer, are implemented with fully-integrated circuits eliminating external, off-chip components which allows reduction in size. Furthermore, compared to placing all circuits in single large chip [5-6], the stack based integration scheme reduces overall system volume and enables increased system functionality [44]. The sensor node's overall 1x1x10 mm^3 form-factor is specifically tailored to make it implantable through a 14-gauge syringe needle, eliminating the need for surgery. There has been continual research to realize a

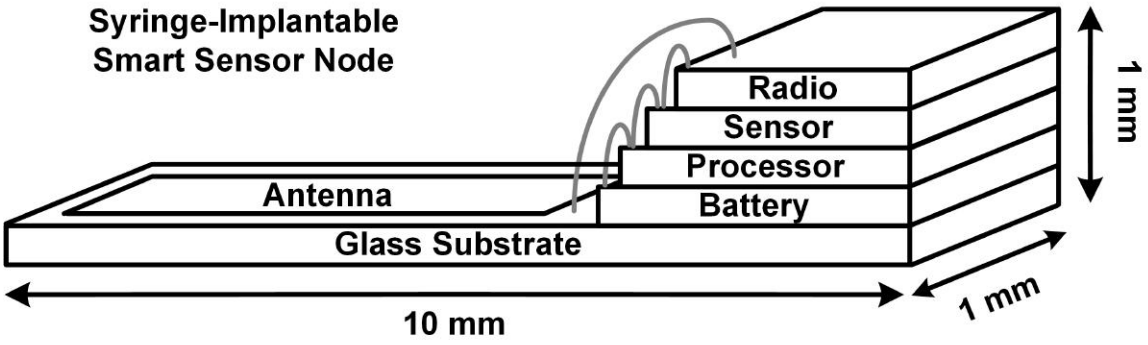

Figure 2.2: The targeted syringe-implantable smart sensor node with proposed radio and other functional layers.

millimeter-scale ultra-low power (ULP) sensor system with multiple functional layers powered by a thin-film battery [23] [16]. This work introduces a new solution to enable long distance ($>$ 20 cm) near-field communication between these millimeter-scale ULP wireless sensor nodes and a base station through tissue.

There are many unique challenges for a radio system that is constrained to a millimeter-scale syringe-implantable form factor. To fit into a syringe needle, the antenna dimension is strictly constrained to a millimeter or less in width. Because this dimension is much smaller than the wavelength (e.g., 3 m for 100 MHz), the antenna gain is very poor. In addition, the RF wireless communication link distance is significantly constrained by the severe signal loss in electromagnetic field-absorbing tissue. A third major challenge is the extreme energy and power constraints imposed on the system. A thin-film battery limited in size to 1x2.2 mm^2 provides only 2 μAh. Moreover, its peak power is less than 50 μW due to the high intrinsic resistance. These limitations present a challenge in designing radio transceiver circuits, which typically consume $>$ 100 μW active power. Addressing these challenges is the topic of this work. A number of works have been presented on ultra-small implanted radios. Backscattering, in which the passive radio in a sensor node reflects an incoming signal from a base station or a reader, is the most common method used to

realize ultra-low power consumption [47][69]. These works consume approximately 1 μW with a small system volume, on the order of several cubic millimeters. However, backscattering suffers from reader self-jamming, limiting the communication range to less than 3.5 cm [47][69]. Wirelessly powered sensor nodes that achieve longer communication distances exist (e.g., [60]), but they typically require bulky off-chip passive components that do not fit in the millimeter-scale form-factor. In contrast, active radios can support significantly longer ranges [14][11] with a smaller volume. In [14], a 1.5-mm^3 complete system with an active transmitter was reported. However, this design only includes a transmitter, and its active power consumption is rather high (45 mW). An active transceiver with an On-off Keying (OOK) transmitter and super-regenerative receiver is proposed in [11] to obtain a range greater than 10 cm. However, the system is co-designed with a 2.3 cm x 2.4 cm loop antenna that is unacceptable for a millimeter-scale system. We propose three techniques by which to realize an ULP millimeter-scale implanted sensor node communication system: 1) a co-designed, asymmetric magnetic antenna pair on the implanted sensor node and the base-station device, 2) a pulse-inject H-bridge oscillator with improved efficiency that replaces a conventional constant-bias cross-couple oscillator [14][11], and 3) a new sensor-initiated synchronization protocol in which timing offset estimation is performed on the base station, eliminating the need for an area-demanding off-chip crystal and synchronization baseband processing on the sensor node and thereby significantly improving its energy efficiency. Combining these techniques, the proposed system achieves a link distance up to 50 cm for sensor TX and 20 cm for sensor RX through 3 cm of tissue. The system fully integrates the transceiver, baseband controller, timer, wakeup controller and MBUS controller [37] on a single chip together with a millimeter-scale magnetic antenna fabricated on a glass substrate [59].

2.2 Overview of System

2.2.1 System Overview

Figure 2.3 is a photo of the proposed radio system that fits inside a 14-gauge syringe needle. Syringe implantation constrains the width of the system to approximately 1 mm, whereas the length can be significantly more than 1 mm. Note that it is the antenna, rather than the radio chip, that dominates the overall system volume. The sensor nodes magnetic antenna is 1x8 mm^2 in size and is printed on top of the 100-μm-thick glass substrate. The radio chip is designed to be 1 mm wide to fully utilize the available area yet fit into the syringe. The chip sits on the same glass substrate and is connected to the antenna by wire-bonding. It is worth mentioning that Figure 2.3. shows proposed radio, which is the focus of this work, rather than the target sensor node. Complete system requires the integration with other functional layers (processor, thin-film battery, power management unit and other peripherals) by die-stacking and wire bonding [44], which will increase size of the system by approximately 0.5mm in height (width and length would remain essentially the same). Moreover, hermetic encapsulation (e.g. glass capsule) of the overall system is necessary for final implantation [46][72] and would add approximately 400 μm to each dimension. If so, a final packaged sensor node is expected to fit into a 13-gauge needle, which has inner diameter of 1.8mm.

Figure 2.4 shows the system block diagram. The proposed radio for the sensor node exchanges data with the base station through near-field inductive coupling, which is a common method for through-tissue communication. It is worth noting that the antennas on the millimeter-scale sensor node and the base station have dissimilar dimensions that are co-designed to enhance coupling strength. The antenna dimension on the sensor node is 1x8 mm^2, whereas the base station antenna size is 11x11 cm^2. The bi-directional link between the sensor node and the base station

Figure 2.3: Proposed millimeter-scale radio system within a syringe needle on top of a one-cent coin.

utilizes asymmetric carrier frequencies; 112 MHz for sensor node TX (i.e., uplink) and 49.86 MHz for sensor node RX (i.e., downlink). Justification for this asymmetric link design will be discussed in Section III. In the SoC, the power oscillator in the pulsed transmitter operates directly from the battery (4.1 V), whereas other blocks, including transmitter (except power oscillator), receiver, baseband controller, on-chip timer, wakeup controller and sleep timer, operate on 1.2 V supply. Since this radio SoC is designed to be integrated with other functional layers (e.g., the processor, sensor, etc.), a power management unit [35] on one of the system layers generates the global 1.2V supply, which is down-converted from battery supply. In the target ultra-low power sensor node with a stack of multiple layers, the designed radio can exchange data and command with other layers via an MBUS interface [37].

2.2.2 Sensor-Initiated Synchronization

Timing synchronization is a critical part of the wireless sensor communication. Generally, timing synchronization is performed at the receiver using digital baseband signal processing to estimate and compensate for the symbol timing and baseband sampling frequency offsets. The timing synchronization complexity depends on the

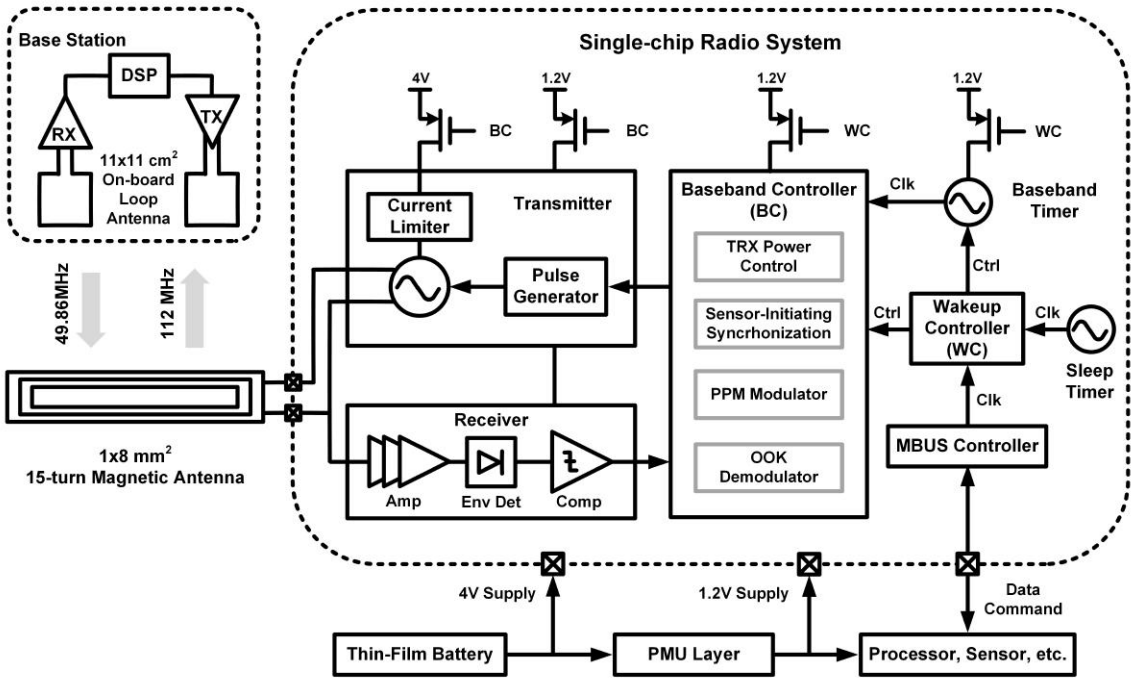

Figure 2.4: Proposed single-chip radio system with an 1x8 mm^2 glass substrate antenna for wireless communication between sensor node and base station.

mismatch between the transmitter and the receiver baseband clocks. Conventionally, an accurate baseband clock is realized by using a phase lock loop (PLL) with an accurate frequency reference. A typical frequency reference is a quartz crystal, which is not feasible for millimeter-scale sensor nodes due to its large volume. Alternatively, an on-chip timer can be used to reduce the system volume [18]. However, its frequency accuracy is significantly worse than that of a crystal oscillator, which means the baseband must search for a wider frequency offset, causing high power consumption in the digital baseband circuits. In conventional wireless sensor nodes, a low-power wakeup receiver is always powered on and listens for the initiation packet [18]. However, if a low-accuracy on-chip timer is used, system power is dominated by baseband circuits, making it impractical to realize communication with a wakeup receiver in millimeter-scale sensor nodes. As shown in Figure 2.5, we propose a new energy-efficient sensor-initiated synchronization scheme. Since the base station can

be much larger than the sensor node, it has a much less constrained power budget. In some cases, the base station can even be powered directly from the electrical grid. At the cost of power consumption and system volume, the base station has excellent receiver sensitivity and digital processing ability. Therefore, in the idle state, the sensor node is sleeping in order to save energy, while the base station receiver is always listening because of its relaxed power budget. Periodically, the sensor node initiates communication by transmitting a packet starting with multiple pulses at a predefined pseudo-random interval (i.e., a header). Once the base station detects the packet, it accurately estimates the baseband timing offset of the sensor node, adjusts its local timer frequency accordingly and then sends a response packet after a precise (using the timing offset correction), pre-defined guard time delay set by the sensor node timer. Since the packet (and data-symbol) arrival time is now synchronized to the sensor node baseband timer, the sensor node receiver no longer requires power-demanding timing offset estimation and symbol boundary synchronization. The sensor receiver can simply sample and compare to demodulate the OOK-modulated signal. Note that in this scheme, it is the sensor node that periodically initiates communication with the base station, while the base station performs energy- / power-demanding synchronization. The time interval between communication initiations is set using a sleep timer [42] on the sensor node and does not need to be very accurate since the receiver is always listening. In this design, the sleep timer frequency is typically 3.5Hz but is tunable. For the sensor node, the digital baseband controller is integrated with an on-chip 200 kHz timer, which employs a resistive frequency locking technique [18]. Thanks to the sensor-initiated synchronization scheme, the baseband controller and timer consume only 4.8 μW active power in total.

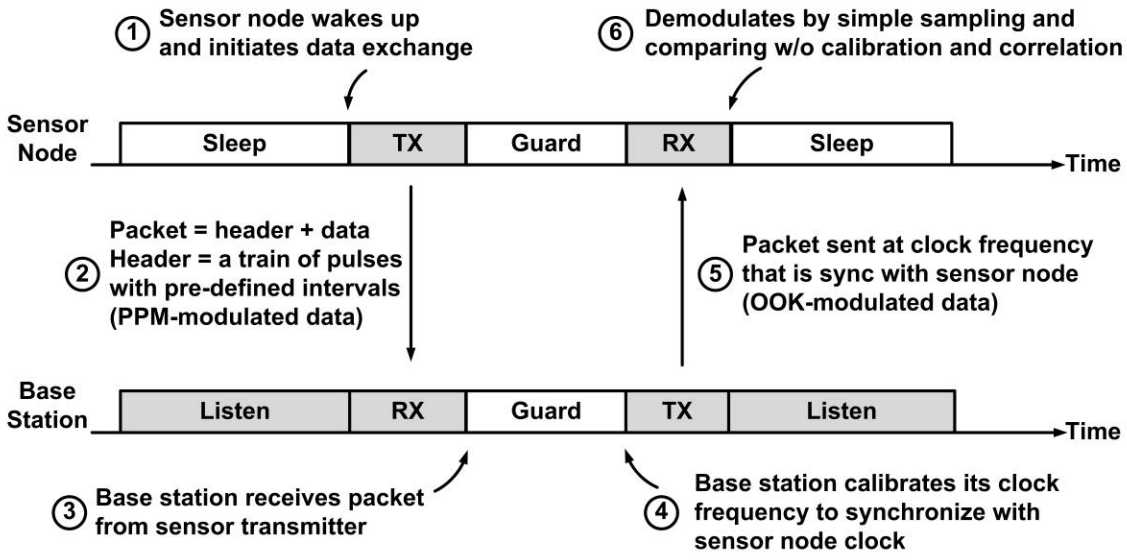

Figure 2.5: Conceptual explanation of proposed sensor-initiated synchronization.

2.2.3 Wakeup Scheme

Since many medical implants required long-term monitoring, battery life is critical for these applications. Figure 2.6 shows the architecture and timing diagram of the wakeup system. Periodically, or as instigated by the processor, the wake-up controller powers on the 200-kHz baseband timer in two phases. First, the linear regulator inside the timer is stabilized for 300 ms while the VCO is clock-gated. Then, the VCO clock gate is released, and after 7.5k cycles for frequency stabilization, the FastFSM, finite state machine logic, clocked with the 200 kHz baseband timer, wakes up the baseband controller. This multi-stage wakeup is used to minimize the duration that power consuming blocks such as the baseband timer and the baseband controller are active, while giving lower power blocks such as the regulator enough time to stabilize. In simulation, the regulator consumes 50nW while the VCO consumes 250nW. However, the regulator requires a stabilization time of 300ms while the timer requires only 100ms stabilization time. Hence, the regulator is stabilized first using the sleep timer, after which the baseband timer is stabilized by counting its own clock cycles since the

sleep timer frequency is too slow to accurately set the stabilization time. After the baseband controller is clocked and enabled, it interacts with the processor via MBUS to retrieve the message data. The baseband controller then powers on the transceiver and performs time-multiplexed modulation (TX) and demodulation (RX) according to the sensor-initiated protocol. After completing a complete cycle of transmit and receive, the baseband controller raises the BB_DONE signal which switches the system back to sleep mode, with only the wake-up controller and sleep timer remaining active. The overall sleep power of SoC is measured to be 22 nW, which results from the power of wake-up controller and the sleep timer and leakage current of all other circuits and pads. The system is designed to operate on a 1x2.2 mm^2 thin-film battery (2 μAh, 4.1 V). Consider a periodic communication session where the sensor node wakes up and transmits and receives 16-bit data. Per session, the transmitter is active for 8ms at 43.5μ (2 kbps) and receiver operates for 160 μs at 36 μW (100kbps). If the guard (or turnaround) time is 100ms between transmit and receive phases, the baseband controller operates for 108.16ms at 4.5 μW. The baseband timer consumes 300nW for 508.16ms per session including the time for stabilization. Therefore, the total energy that the SoC consumes per session is 993nJ. The stabilization of baseband timer is necessary because stable clock is required for synchronous communication between sensor node and base station. But it adds energy overhead each time the system wakes up. Start-up of baseband timer consumes 300nW for 400ms, while system sleep power is 22nW. Thus, as long as sleep time is longer than 0.43s, duty-cycling of baseband timer is worthwhile to save energy. The system is highly duty-cycled to increase the battery life ($>>$ 0.43s). Assuming a periodic session with 10-minute interval, the average power of the whole system is 23.7nW (sleep power is 22nW). It corresponds to a 2-week expected lifetime without battery recharging. Although above calculation assumes no battery recharging, for final implants, wireless power transfer from an external energy source can be used to recharge the thin-film

battery, which can further improve device lifetime. Typically, power can be wirelessly transferred through inductive-coupling link [31]. Other wireless transfer methods have also been proposed, including near infrared light [1] [48] and current bursts through electrodes [33]. However, wireless power transfer using the proposed antenna is beyond the scope of this work and subject of future work.

2.3 Antenna Design

2.3.1 Asymmetric Inductive Link

The target link between the sensor node and the base station is asymmetric, which results from the fact that the antenna in the base station has a relaxed dimension constraint ($> \text{cm}^2$), whereas the sensor antenna has a strictly constrained dimension ($<$1x10 mm^2) due to the size of the syringe needle. Furthermore, in the proposed system, the millimeter-scale sensor antenna is printed on glass substrate for easy assembly, while the base station antenna is printed on a circuit board (FR4 material). The base station antenna has a relatively large quality factor (> 60) due to lower loss traces of FR4 printed board. Most biological tissues have magnetic permeability almost equal to that of a vacuum, which makes inductive link suitable for through-tissue communication [56]. First-order modeling of the inductive link is shown in Figure 2.7, where L1 and L2 are self-inductance, R1 and R2 are loss resistance, C1 and C2 are parallel capacitance and M is mutual inductance. The subscript 1 and 2 indicate the

transmitting side and the receiving side, respectively. A resonant inductive link is utilized because at resonant frequency, the coupling strength is maximized due to passive voltage boosting, which can enhance the communication range [29]. The coupling strength is quantified with transimpedance, whose magnitude at resonant

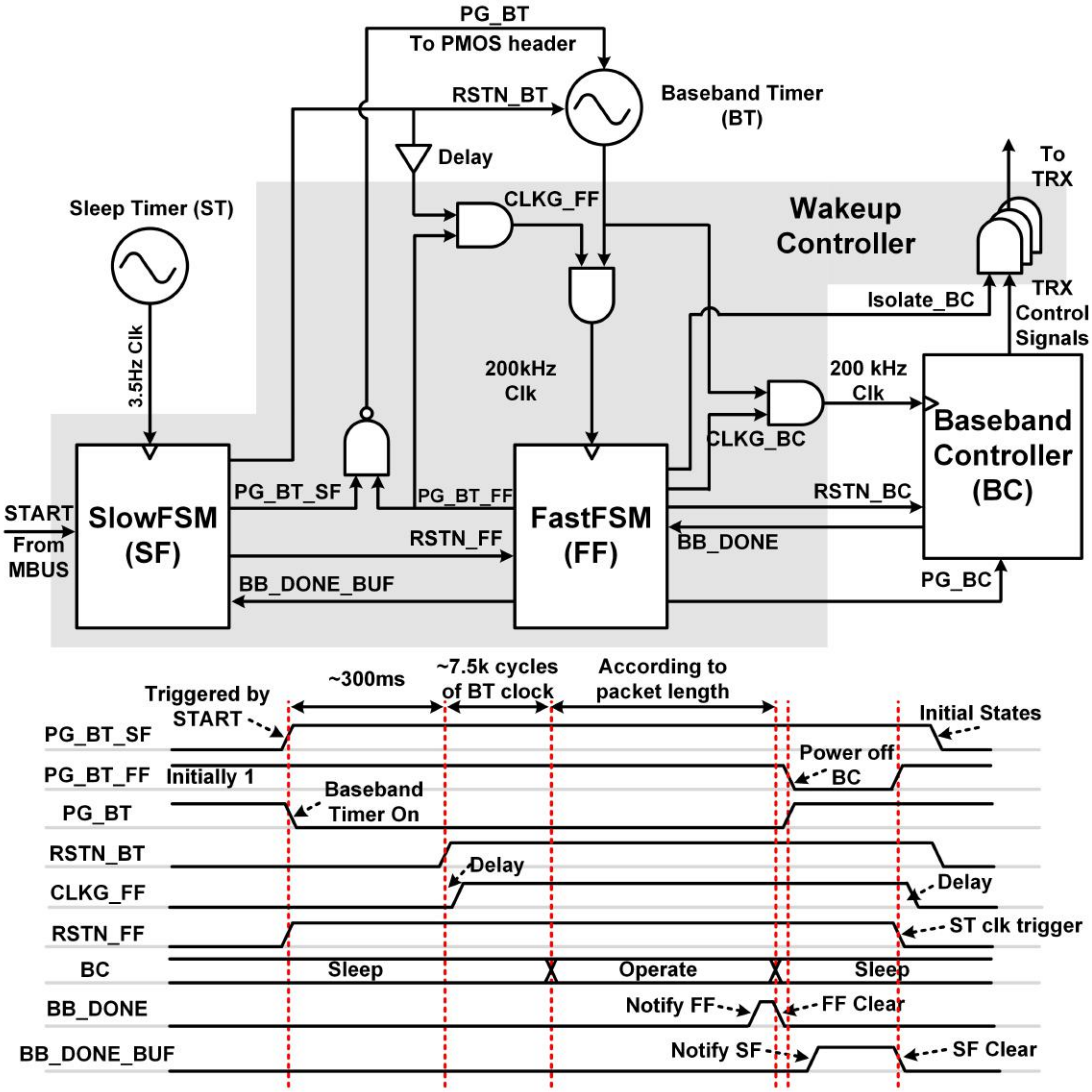

Figure 2.6: Architecture and timing diagram of wakeup system.

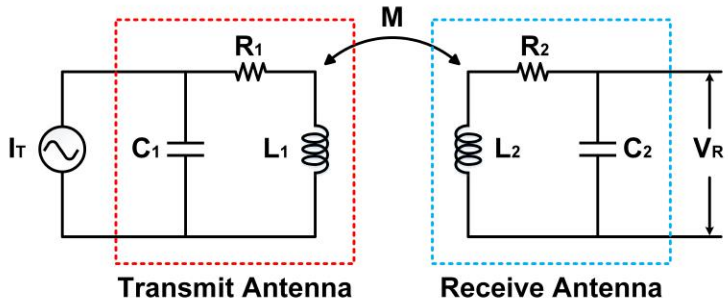

Figure 2.7: Modeling of asymmetric inductive link.

frequency is

$$|\frac{V_R}{I_t}(\omega_s)| = \omega_s M Q_1 Q_2 \tag{2.1}$$

where V_R is the received voltage, I_t is the transmitted current, M is the mutual inductance, Q_1 and Q_2 are the quality factor of the each antenna and ω_s is the self-resonant frequency (SRF). In this work, we design the two antennas to resonate at the same frequency, which is the theoretical optimum center frequency. Note that the coupling link in Figure 2.7 is a passive two-port network, which is reciprocal and thus transfer functions are same regardless of communication direction between implanted sensor node and base station.

2.3.2 Antenna Design Flow

To determine coupling strength, four variables (Q_1, Q_2, SRF and M in Eqa.2.1) must be co-optimized, and those variables are functions of the antenna dimension. In our design, High Frequency Structure Simulator (HFSS) is used to simulate an individual coil to acquire Q and SRF of each possible coil dimension. However, mutual inductance depends on the distance between the two antennas and simulating a complicated 3D scenario with two antennas in HFSS is extremely time consuming. Thus, the mutual inductance is calculated based on a model called Partial Element Equivalent Circuit (PEEC) [26][27]. For any two magnetic antennas, the total mutual inductance is the sum of all of the partial mutual inductances that exist between any pair of metal bars [32]. If the current distribution in each conductor is uniform (i.e, there is negligible skin effect), then the partial mutual inductance can be calculated using an equation that depends solely on the geometry and relative position of the two bars which allows for extremely fast mutual inductance calculation, which implemented in MATLAB. While PEEC does not model retardation, this is an acceptable approximation for near-field communication and the resulting accuracy is within 3% compared to 3D HFSS simulation. Using the PEEC and HSFF two analysis tools, the

overall antenna optimization is then performed as follows: A particular set of antenna dimensions is selected. The sensor and base-station antennas are each individually simulated using HFSS to obtain Q and SRF, and then the MATLAB PEEC model is used to obtain M. These model parameters are then inserted into the model equation to obtain the transimpedance or in the model itself to perform co-simulation with the transceiver circuits. Since each of the two antennas has three parameters (outer width W, outer length L and number of turns N), the number of possible antenna topologies is enormous. To make this multidimensional search tractable, we first constrain the total width of the sensor antenna to 1mm to fit in the syringe diameter, leaving two search parameters for the sensor antenna (Lsn and Nsn). Second, we assume that base station antenna is square shape (Wbs=Lbs), leaving two parameters for the base-station antenna (Wbs and Nbs). To further limit the search space, we make a useful observation that a single-turn base station antenna is optimal, as shown in Figure 2.8, because as the number of turns is reduced, SRF and Q of the base-station antenna increase while M decreases. At the same time, the corresponding optimal sensor antenna also has a higher Q due to the increased frequency. Since three factors (ω_s, Q_1 and Q_2), increase and one (M) decreases when the fill factor is reduced, a smaller turn number results in a larger transimpedance. Therefore, we arrived at the conclusion that a single-turn base station antenna is optimal (Nbs=1). This reduces the number of search parameters to only 3 (Wbs, Lsn and Nsn). In this derivation, metal width and spacing of PCB antenna are 600 μm and 250 μm, respectively, which are chosen to constrain the searching space. Fill factor in Figure 2.8 is calculated based on this width, spacing, the turn number and outer dimension. If further optimization is desired, metal width and spacing should also be taken into consideration in the design process.

The final antenna dimension search is then performed as follows. For each sensor antenna length and number of turns, the optimal corresponding base station an-

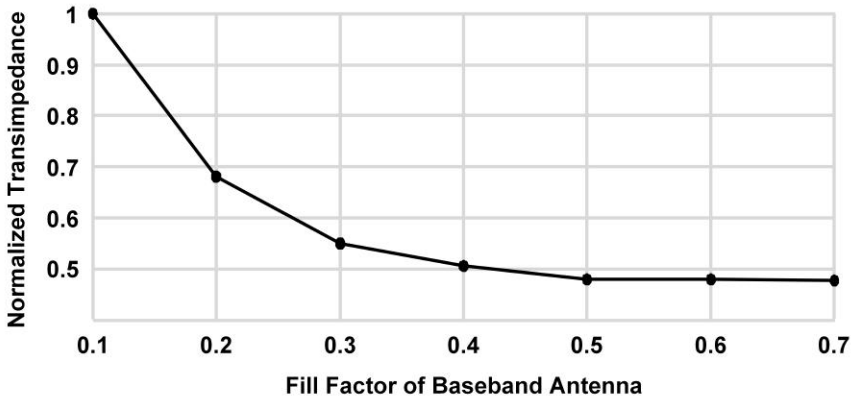

Figure 2.8: The relationship between coupling strength and fill factor of the base station antenna.

tenna (with a certain outer dimension) is found by matching its SRF with that of the sensor antenna SRF. The resulting antenna configuration is then analyzed, the transimpedance is obtained and the optimal configuration is selected. Figure 2.9 (a) shows the model parameters versus sensor antenna length and the resulting transimpedance. Increasing the sensor antenna length results in monotone increasing transimpedance due to increasing mutual inductance. However, beyond 8mm length, transimpedance saturates due to decreasing Q and SRF, thus there is a diminishing return for increased size.. We also found a similar trade-off for the fill factor , which is shown in Figure 2.9 (b). The transimpedance saturates when the fill factor is larger than 0.6, which corresponds to 15 turns. Thus, the sensor antenna is designed to be 11x8 mm^2 in total size with with 15 turns of 15 μm turn width and 5 μm spacing,, while the corresponding optimal single-turn PCB antenna is 11x11 cm^2 with 600 μm metal width. The layout of sensor antenna and the photo of base station antenna are shown in Figure 2.10 (a) and (b) respectively. The sensor antenna was simulated in HFSS and measured with probe testing, as shown in Figure 2.10 (c) and (d). We used Impedance Standard Substrates to calibrate the network analyzer and probe setup, which decouples the effect of probe in testing and ensures accuracy. At the chosen frequency, skin depth within gold metal is 7.2 μm, which is comparable to half

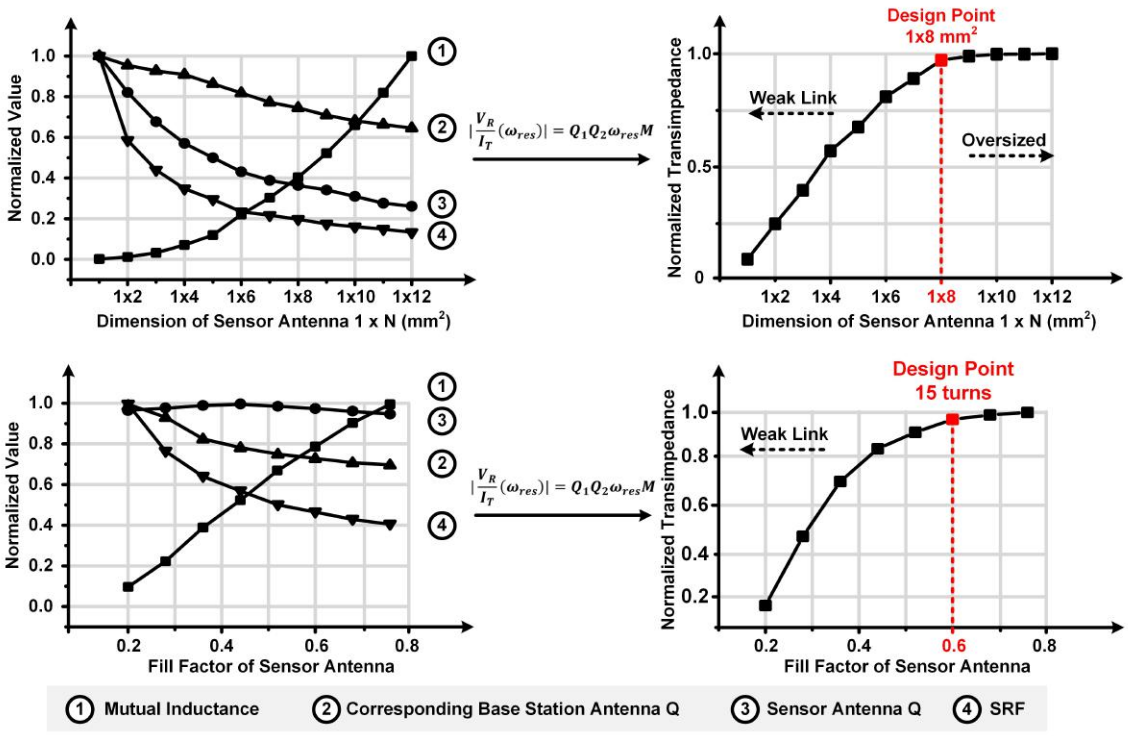

Figure 2.9: Co-design of the sensor antenna with base station antenna (a) dimension (b) fill factor.

metal width (15 μm) and larger than metal thickness (1.5 μm) of sensor antenna. Therefore, skin effect expected to be small in the proposed antenna structure.

2.3.3 Frequency Selection

In this work, the 114.7 MHz center frequency for uplink from the sensor node to the base station is determined based on the above analysis to maximize the link strength. At this particular center frequency, the field strength due to the signal transmitted from the sensor node remains well below the FCC limit of 150 μV/m at a distance of 3 m [20] since the sensor antenna has very limited gain. However, this FCC spectral mask significantly constrains the maximum power from the base station while a large base station transmit power is desired to relax the sensitivity requirement of the sensor receiver. As a solution, we propose a system with asymmetric center

(a)

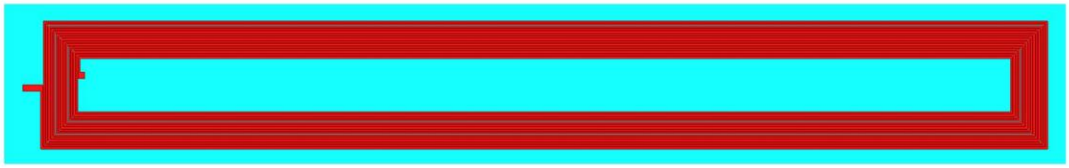

(b)

(c)

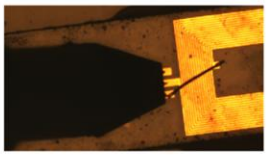

(d)

	HFSS Simulate	Measure
L (nH)	1670	1660
R (ohm)	290	258
SRF (MHz)	118	114.7

Figure 2.10: (a) Layout of sensor antenna on glass substrate. (b) 11x11 cm2 base station antenna printed on FR4 board. (c) Probe testing of sensor antenna. (d) comparison of HFSS simulation and measurement results for sensor antenna.

frequency allocation. We observe that the FCC limit at 49.82-49.9 MHz is 36.5dB larger than 150 μV/m, allowing base station to transmit 36.5dB larger power in this band. However, resulting transimpedance is 21.5dB weaker due to lower frequency and lower resonant Q for the designed antenna pair. Overall, the requirement for sensor node sensitivity is reduced by 15 dB. Therefore, we selected 49.86 MHz as the center frequency for the base station to sensor, even if it is sub-optimal in terms of link strength. We implement a digitally tunable on-chip capacitor array to change the sensor node antenna resonant frequency according to the transmit and receive mode.

2.3.4 Effect of Biological Tissue

Until now, proposed design flow has not considered the effect from biological tissue after implantation. However, it can be expected that resonant frequency of antenna may change due to the tissue around it. HFSS simulation shows that the resonant frequency of sensor antenna will shift down by 12MHz when the antenna is packaged by a 1x1x10mm^{3}glass capsule and fully covered by muscle tissue. The frequency-dependent dielectric properties of muscle are based on previous study [25].

The frequency shift can be tolerable in this work, since base station transceiver has ability to tune carrier frequency.

2.4 Circuits Design

2.4.1 Pulsed Transmitter

Figure 2.11 shows the architecture of the transmitter and the associated conceptual waveforms. The transmitter consists of a power oscillator, pulse generator, current limiter and decoupling capacitor (decap). The power oscillator, combining the functions of frequency generation and power delivery, is implemented to replace the power-hungry frequency synthesizer and power amplifier. The sensor transmitter circuit operates at 13.6 mW for the maximum output power. However, the maximum peak power of the intended thin-film battery ($< 50\mu$W) is insufficient to provide such a large current to power the oscillator. Thus we employ an integrated decap (1.3nF) made of a metal-insulator-metal (MIM) capacitor as an energy-buffer. The decap is formed by top two metal layers, which are placed over digital circuits (wakeup controller, baseband controller and MBUS controller) to save chip area. As shown in Figure 2.11, during a pulse, the power oscillator draws high current from the decap (decap voltage drops), delivering strong output power to the antenna. After a pulse is transmitted, the power oscillator is shut down and the decap needs to be recharged before the next pulse is transmitted. However, the peak current that can be drawn from the battery is limited by its large intrinsic resistance. In this work, the current limiter is implemented as a series resistor (100kohm) between battery and decap, limiting the recharging current to be less than 15 μA, which protects the battery from being overdrawn. Therefore, recharging time is long compared to pulse width and the resulting transmitted signal is a series of sparse pulses. To exploit this unique feature, the transmitter employs pulse position modulation (PPM). The baseband controller

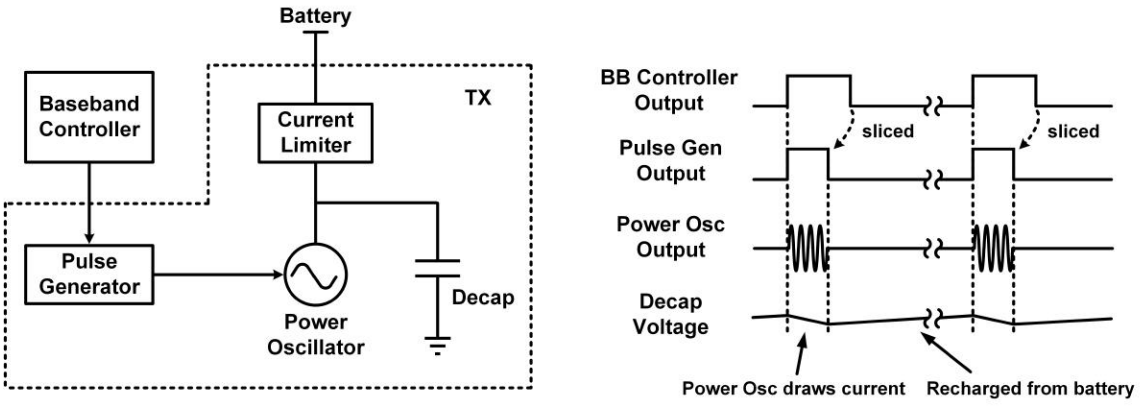

Figure 2.11: Architecture of pulsed transmitter and conceptual waveforms.

generates the control signals to enable the pulse transmission. The enable signal is sliced by the pulse generator to produce a tunable-width pulse, which can be shorter than a baseband clock period.

A conventional power oscillator is based on a cross-couple pair of oscillators that provide negative resistance. To start up and sustain the oscillation, the negative resistance, which depends on the bias current, must to be large enough to overcome the loss in the tank [14][49]. However, since the oscillator draws constant bias current, it has a low transmit efficiency (simulated as 40%). In this work, we propose a new pulse inject oscillator (PIO). Figure 2.12 shows its schematic, which consists of a switched-capacitor start-up circuit and pulse inject loop. To increase efficiency, the proposed oscillator injects pulsed-current through an H-bridge only when oscillation is near the peak. The startup time, a critical factor for an efficient pulsed-radio, is less than 2 cycles.

Figure 2.13 shows the simulated waveforms in SPICE, showing the operation of the PIO. Before a pulse is generated, it takes 20 μs to pre-charge (Charge=1, TX_EN=0), with C1 discharged to ground and C2 charged to VBAT. At the same time, the two nodes of the antenna (VA and VB) are charged to VBAT/2, which is the desired common mode voltage. C3 is also charged to VBAT/2, which will be used as the

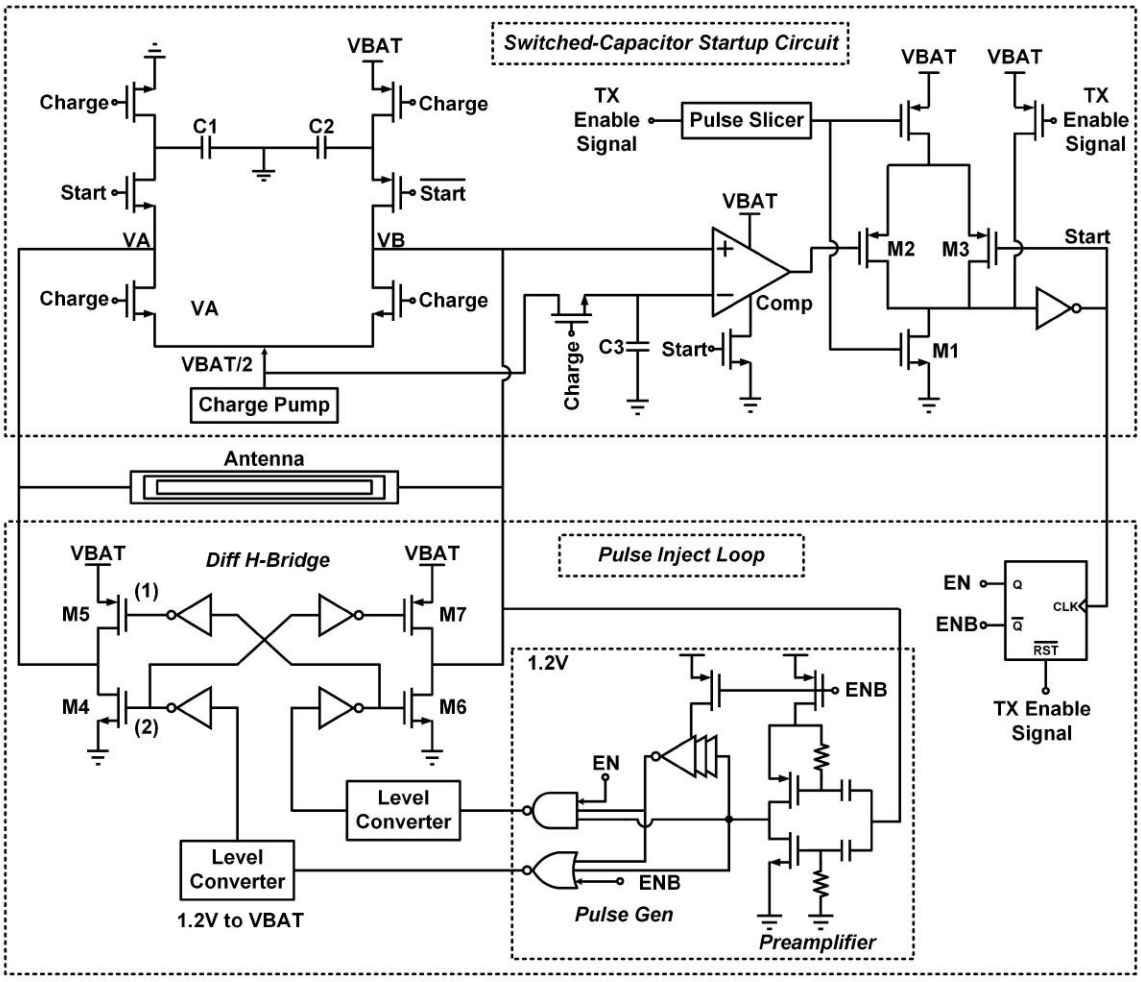

Figure 2.12: Schematic of proposed pulse inject oscillator.

reference voltage in the next phase. Note that Start is 0, so the open-loop comparator is off. VBAT/2 is generated using a serial-parallel charge pump, clocked by the baseband timer. After pre-charging is finished, TX_EN toggles to 1, and the pulse slicer generates a pulse of 1.2 ns, which turns on NMOS footer M1 and switches Start to 1. When Start becomes 1, C1 and C2 share charge with the antenna and inject an initial charge to VA and VB, initiating oscillation. Since Start is 1, the comparator is powered on, and its output is 1. When the pulse slicer output returns to 0, M1 is turned off, but Start remains 1 because the PMOS switches M2 and M3 are off. VA and VB continue to change until half of an oscillation cycle is completed. Since VB crosses VBAT/2, the output of the comparator toggles from 1 to 0, switching Start to 0 and causing three things to happen. First, C1 and C2 are disconnected from the antenna since enough energy is now transferred into the antenna. Second, the comparator is powered off. Third, the pulse inject loop is enabled by a negative-edge triggered flip-flop. At this point, the pulse inject loop sustains the oscillation. A preamplifier combined with a pulse generator extracts and generates digital pulses from the oscillation signal. The preamplifier uses resistor bias at its gates to reduce short-circuit current. The pulses at the transistor gates of the differential H-Bridge, which are tuned to overlap with the peak of the oscillation points, control the H-Bridge to inject current into the antenna differentially, which sustains the oscillation. The four transistors (M4-M7) have low power loss because during current injection, VDS is low, and during off-state, the current is 0, which enhances efficiency. The proposed design utilizes two voltage domains (1.2 V and 4.1 V VBAT) to reduce the overall power consumption. During a pulse, VA and VB oscillate at full swing between 0 and the battery voltage (4.1 V), which provides the largest possible transmit power. The simulated power efficiency of the proposed pulse-inject oscillator is 68%, which is 1.65x higher than that of a constant-bias cross-couple oscillator. Since battery voltage (VBAT) is 4.1V, HVT transistors with thick gate oxide are utilized for the circuits

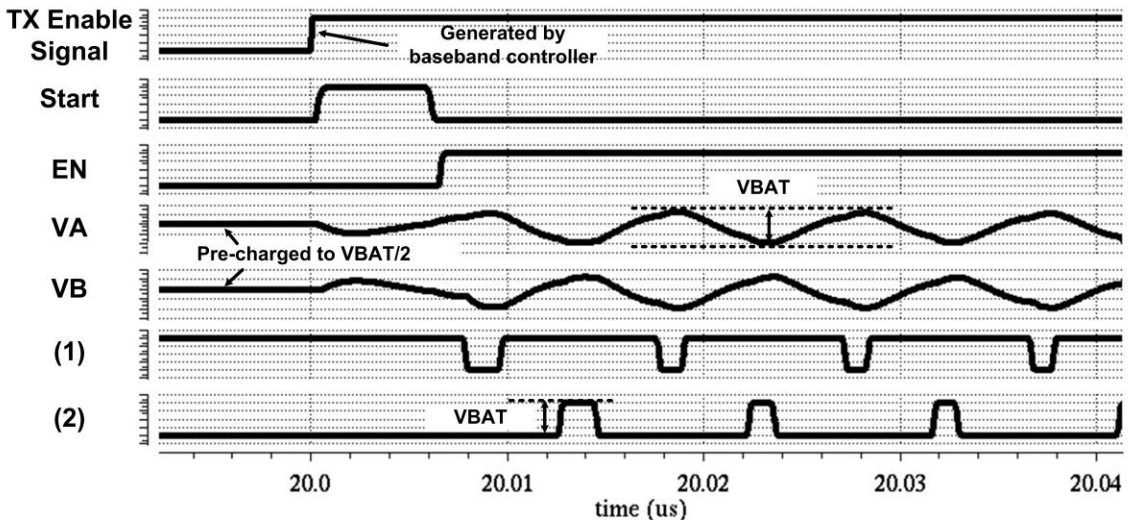

Figure 2.13: Simulated waveforms of pulse inject oscillator using SPICE.

that operate on battery voltage and SVT transistors are used for 1.2V domain.

2.4.2 OOK Receiver

Unlike the sensor node where pulsed transmission is employed because of the power constraint, the base station transmits with a continuous OOK scheme. The sensor receiver demodulates the OOK signal from the base station continuously drawing current from the 1.2 V supply. It is feasible because its power consumption is less than the maximum peak power of the millimeter-scale battery ($< 50\ \mu$W). Figure 2.14 shows the schematic of the receiver, which consists of a 3-stage amplifier, envelope detector (ED) and clocked comparator. The received signal is amplified and demodulated by the ED. A clocked comparator samples and digitizes the output of the ED. The first-stage amplifier is a current-reuse inverter amplifier for high current efficiency. The transistors in the amplifier are biased at the sub-threshold region for higher gmI efficiency. The gain of the three-stage amplifier is simulated as 37 dB at 49.86 MHz. The ED comprises a source-follower topology, and the transistor is biased at the non-linear region, consuming 200 nA. The load capacitor can be tunable up to

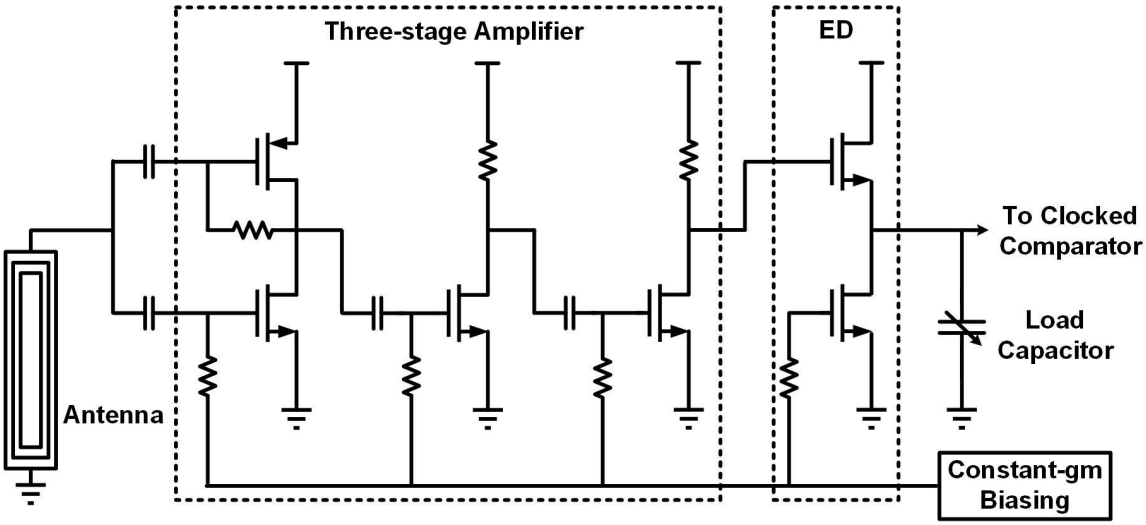

Figure 2.14: Schematic of OOK receiver.

31 pF, filtering out any high frequency components. A constant-gm biasing circuit is designed for the amplifier and envelope detector. The total receiver consumes 36 μW while demodulating 100 kb/s OOK signal.

2.5 Measurement Results

Figure 2.15 shows the chip microphotograph of the proposed near-field radio fabricated in 180 nm CMOS technology. The chip has a total area of 1050 μm x 2120 μm including the pads. Proposed radio is designed for wireless through-tissue communication. To demonstrate this feasibility, a medium of 3 cm-thick bovine tissue (typical beef steak) is utilized in following wireless testing of the transceiver.

The transmitter was measured when driving the antenna on glass substrate (sensor antenna). Figure 2.16 shows the measured time-domain waveforms of the transmitter in pulsed mode. Once the pulse is enabled by the baseband controller, the oscillation can start up quickly. With the pulse generator, the pulse width can be digitally tunable from 150 ns to 1320 ns. When the pulse width is 920 ns, the transmitter supply voltage on the decap drops by 1.5 V during every pulse as shown in the

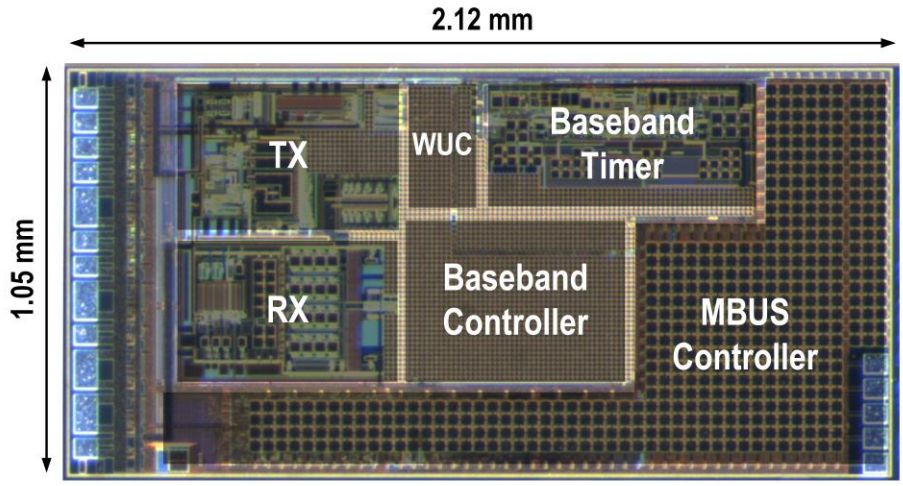

Figure 2.15: Die photograph of the proposed radio, where MIM decoupling capacitor is placed over WUC, Baseband Controller and MBUS Controller

measurement but is recharged to its full level after around 500 μs, where the current limiter sets the recharging current to be less than 15 μA. For the communication range and power spectrum measurement setup, we used an external 4.1-V supply to allow the sensor node power oscillator to continuously draw current. The sensor transmitted signal was wirelessly received by the 11x11 cm^2 base station loop antenna printed on an FR4 board through 3cm-thick bovine tissue. Figure 2.17 shows the power spectrum measured with a Spectrum Analyzer, and Figure 2.18 shows the measured power across a range of distances and relative angles between two antennas.

The receiver sensitivity was measured using a wired setup where an RF signal generator was connected to the sensor node receiver via a cable or through the antenna pair. Wired setup is used to measure receiver sensitivity quantitatively, where the input of receiver was connected to the signal generator (source 50Ω) through SMA cable. Figure 2.19 shows the measured sensitivity across input power, which is the value directly read from signal generator. Note that due to impedance mismatch (receiver input non-50Ω), actual receiver input power is less than the value read from signal generator. At a BER of 10^{-3} and a data rate of 100 kb/s, the receiver has a sensitivity at -54 dBm and consumes 36 μW at a supply voltage of 1.2 V. This same

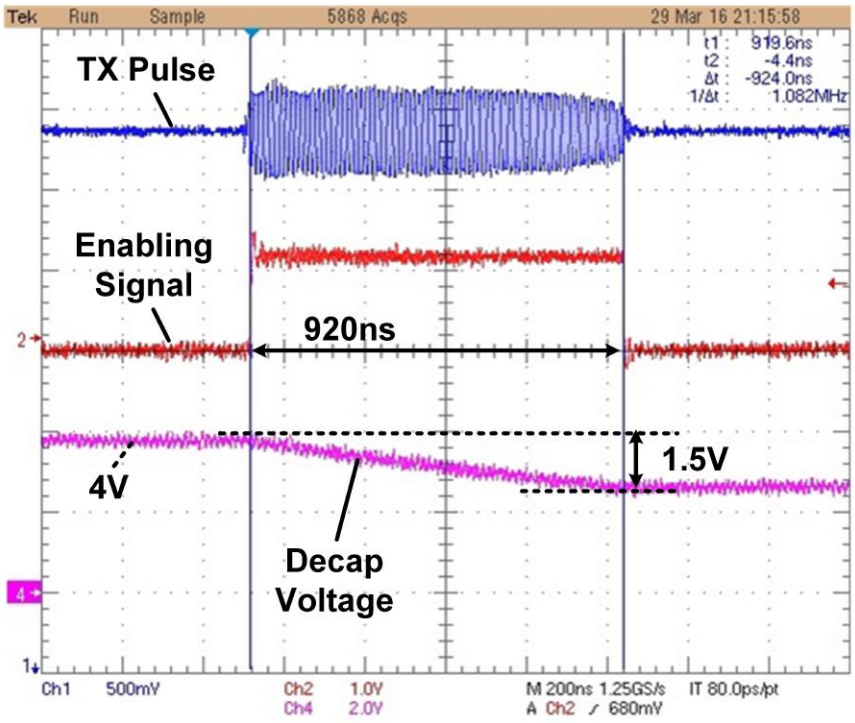

Figure 2.16: Measured waveforms of transmitter.

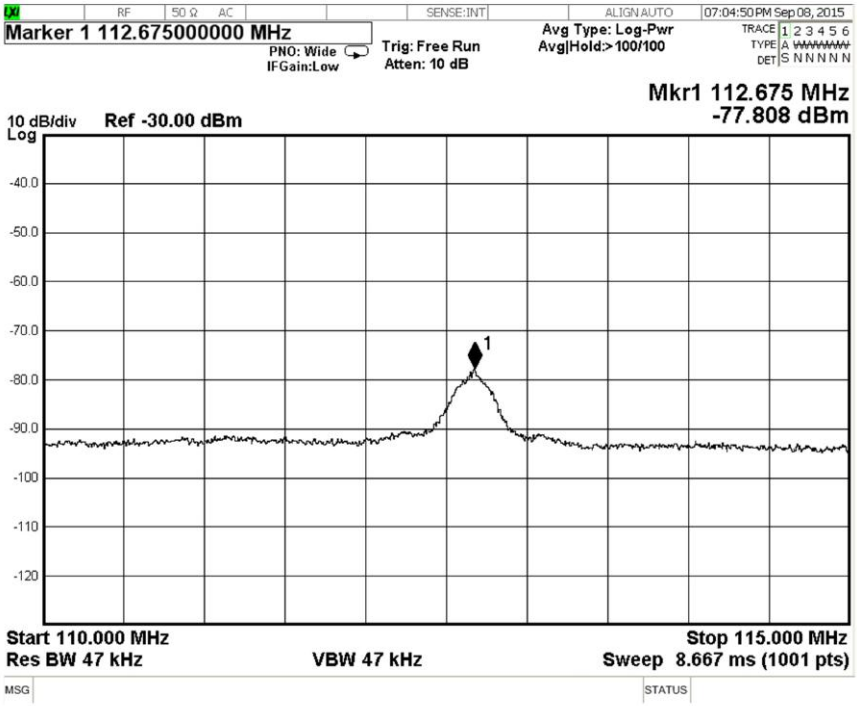

Figure 2.17: Measured power spectrum of transmitted signal received by base station antenna.

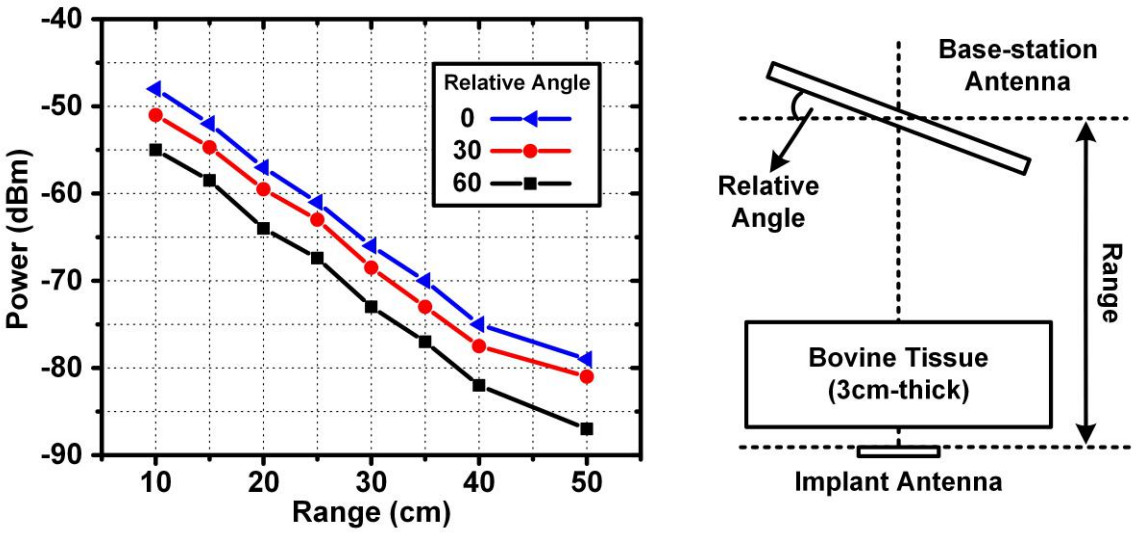

Figure 2.18: Measured transmitter output power vs. range and relative angle between two antennas.

BER was also measured wirelessly at approximately 20 cm through 3cm-thick bovine tissue, where the RF signal generator feeds the OOK-modulated signal into the base station antenna with 1-Watt power, and the chip detects it using the sensor antenna. While demodulating 100 kb/s OOK signal, the measured waveform of the envelope detector output when two antennas are separated by 3cm and 20cm are shown in Figure 2.20 and 2.21 respectively.

The timer has a nominal frequency of approximately 200 kHz. Since the temperature is typically stable in implanted applications, the frequency variance of the timer is dominated by the supply variation. Figure 2.22 shows the measured frequency variance with the supply voltage ranging from 1.1 V to 1.3 V, corresponding to a supply variation of 0.28%/V. Figure 2.23 shows the transient response of the timer frequency after powering on the timer, demonstrating that the frequency is stabilized after 7.5 k clock cycles, which is approximately 100 ms.

To demonstrate the proposed radio system, we implemented a prototype base station that can detect the transmitted pulses from the proposed radio by down-mixing,

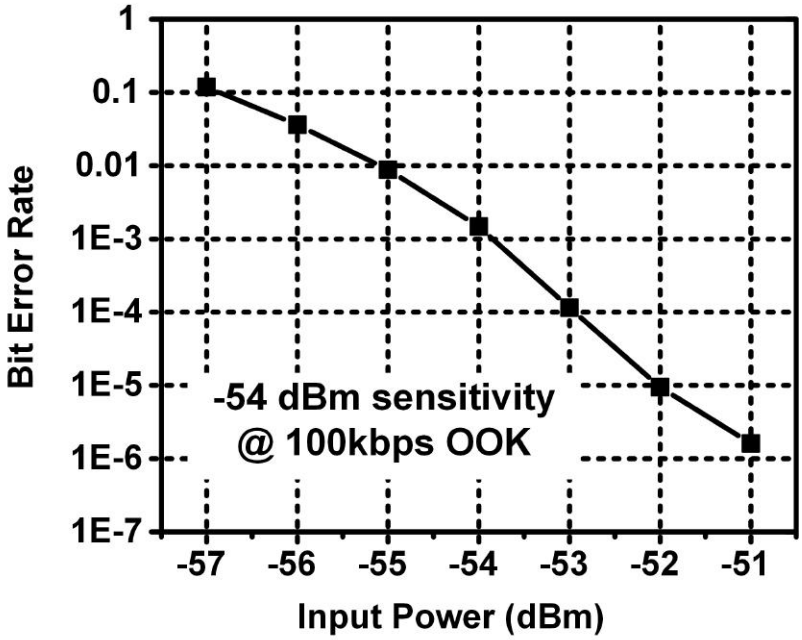

Figure 2.19: Measured sensitivity of receiver.

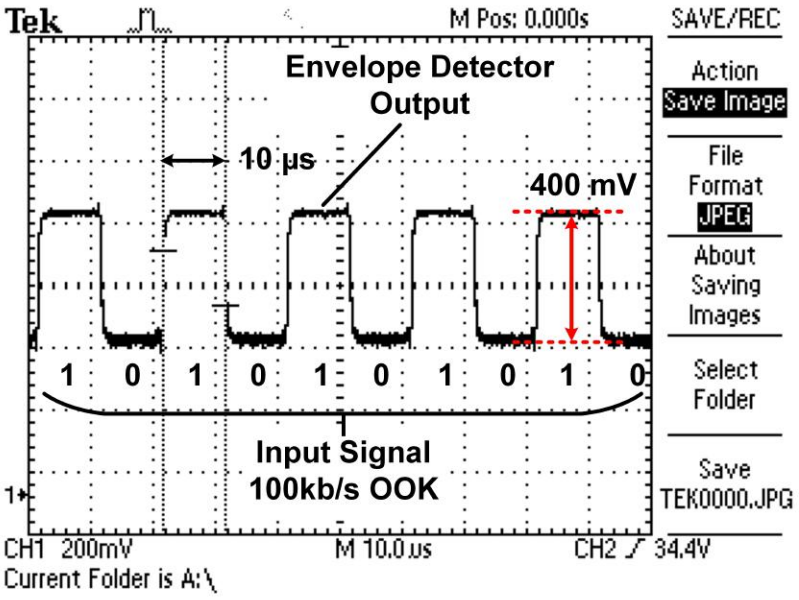

Figure 2.20: Measured waveform at the output of receiver envelope detector wirelessly at different distance at 3cm.

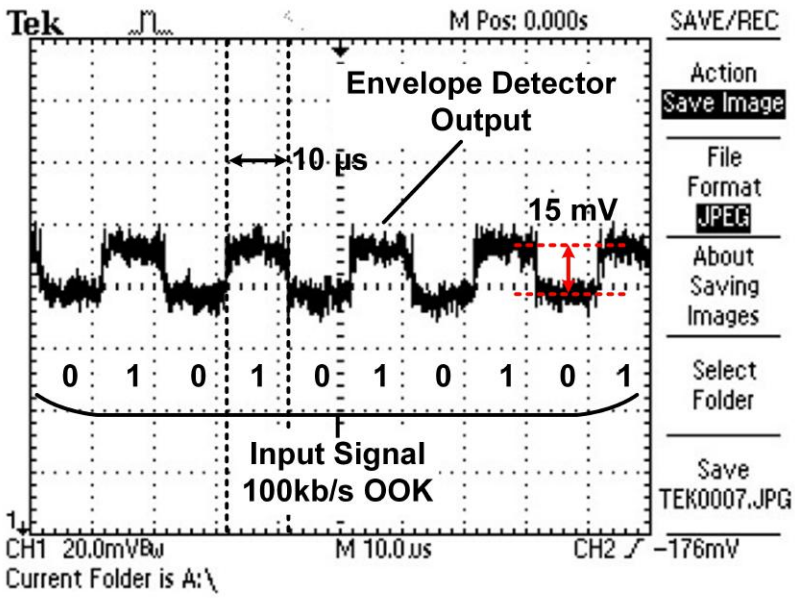

Figure 2.21: Measured waveform at the output of receiver envelope detector wirelessly at different distance at 20cm.

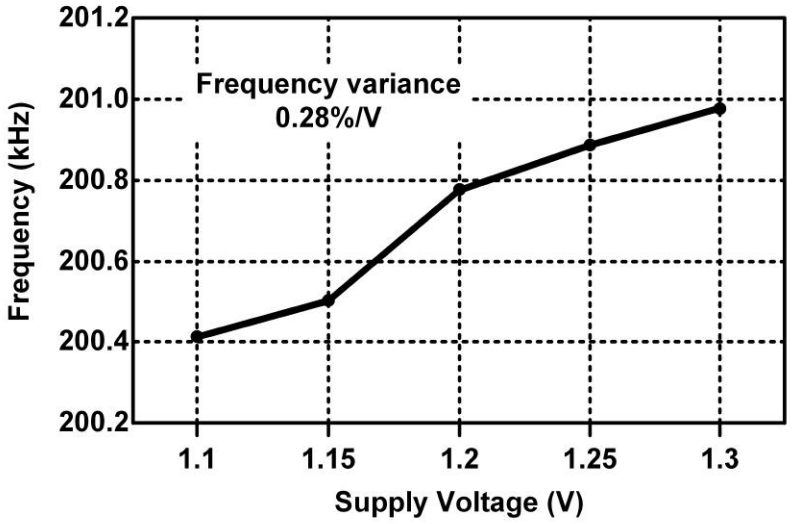

Figure 2.22: Measured supply variance of baseband timer frequency.

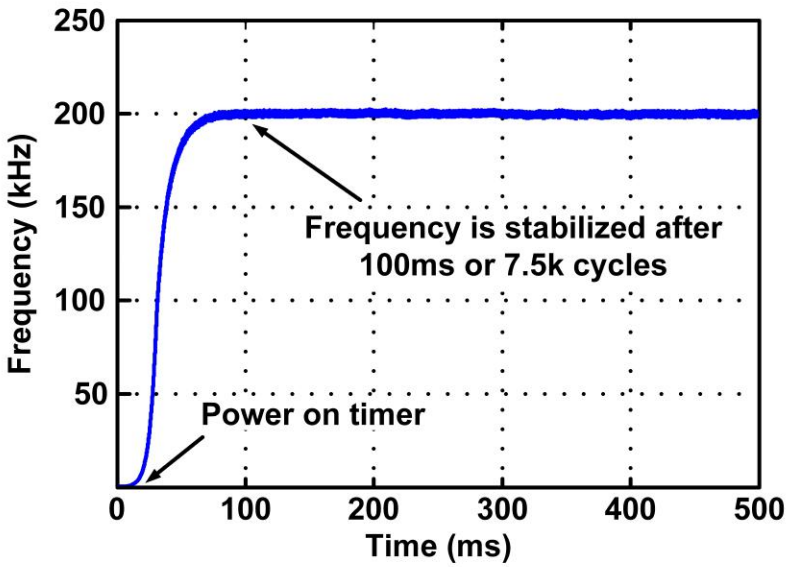

Figure 2.23: Measured transient settling of baseband timer frequency.

converting to digital format and oversampling at 10 MHz. Figure 2.24 shows the captured pulses using the prototype base station. It shows that the proposed radio is woken up every 320 ms (programmable) by the wakeup controller. Every time the radio wakes up, it transmits a packet consisting of 8 pulses. Figure 2.25 shows the measured waveforms of the transmitted pulses and the decap voltage. After the radio wakes up, the decap is charged to 4 V, and the transmitter generates pulses, which are controlled by the baseband controller. After transmission finishes, transmitter circuits are power gated, and the decap is disconnected from battery and thus decap voltage gradually drops due to leakage current, as expected. The generated pulse pattern corresponds with the captured results at the base station. When 32 pulses are used for the packet header, the software-based algorithm on the base station can successfully track and correct the baseband frequency offset within 2000ppm (0.2%) between the sensor node and the base station. To demonstrate a complete self-contained system, this radio chip is measured with other system peripherals including a processor layer, decap layer and the power management unit. During the testing, the battery voltage (4V) is provided from a supply generator, while 1.2V volt-

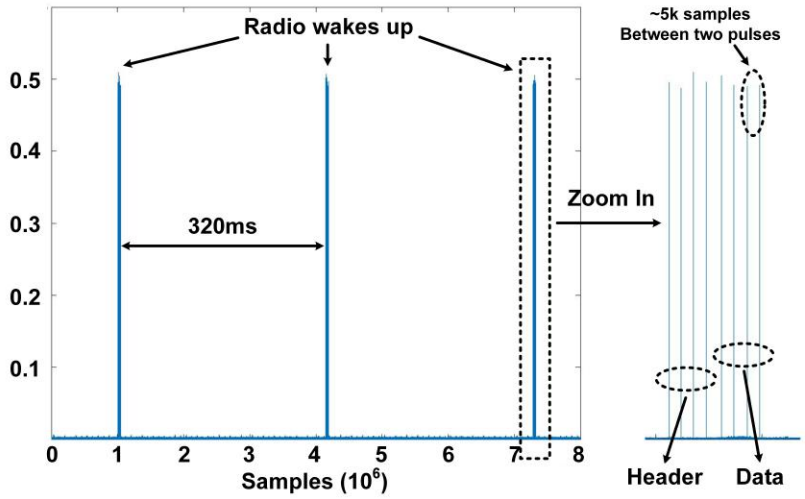

Figure 2.24: Captured transmitted pulses using prototype base station receiver.

age is generated by the power management unit by down-converting from the same 4V terminal. Configured by the processor on the processor layer using the MBUS interlayer communication [37], the chip periodically wakes up, transmits and receives data as expected, verifying the functionality of power management scheme and chip-to-chip interface. Figure 2.26 summarizes the performance of each block in the radio. Figure 2.27 provides a comparison to related prior work.

2.6 Summary

A fully integrated near-field radio chip fabricated in 180 nm CMOS technology is demonstrated for syringe-implantable smart sensor nodes. A 1x8 mm^2 antenna printed on glass substrate and an 11x11 cm^2 base station antenna printed on FR4 circuit board are co-designed to form an asymmetric inductive link between the sensor node and base station. The transceiver, co-designed with the 1x8 mm^2 sensor antenna, consumes 43.5 μW average power at 2 kbps, while the receiver power consumption is 36 μW with -54dbm sensitivity at 100 kbps. The radio can operate on a millimeter-scale battery that has a stringent 50 μW peak power constraint. The system was

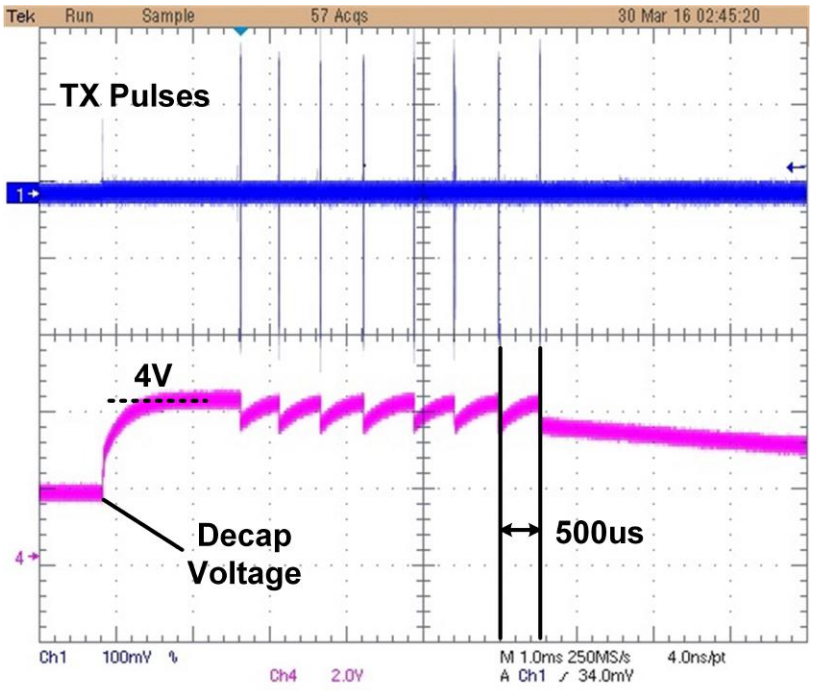

Figure 2.25: Measured waveforms of transmitter showing correspondence.

Technology		180nm CMOS
Die Area		2.12 x 1.05 mm^2
Transmitter	Average Power	43.5 µW @ 4.1V
	Peak Power	13.6 mW @ 4.1V
	Center Frequency	112 MHz
	Modulation	PPM
	Pulse Width	150-1320 ns
	Data Rate	2 kbps
	Output Power	-78 dBm @ 50cm
Receiver	Active Power	36 µW @ 1.2V
	Center Frequency	49.86 MHz
	Modulation	OOK
	Data Rate	100 kbps
	Sensitivity	-54 dBm
	BER	10^{-3}
Baseband	Active Power	4.8 µW @ 1.2V
	Clock Frequency	200 kHz
System Sleep Power (Including Wake-up Controller)		22 nW

Figure 2.26: Summary of the system performance.

		This Work	CICC 2013 Yakovlev et al.	ISSCC 2011 Chen et al.	VLSI 2011 Mark et al.
Technology		180 nm	65 nm	180 nm	65 nm
Application		Syringe-implanted Sensors	Implanted Sensors	Intraocular Pressure Monitor	Implanted Neural Sensor
Antenna		1 x 8 mm^2 15-turn	2 x 2 mm^2 1-turn	0.4 x 0.4 mm^2 6-turn	1.1 x 1.1 mm^2 1-turn
Communicate Distance	Transmit	50 cm	3.5 cm	10 cm	1.3 cm
	Receive	20 cm	3.5 cm	N/A	N/A
Transmitter	Architecture	Pulse Injection LC Oscillator	Passive	Constant Bias LC Oscillator	Passive
	Center Freq	112 MHz	1.32–2.14 GHz	570/690 MHz	535 MHz
	Modulation	PPM	LSK	FSK	LSK + PPM
	Peak Power	13.6 mW	1.4 µW	45.7 mW	660 nW
	Data Rate	2 kbps	2 Mbps	7.5 kbps	2 Mbps
Receiver	Sensitivity	-54 dBm @ 100kbps	Unknown	N/A	N/A
	BER	$1x10^{-3}$	Unknown		
	Center Freq	49.86 MHz	1.32–2.14 GHz		
	Modulation	OOK	ASK		
	Power	36 µW	1.2 µW		
Baseband Controller and Clock		Integrated	N/A	N/A	N/A

Figure 2.27: Comparison table with recent prior work.

measured to achieve a range of 50 cm for the sensor TX and 20 cm for RX. This work enables wireless communication for the implanted smart devices, increasing their potential use cases in healthcare applications.

CHAPTER III

A 915MHz Asymmetric Radio for 3x3x3 mm^3 Sensor Node with 20m Non-Line-of-Sight Communication

3.1 Introduction

The number of connected devices is fast growing towards the highly anticipated vision of the ubiquitous Internet-of-Things (IoT). Along this trend, millimeter-scale computers have a potential to play important roles in many applications. Making the computing device or wireless sensor node smaller, lower power, and more affordable has become an important problem for both industry and academic research, especially in indoor environment that is difficult for RF communication. Enabling long range (>10m) wireless communication in non-line-of-sight (NLOS) scenarios can dramatically expand the application space and usability of millimeter-scale computers.

However, there are numerous challenges for the radio system fully integrated within a millimeter-scale form factor, as explained in Section 1.1. Among them, the major technical challenges are poor antenna efficiency and the small instantaneous current limit ($\sim$ 10s of μA) of thin-film batteries. We address these challenges in several ways:

1) We found that a magnetic dipole antenna achieves better efficiency at an

electrically-small size than an electric dipole, when the antennas are resonated with finite-Q lumped components. In addition, the high imaginary impedance of electrically-small electric dipoles ($\sim$ 4 kΩ compared to 10 Ω for the magnetic antenna) requires an impractically large off-chip inductor to resonate.

2) By simultaneously considering the magnetic dipole efficiency, frequency-dependent path-loss, and wall penetration loss, we found that a 915MHz carrier frequency is optimal for a 3x3x3mm sensor node in NLOS asymmetric communication with a gateway [15]. This is despite the resulting low antenna efficiency (0.21%) which typically drives mm-scale radios to operate at >> 1GHz frequency [63].

3) Proposed transceiver is co-designed with proposed magnetic antenna [19]. In transmit (TX) mode, instead of using a PA and PLL, we utilize a cross-couple driver to resonate the magnetic antenna at 915MHz with a quality factor (Q) of 110 in order to reduce overall power consumption. In receive (RX) mode, we propose a novel approach of reusing the cross-couple driver in a non-oscillating mode to raise the Q of the resonant tank to 300, resulting in 49 dB voltage gain at 43 W, thereby replacing a power-hungry LNA and bulky off-chip filter.

4) A sparse pulse position modulation (PPM) combined with an asymmetrical sensor-initiation communication protocol [59] shifts the power-hungry calibration of frequency offset to the gateway, enabling crystal-free radio design.

In this work, an energy-autonomous radio system, including the transceiver IC, a 3D antenna, off-chip capacitors, a processor, a power management unit (PMU) and memory, is integrated within a 3x3x3mm sensor node, and was demonstrated in stand-alone bi-directional 20m NLOS wireless communication. Data rates is variable from 30bps to 30.3kbps for TX and 7.8kbps to 62.5kbps for RX. The transmitter TX generates -26.9 dBm equivalent isotropically radiated power (EIRP) consuming 2mW power and the receiver RX has a sensitivity of -93dBm consuming 1.85mW power.

The content of this work in Chapter III was published previously in collaboration

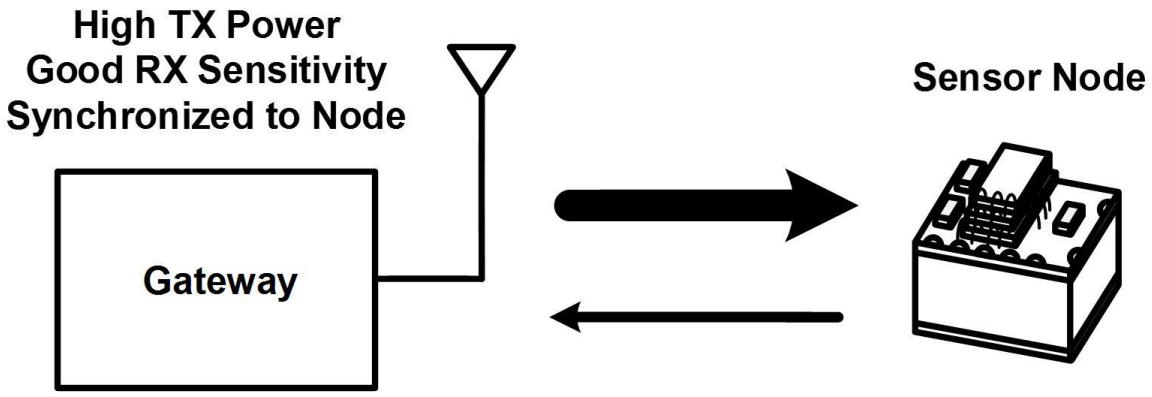

Figure 3.1: Asymmetrical link between 3x3x3 mm sensor node and gateway

with my fellow group member Li-Xuan Chuo [19].

3.2 Overview of System

Similar to the near-field radio described in Section II, proposed far-field radio system communicates with gateway through asymmetric inductive link as shown in Figure 3.1. The gateway transmits high output power and has good RX sensitivity at cost of higher power and system volume than sensor node. Proposed radio within the millimeter-scale sensor node is crystal-free and PLL-less and thus the frequency stability is sacrificed. To address this, the system employs a gateway assisted synchronization protocol that is initiated by sensor node transmission, which will be described in Section 3.4.

3.2.1 System Architecture and Construction

The overall architecture of the proposed radio system is shown in Figure 3.2.The 3D magnetic dipole antenna is manufactured using a 3x3x2 mm circuit board printed on a low loss Rogers RT/duroid 5880 substrate. Its 4-loop configuration, constructed from two copper layers and 2mm-height vias, achieves a 0.21% efficiency at 915MHz. The off-chip SMD capacitor C1 (0.5pF) and the integrated digitally-switched capac-

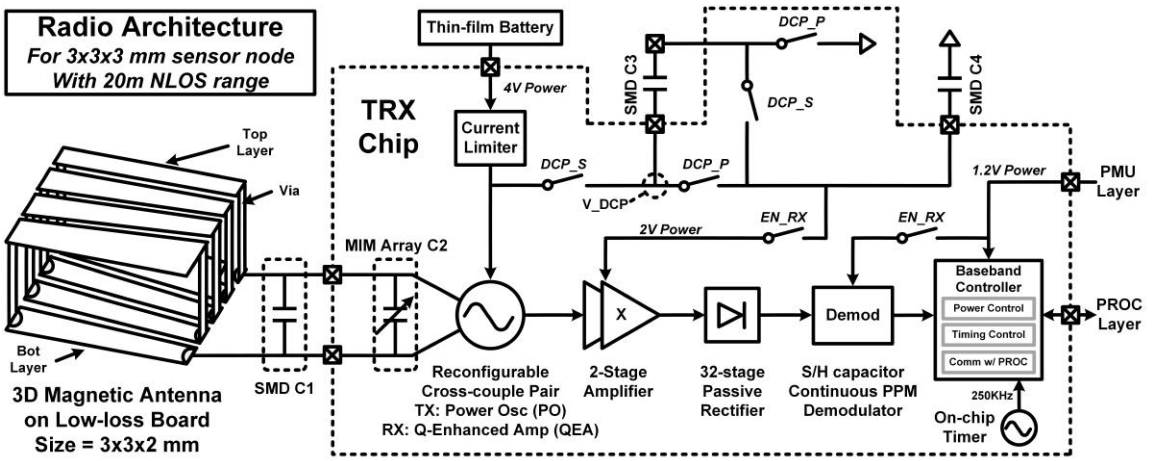

Figure 3.2: Architecture of proposed 915MHz radio for 3x3x3 mm sensor node

itor array C2 complete a resonant tank with a Q of 110 at 915MHz. The resonant frequency is tuned using C2 within the 891.4-932 MHz range. It is shown later in Section 3.3 that the efficiency of a magnetic antenna exceeds that of a more traditional electric dipole antenna for extremely small electrical sizes ($< 0.015\lambda$) when resonated with lump components. Furthermore, an electric dipole typically requires physical separation from the electronics, while the proposed magnetic dipole allows electronics to be stacked on top and bottom, enabling compact integration. As shown in Figure 3.3, the electronics stack, along with three off-chip capacitors, are placed on one side of the antenna while a photo-voltaic (PV) cell and batteries are on the other. This makes it possible to expose the PV while protecting sensitive electronics from light when coated in black epoxy. The transceiver chip consists of RF front end, power management, baseband controller circuitry and a ultra-low-power on-chip timer [18]. The baseband controller directly modulates the transmitter bias current to generate RF modulated pulses. The receiver performs energy detection with a Q-enhanced amplifier followed by additional amplifiers and a 32-stage passive rectifier.

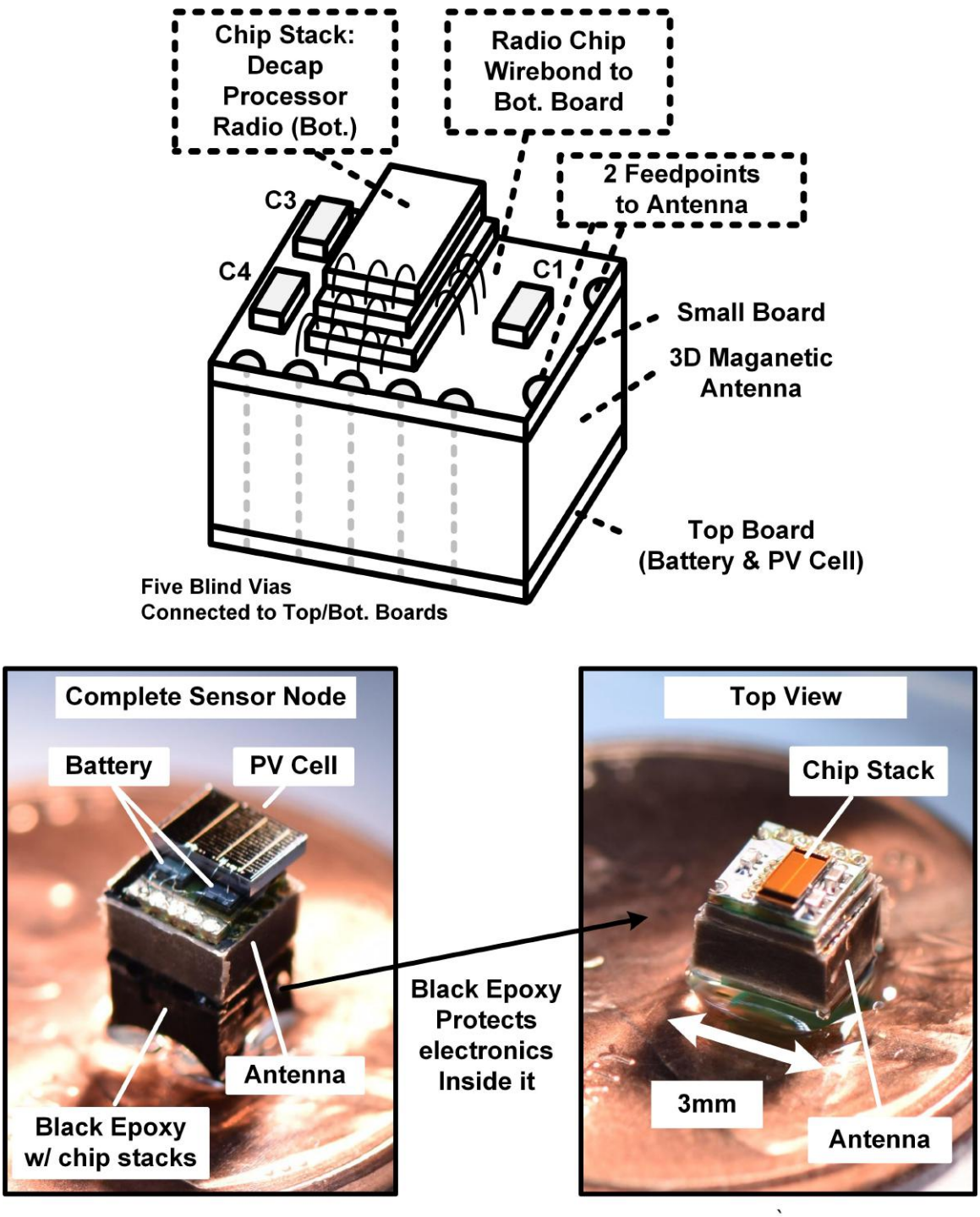

Figure 3.3: Physical construction of sensor node including proposed radio

3.2.2 Transceiver Schematic and Operation

Figure 3.5 shows schematic of transceiver circuits and Figure 3.4 shows the timing and operation of proposed radio. In transmit mode, a cross-coupled driver resonates the magnetic antenna at 915MHz with a bias current >100 μA. This architecture delivers power to the antenna with an efficiency of 32.4% (calculated based on measurements results) and replaces the power hungry PA and PLL. However, open-loop operation results in carrier frequency drift, which we address with a wider frequency search at the gateway at the cost of increased gateway complexity. Because the peak TX current exceeds the thin-film battery current limit, the TX circuits operate from a 0.5μF storage cap (when C3 and C4 are series-connected) while the thin-film battery ($\sim$4V), under the protection of a current limiter ($\sim$10μA), continually charges the storage cap. The relatively long storage cap recharge time between transmit pulses results in inherent sparsity. We exploit this sparsity to realize a new energy-efficient modulation scheme that conveys multi-rate trellis-coded bits in the form of sparse M-ary PPM. The TX baseband controller supports dynamically adjustable modulation parameters such as the pulse width, number of pulse repetition, trellis-code rate (1/4, 1/3, 1/2, 1, 2, 3, 4) for error correction, and PPM modulation size M. In receive mode, we propose a new Q-enhancement amplifier (QEA) technique, where the cross-coupled pair is biased in a non-oscillating region (<20μA) as opposed to the oscillation region (>100μA), This raises the Q of the resonant tank to 300 (from 110 when QEA is disabled), resulting in 49dB voltage gain at 43W (simulated). The QEA replaces the high power and bulky off-chip components of a conventional LNA and channel selection filter. It also avoids the high power consumption and reradiation of a super-regenerative receiver [11]. The bias current of the cross-couple pair is digitally tuned with a tail transistor. Its output signal is further amplified by 17dB using a 2-stage amplifier consuming 870A from the parallel-connected C3 and C4 with a 2V supply. The RX demodulator consists of a 32-stage passive rectifier, 4 S/H capacitors

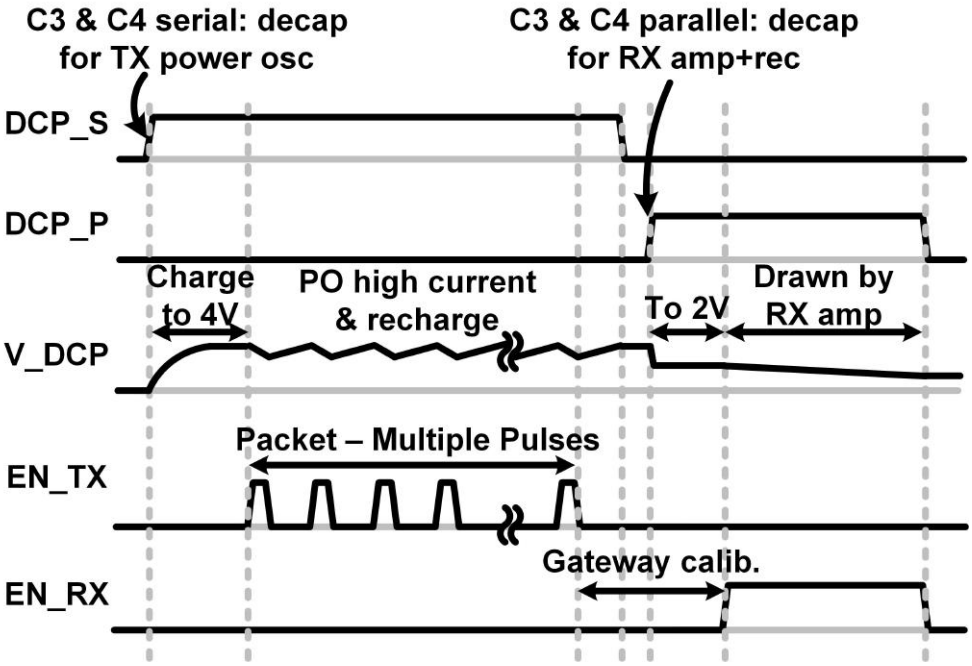

Figure 3.4: Timing showing operation of proposed system

and 2 clocked comparators that collectively consume 250nA from a 1.2V supply. The RX uses binary PPM. The rectifier output is sequentially sampled on S/H capacitors. Once two capacitors (Cs1 + Cs2 or Cs3 + Cs4) store the voltage for the 1st- and 2nd-half period of an incoming binary PPM symbol, an associated comparator (Comp1 or Comp2) generates a demodulated bit. This approach eliminates the need for an accurate reference voltage for the comparator.

3.3 Antenna and Carrier Frequency

3.3.1 Magnetic vs Electrical Antenna

At millimeter-scale dimension, the antenna is electrically small compared to the wavelength at 915MHz carrier frequency [9]. The antenna radiation efficiency is the major specification for communication range. We investigate two categories of the electrically small antenna: electric dipole with capacitive impedance and magnetic dipole with inductive impedance. Figure 3.6 shows the radiation efficiency at

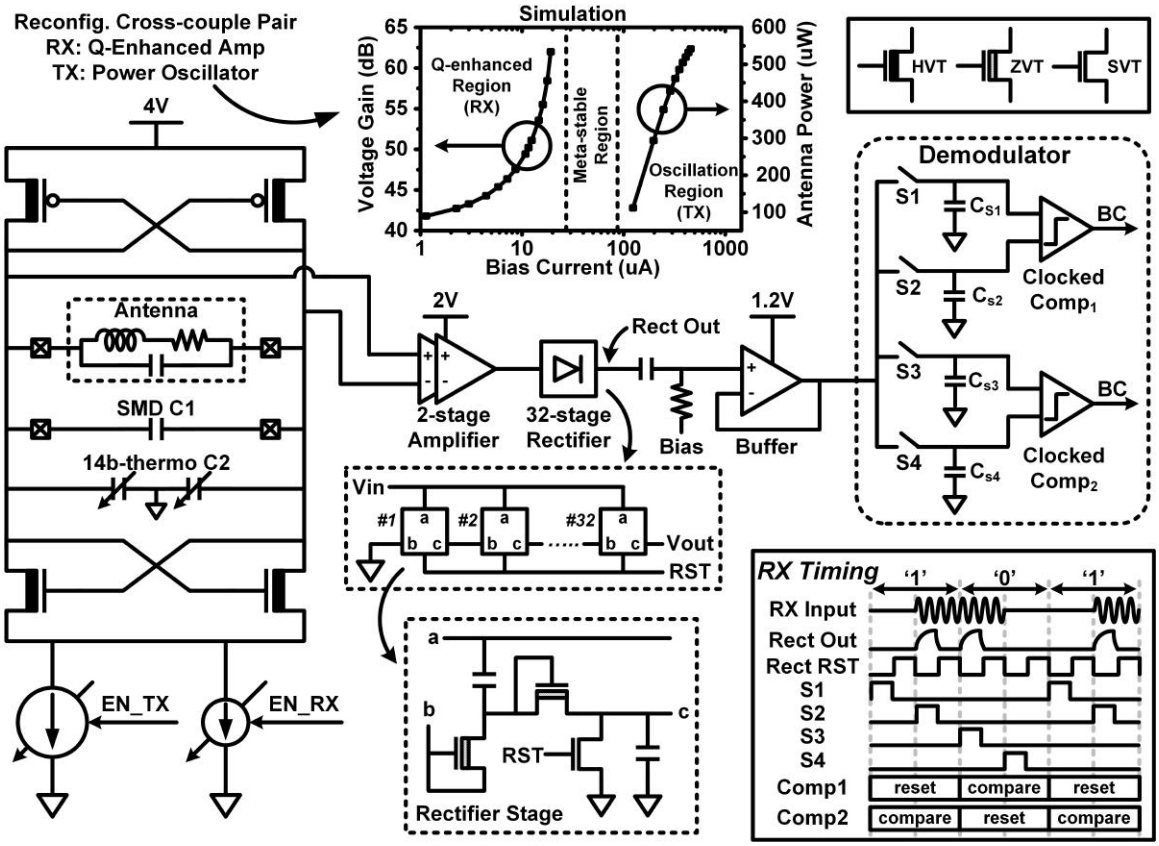

Figure 3.5: Schematic of transceiver circuits

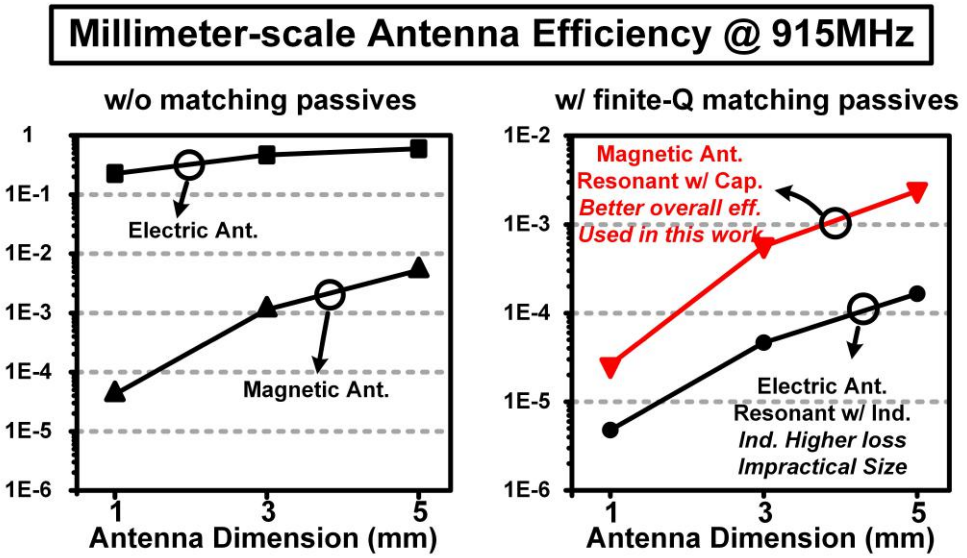

Figure 3.6: Millimeter-scale antenna efficiency at 915MHz

millimeter-scale dimension (1 to 5 mm) of both types of electrically small antennas. On the left, the standalone electric dipole has better efficiency than the magnetic dipole. However, in a practical system, we need to resonate out the imaginary impedance of the antenna. At 915 MHz, the electric dipole needs hundreds of nH inductance for matching, which will be lossy and bulky. In contrast, the magnetic dipole requires a capacitance of only a few pF available in semiconductor technology with pretty high Q (larger than 60). Therefore, a fair comparison is necessary. On the right of Figure 3.6, when quality of resonant passives is considered, the magnetic dipole has much higher efficiency at target dimension (3 mm). Utilized magnetic antenna is printed on a low-loss Rogers 5880 material as shown in Figure 3.7. The antenna exhibits 0.21% efficiency (-25 dBi gain) at 915 MHz from HFSS simulation.

3.3.2 Path Loss Analysis

To maximize the communication range, path loss including proposed magnetic antenna has to be minimized for longest range. As mentioned in Section 1.3.3, Friis transmission model is widely used when RF designers make link budget. The antenna

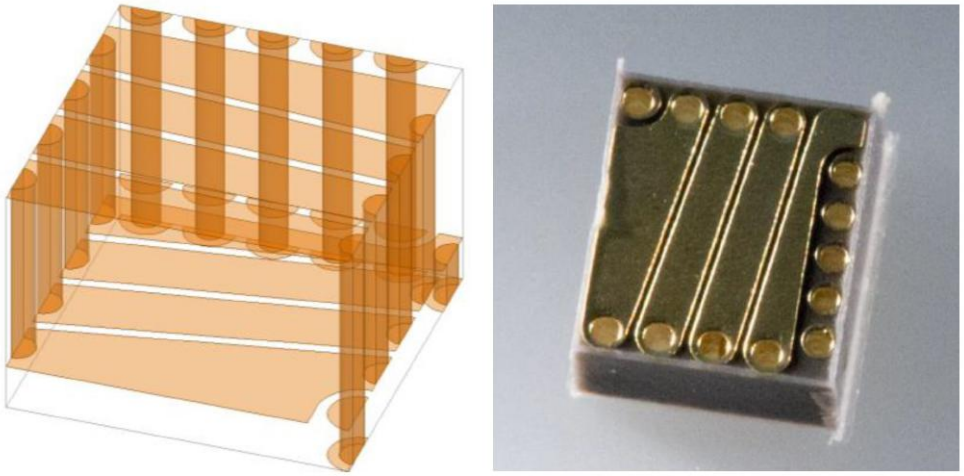

Figure 3.7: Printed 3D loop antenna

efficiency of proposed antenna is also included in analysis of path loss. As shown in Figure 3.8 (left), with Friis free-space model, higher carrier frequency reduces LOS path loss, because free-space transmission loss increase with quadratic of carrier frequency but electrically-small loop antenna increases with fourth power of carrier frequency [62]. This is the reason that millimeter wave (mmW) has been a typical choice for prior millimeter-scale radio systems [12] [63].

However, in this work, proposed sensor node is targeted for an indoor environment that includes one layer of wall/floor which blocks the LOS between the gateway and the sensor node. Therefore, ITU attenuation model given by Equation (3.1) is included to analyze path loss [58].

$$L(F_c, d) = 20 \log_{10} \frac{4\pi F_c}{c} + N \log_{10} d + FL(F_c) \tag{3.1}$$

In Equation (3.1), $L(F_c, d)$ is the path loss in dB, F_c is carrier frequency in Hz, d is communication distance in meter, c is light speed, N is the distance power loss coefficient (for indoor environment, empirically $N = 3$) and $FL(F_c)$ is floor loss depending on carrier frequency. The resulted NLOS path loss is shown in Figure 3.8 (right), showing that minimum path loss is achieved at around 1 GHz [15]. Therefore,

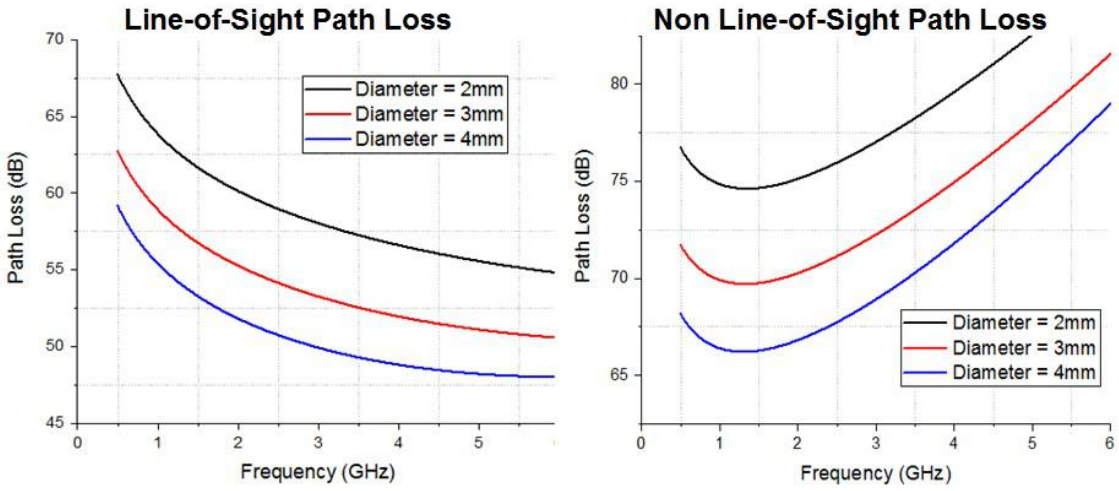

Figure 3.8: Path loss considering magnetic antenna gain for LOS and NLOS scenarios

ISM band frequency 915 MHz is selected for proposed radio system.

3.4 Sensor Initiate Protocol

Based on the 'sensor initiate protocol' that is described in Section 2.2.2, the sensor node starts communication by sending a header that consists of multiple pulses with predefined pseudo-random intervals. The gateway tracks and compensates the baseband timing and carrier frequency offset by analyzing the sensor TX header and sends a return packet back to the sensor node that is precisely synchronized to the sensor nodes ultra-low power timer and its carrier frequency. This frees the sensor node from the power-demanding timing and frequency synchronization, greatly lowering its complexity and power consumption. Using this synchronized return packet, the gateway further notifies the sensor node of the optimal modulation parameters (e.g., coding rate, pulse width, etc.), enabling a graceful tradeoff in link distance vs. data rate. We realized a real-time, fully functional communication protocol using a gateway prototype implemented on an USRP FPGA.

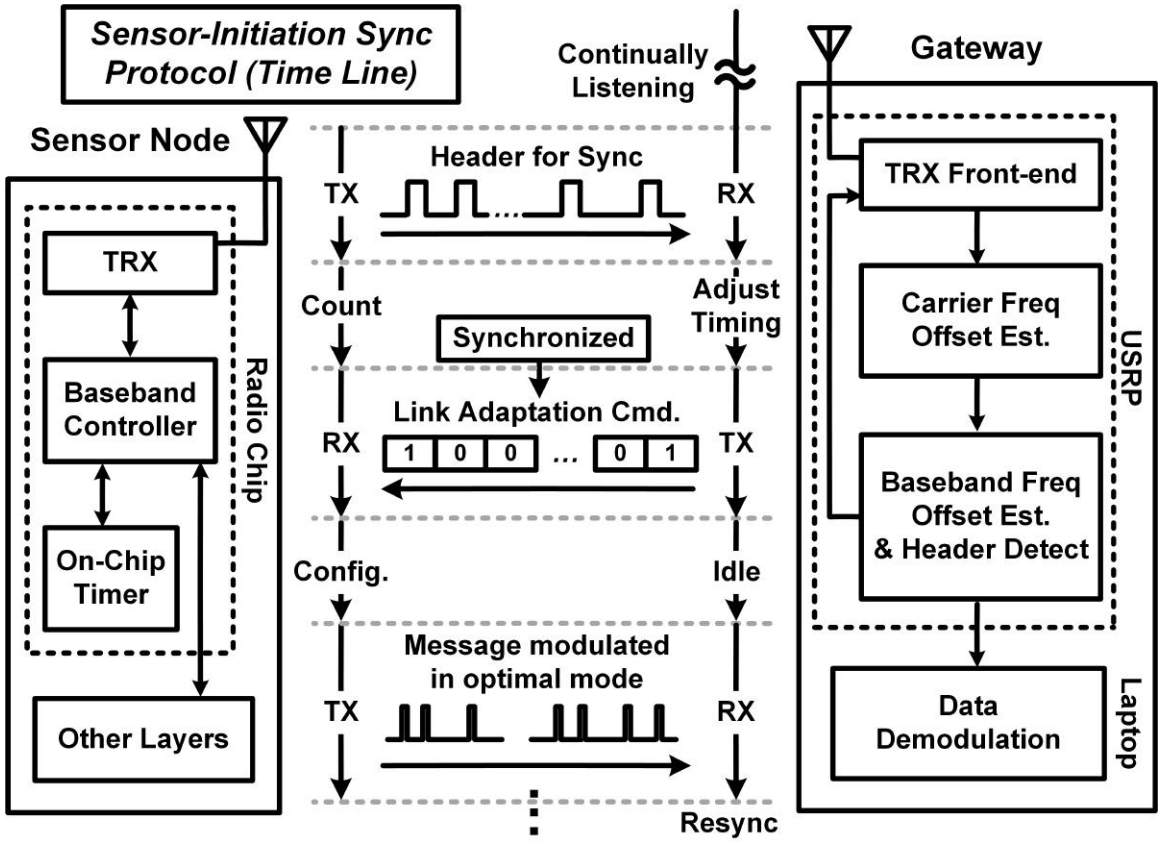

Figure 3.9: Adaptive sensor-initiation synchronization communication protocol.

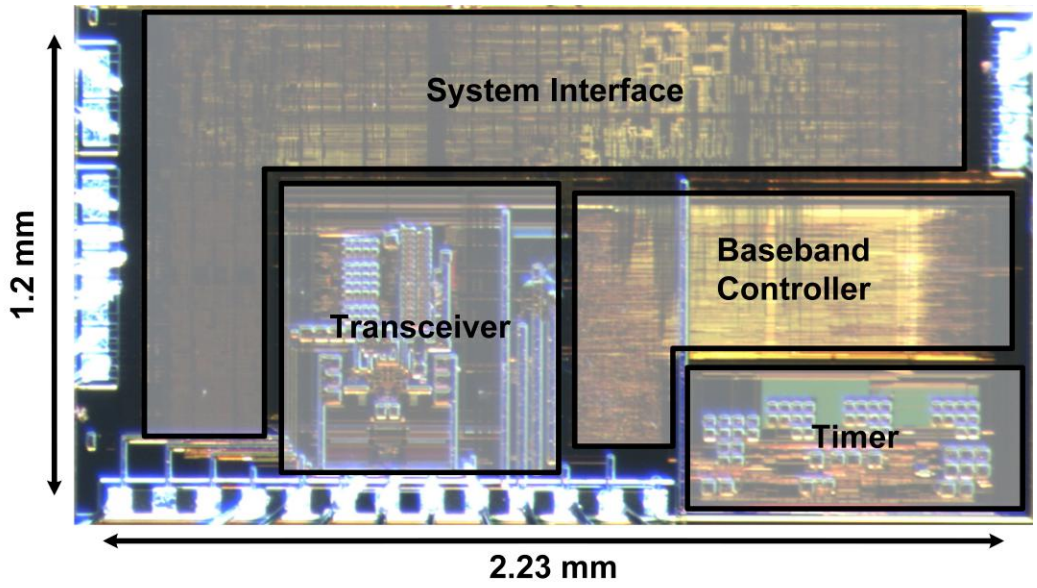

Figure 3.10: Die photo of transceiver

3.5 Measurement Results

As shown in Figure 3.10, transceiver chip (2.23 mm x 1.2 mm) implemented in 180nm CMOS technology includes transceiver front-end, baseband controller, on-chip timer and interface to other system layers. Fabricated chip is integrated into a complete 3 x 3 x 3 mm sensor node including 3-D loop antenna and other functional peripherals as shown in Figure 3.3. Complete sensor system was measured together with custom gateway that realizes proposed sensor initiate protocol as described in Section 3.4, demonstrating a wireless bi-directional communications for 20 meter range. The test set-up is shown in Figure 3.11. Figure 3.12 shows captured waveforms using oscilloscope at the sensor node radio chip, where sparse transmitted pules initializes the communication and receives the message sent from custom gateway after calibration of its center frequency and baseband frequency. During this procedure, another second custom gateway (only receiver is turned on) operates to monitor the RF channel, showing the pulses transmitted by sensor and triggered loop-back RF signals from the working gateway.

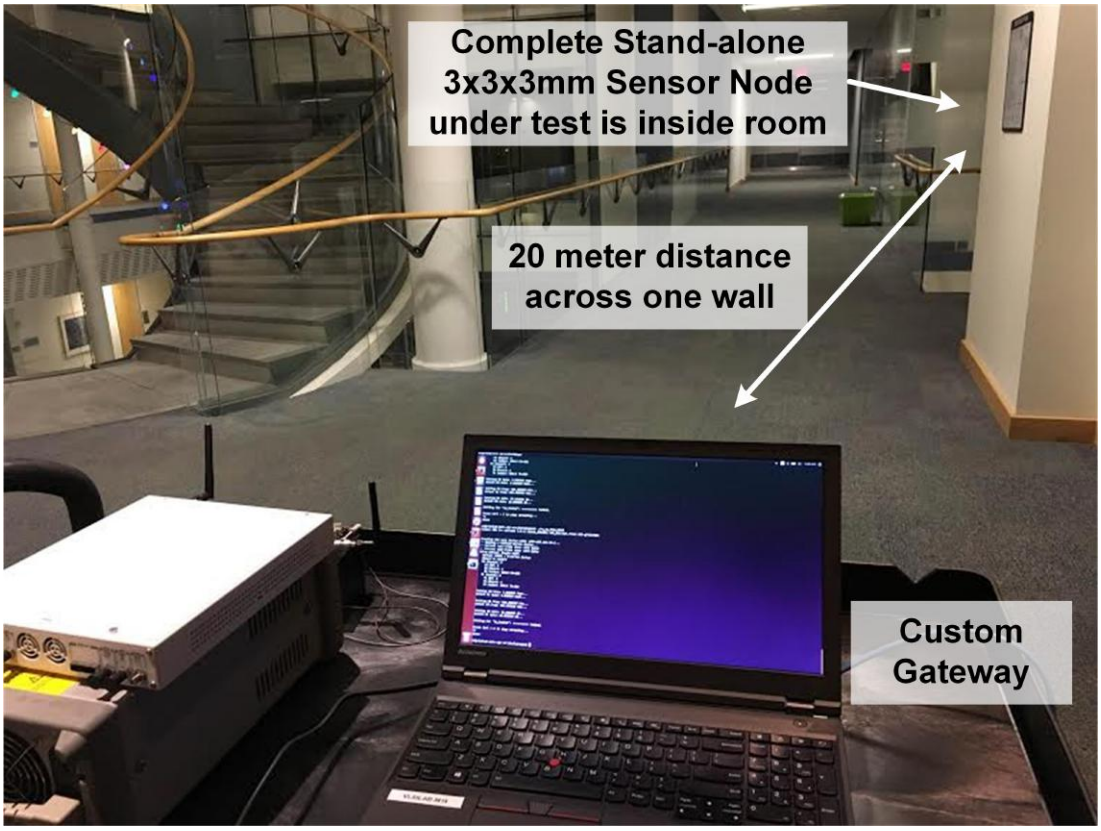

Figure 3.11: Measurement set-up where complete 3x3x3 mm sensor system communicates with custom gateway

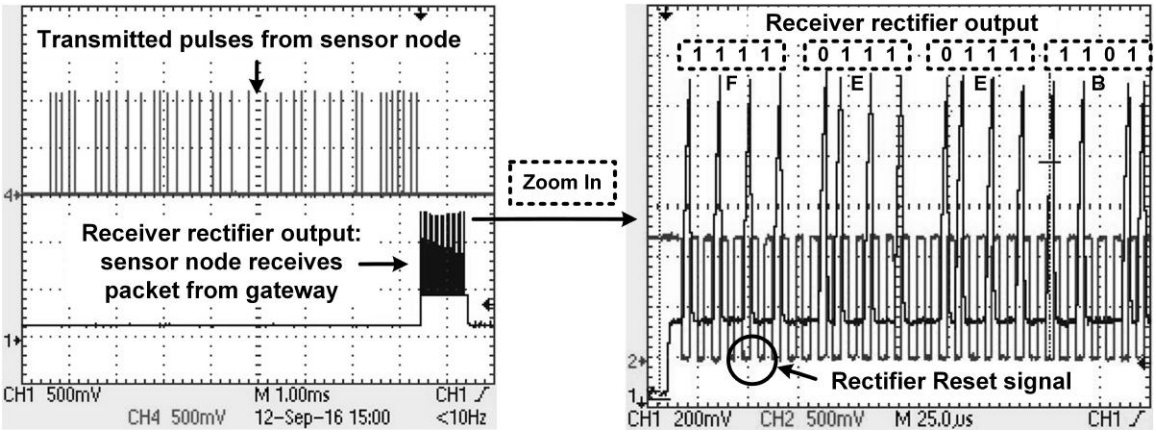

Figure 3.12: Transmitted spase pulses and received return packet (BEEF) measured at the sensor node transceiver

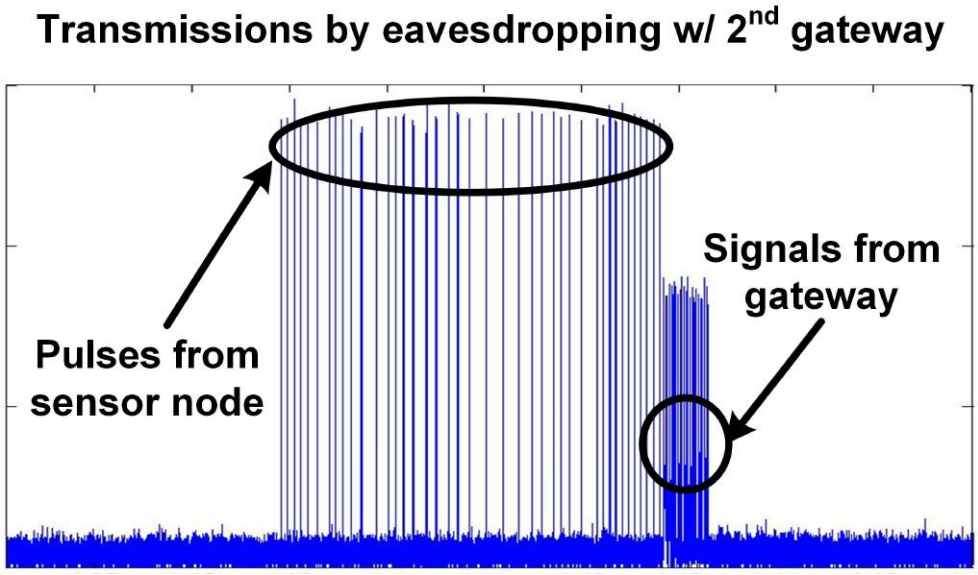

Figure 3.13: Sensor node and gateway communication channel monitoring by another receiver

Figure 3.14 (right) shows the carrier frequency tuning range of the transmitter controlled by the 14b thermometer code of resonant capacitance shown in Figure 3.2. The tuning range is around 40 MHz. EIRP of the transmitter when transmitting a continuous tone was measured using a horn antenna (LB-530-NF) at 2.17m distance. Figure 3.14 (left) is measured EIRP when bias current of power oscillator is tuned, showing that the transmitter EIRP ranges from -45.9 -26.1dBm for 0.52 2mW TX power consumption at 4V supply voltage. Figure 3.14 is the measured EIRP when transmitter consumes maximum power at 2.17m distance.

Figure 3.16 shows the sensitivity measurement result. Because the front-end is co-designed with proposed magnetic antenna and not impedance-matched to 50, the receiver sensitivity cannot be measured via a wired test. Therefore, we measured sensitivity wirelessly via turn- around communication with the gateway realizing proposed sensor initiate synchronization. The received power at sensor node receiver is measured using a horn antenna (LB-530-NF) next to the sensor node. Thus the bit error rate (BER) is thus measured for different received power. Receiver sensitivity was measured to be -93 dBm for 30 kbps data rate with 10^{-3} BER. When QEA bias

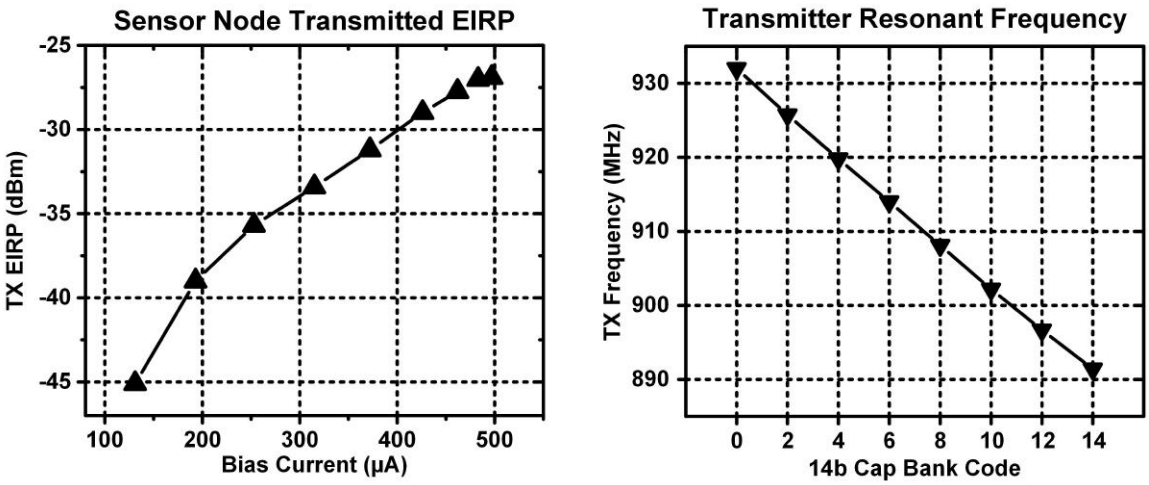

Figure 3.14: Measured transmitter performance

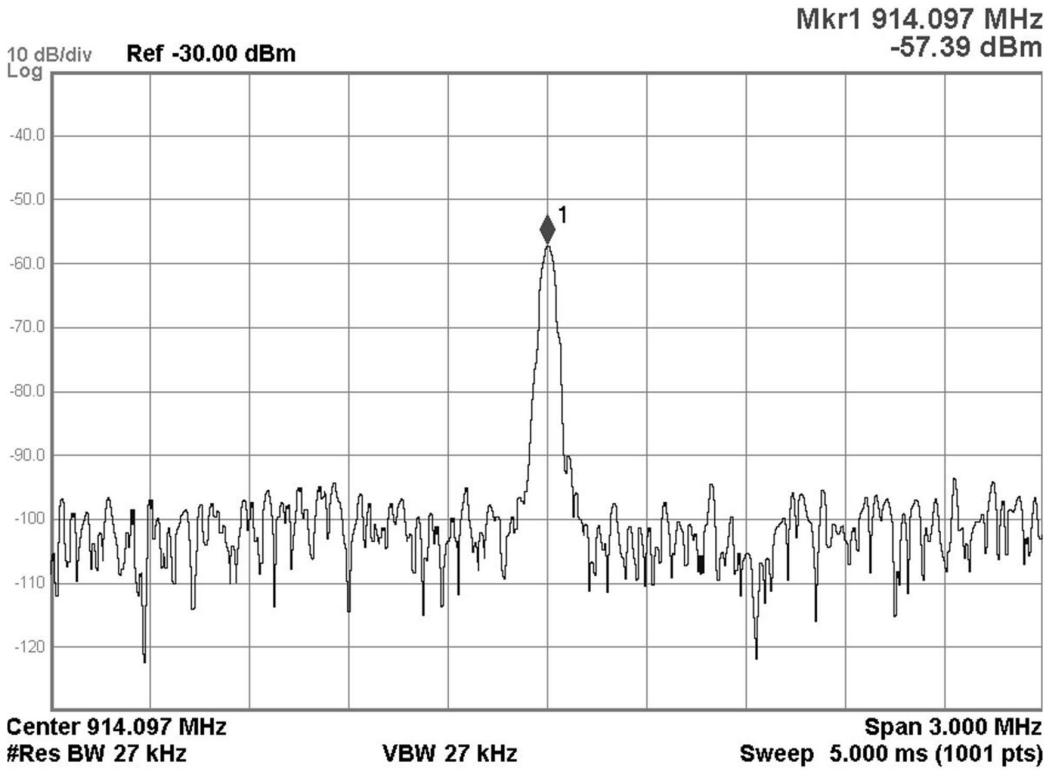

Figure 3.15: Spectrum captured using horn antenna wirelessly at 2.17m

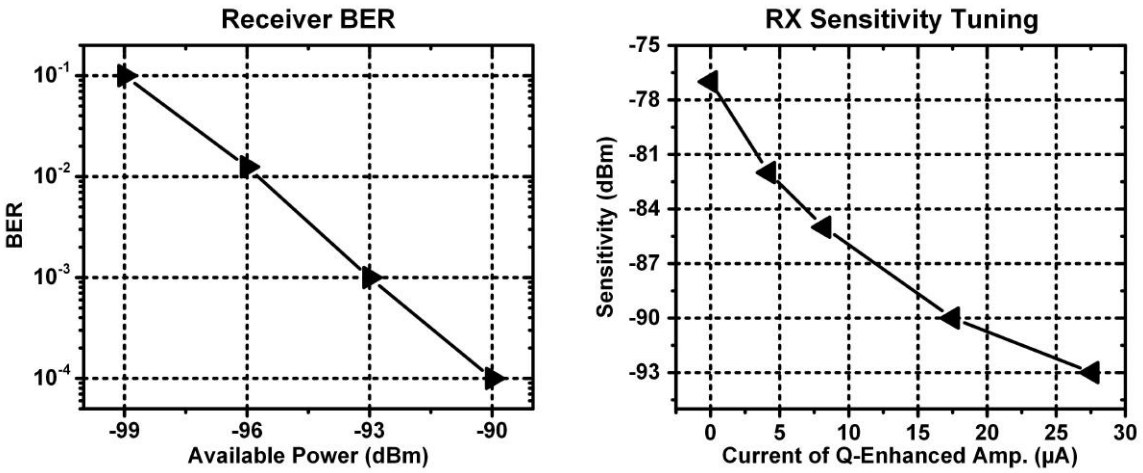

Figure 3.16: Measured receiver performance

current is tuned, it is shown that receiver sensitivity is can be reconfigured. Figure 3.17 summarizes the comparison of implemented radio system with recent related prior work.

3.6 Summary

A fully integrated 3 x 3 x 3 mm radio system is demonstrated for wireless bi-directional communications. It is shown that electrically-small magnetic antenna has better efficiency than electric dipole when finite quality factor of matching passives is considered. Moreover, when ITU model is utilized for NLOS communication in indoor environment, carrier frequency of 915MHz is shown to be optimal for lowest path loss considering efficiency of magnetic antenna. A asymmetric sensor initiate communication protocol was proposed and and implemented on custom gate using FPGA-based software-defined radio platform for real-time demonstration. A complete CMOS transceiver is then co-designed with proposed high-Q 3D loop antenna, consuming 60.6 μW average power at 7 kbps for transmission. The receiver consumes 1.85 mW with a -93 dBm sensitivity at 30 kbps. The complete radio system demonstrates larger 20 meter communication distance with the custom gateway in a indoor

		This Work ISSCC 2017	M. Tabesh JSSC 2015	J. Bohorquez JSSC 2009
Technology		180 nm	65 nm	90 nm
Overall Dimension		$3x3x3\ mm^3$ Complete Sensor Node (incl. Radio Chip + 3D Ant.)	$3.7x1.2\ mm^2$ Radio Chip + Integrated Ant.	$2x1\ mm^2$ Radio Chip (not incl. Loop Ant.)
Antenna		$3x3x2\ mm^3$ 3D Magnetic Antenna	Integrated Antenna	$2.3x2.4\ cm^2$ Loop antenna
Carrier Frequency		915 MHz (TRX)	60GHz (TX) 24GHz (RX)	402-405MHz (TRX)
Measured Range		20m (NLOS)	50 cm	N/A
TX	EIRP (Tone) Testing Method	-26.9 dBm Wireless Testing Incl. $3x3x2\ mm^3$ Ant.	N/A	-37.4 dBm **** Wireless Testing Incl. $2.3x2.4\ cm^2$ Ant.
	Peak Power (Tone)	2 mW	11mW **	350 µW
	Efficiency	32.4% *	N/A	N/A
	Modulation	M-ary Pulse-Pos. Mod.	Multi. Pulse-Pos. Mod.	MSK
	Average Power	60.6 µW	N/A	350 µW
	Data Rate	30bps - 30.3kbps	1.2Mbps - 12Mbps	120 kbps
RX	Technique	Q-Enhanced Amplifier	Backscatter	Super-Regnerative
	Modulation	Binary Pulse-Pos. Mod.	Pulse-Pause Mod.	Sync. OOK
	Sensitivity Testing Method	-93 dBm Wireless Testing Incl. $3x3x2\ mm^3$ Ant.	-10.5 dBm Wired Testing Signal Gen. as Input	-99 dBm Wired Testing Signal Gen. as Input
	Power	1.85 mW	1.5 µW ***	400 µW
	Data Rate	7.8kbps - 62.5kbps	6.5 Mbps	40 kbps

* Calcilated based on measured results: -26.9dBm EIRP, 2mW TX power, antenna eff. 0.21% and directivity 1.5
** Calculated based on simulated results: 250pC total charge for 3 pulses (width 680ps) from 0.9V supply
*** Calculated based on measured results: -48dBm received power at 20 cm away at 406MHz
**** Measured stand-by power reported

Figure 3.17: Comparison Table

NLOS environment. The proposed solution enables long range wireless communication for millimeter-scale computers in NLOS indoor environment, increasing their potential use cases in IoT applications.

CHAPTER IV

A 606μW BLE Transmitter using Transformer-Boost Power Oscillator and Co-designed 3.5x3.5 mm^2 Planar Loop Antenna

4.1 Introduction

Millimeter-scale wireless sensor nodes operating under restricted battery capacity are envisioned to become ubiquitous in IoT applications with constrained space (healthcare, fitness, beacons, etc.), as explained in Section 1.1. Transmitter is a critical block to realize data transfer from mm-scale sensor nodes to other nodes in wireless network. Thus, various designs of transmitters for millimeter-scale computing devices have been presented in recent works [59] [19] [63]. Among those works, custom communication protocols with OOK or pulse-based modulation were commonly utilized to realize low power and simple hardware. However, a specifically designed custom gateway is necessary to communicate with such devices, increasing cost and development life cycle. On the other hand, Bluetooth Low Energy, as an extension from classic Bluetooth, specifies another low-cost modulation of FSK and is widely installed in commercial mobile devices and wearables. Previous low-power BLE transmitters still consume power consumption of several mW [45] [57] [70] [67] [55], which is still large for next-generation energy-constrained applications.

Therefore, it is desired to have a new solution for BLE transmitter with ultra low power consumption (<1 mW), high energy efficiency (> 20%), miniaturized system (millimeter-scale volume) and low cost.In this work, we present a 600μW BLE transmitter with a co-designed 3.5x3.5mm^2 planar loop antenna on printed circuit board, supporting robust and convenient wireless data acquirement (for 10 meter) from a millimeter-scale computing devices to any BLE-compliant mobile or wearable devices. Designing an energy-efficient BLE-compatible transmitter with decent range in millimeter-scale form factor is challenging due to constrained antenna dimension and limited energy source. We addressed those challenges in several ways:

1) A 3.5x3.5mm^2 loop antenna with high quality factor (simulated Q = 110) is implemented considering trade-off between antenna gain and resonant capacitance value;

2) A high-Q digitally switched capacitor array (simulated Q>283) resonates with the high-Q loop antenna at BLE band (around 2.4 GHz), allowing low degradation of antenna gain. Besides high Q, its resolution and total range was designed to meet BLE specifications;

3) A digitally controlled power oscillator (DCPO) based on the high-Q resonator performs frequency generation and power delivery into the antenna. A transformer-boost technique was proposed for DCPO to achieve 1.2x output power level and 3.16x transmit efficiency compared to conventional fashion;

4) By implementing a duty-cycled all-digital phase-locked loop (ADPLL), open-loop GFSK modulation was realized to reduce overall energy consumption from system level.

4.2 Transmitter Architecture

The overall architecture of the proposed BLE transmitter is shown in Figure 4.1. As explained in Section 3.3.1, at electrically-small size (0.028λ), a magnetic dipole

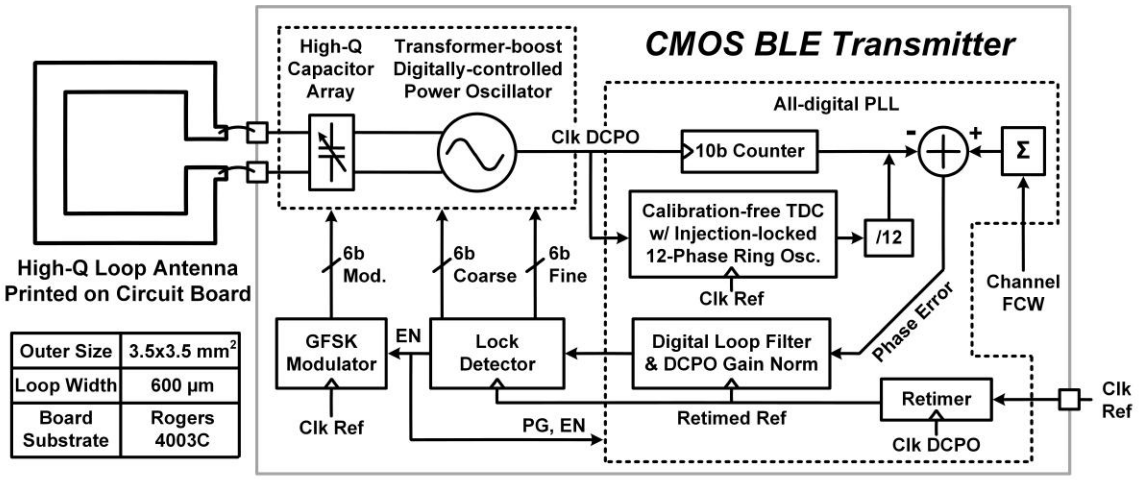

Figure 4.1: Architecture of Proposed BLE Transmitter

antenna achieves better efficiency than an electric dipole considering quality factor of resonant passives. Thus, a 3.5x3.5mm^2 loop antenna with 600μm loop width was implemented on printed circuit board (Rogers 4003C substrate). An integrated capacitor array with high quality factor resonates with designed loop antenna at desired carrier frequency (BLE band). Co-design of antenna and circuits is explained in Section 4.3. A new transformer-boost digitally-controlled power oscillator (DCPO) is proposed for higher transmit efficiency and higher output power. The all-digital PLL (ADPLL) based on counter and TDC [61] is aimed for fast channel frequency settling ($\sim$15μs) and then the GFSK modulator performs BLE packet generation ($\sim$368μs) in a open-loop fashion, which means that ADPLL is shut down after frequency settling for power saving.

4.3 Antenna and Circuits Co-design

In this design, loop antenna dimension is a variable at initial step of overall design. Its dimension has to be designed considering the antenna gain and eventual resonant frequency when utilized in power oscillator.

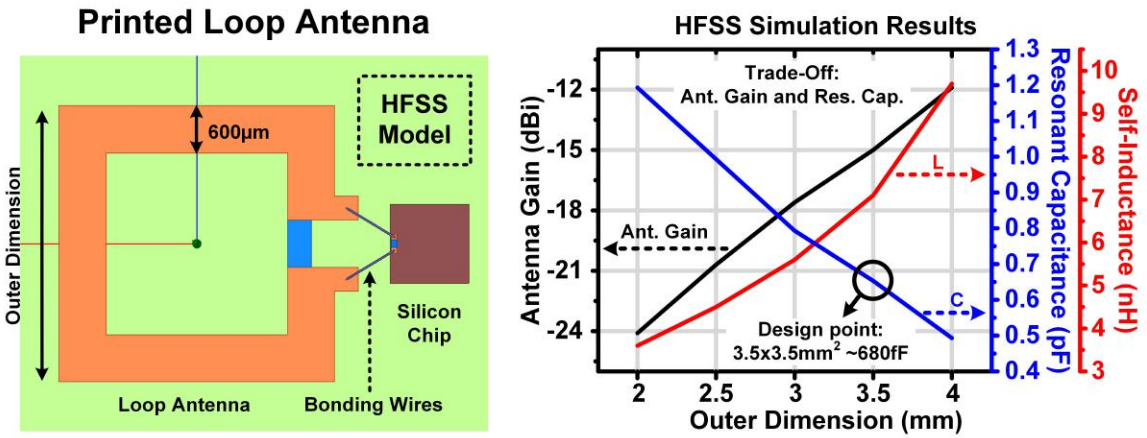

Figure 4.2: Printed loop antenna simulated using HFSS

4.3.1 Analysis of Printed Loop Antenna

To analyze performance of loop antenna, a complete model where antenna is bonded to the chip is built in Ansys HFSS. The substrate of printed circuit board (thickness is 600μm) has dielectric constant of 3.38 and loss tangent of 0.0025 [21]. The chip is modeled as a box of pure silicon with 2x2 mm dimension. HFSS simulation results are shown in Figure 4.2, showing the complete model and the dependence on outer dimension. As dimension increases, antenna gain is increased with fourth power of dimension according to theory [62]. The HFSS simulated antenna gain aligns well with theory. Larger dimension is desired for higher antenna antenna. However, self inductance also increases, reducing self resonant frequency that hinders its usage in power oscillator. Moreover, extra resonant capacitance has to be large enough for routing parasitics and capacitance tuning range, which will be explained in Section 4.3.3. Therefore, 3.5x3.5 mm^2 loop antenna is selected and its HFSS simulation result is shown in Figure 4.3. Simulated capacitance to resonate this antenna at 2.4GHz is around 680fF, allowing design margin for digitally controlled capacitor array and other parasitic capacitance of on-chip structures.

Target Freq.	2.4 GHz
Rad. Efficiency	0.021
Antenna Gain	-15 dBi
Inductance	7 nH
Quality Factor	110
Directivity (magnetic dipole)	1.76 dBi

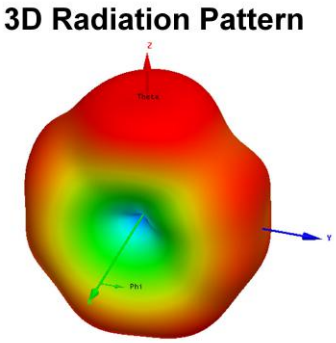

Figure 4.3: Simulated result of 3.5x3.5 mm^2 printed loop antenna

4.3.2 Analysis of Transmitter Efficiency

Figure 4.4 shows general architecture and first-order model of a power oscillator. The loop antenna with inductive imaginary impedance and the capacitor array forms a parallel high-Q resonator at target frequency. The power oscillator with the resonator performs frequency generation and then RF current (I_ANT) circle through loop antenna, inducing electromagnetic radiation. Since the resonator has much larger quality factor (usually >60) than on-chip resonator (limited by on-chip inductor to around 10), the power oscillator based on off-chip resonator consumes much lower current than on-chip LC oscillator. The overall transmit efficiency is given by Equation (4.1).

$$Eff_{TX} = \frac{Q_C}{Q_C + Q_L} \times Eff_{PO} \tag{4.1}$$

In Equation (4.1), Eff_{TX} is transmit efficiency, Q_C and Q_L are quality factor of magnetic antenna and resonant capacitor respectively, EFF_{PO} is power oscillator efficiency. Therefore, Q of capacitor and power oscillator efficiency are desired to be maximized. Furthermore, EIRP is given by Equation (4.2) where G_{ANT} is gain of antenna (omni-directional).

$$EIRP = P_{DC} \times Eff_{TX} \times G_{ANT} \tag{4.2}$$

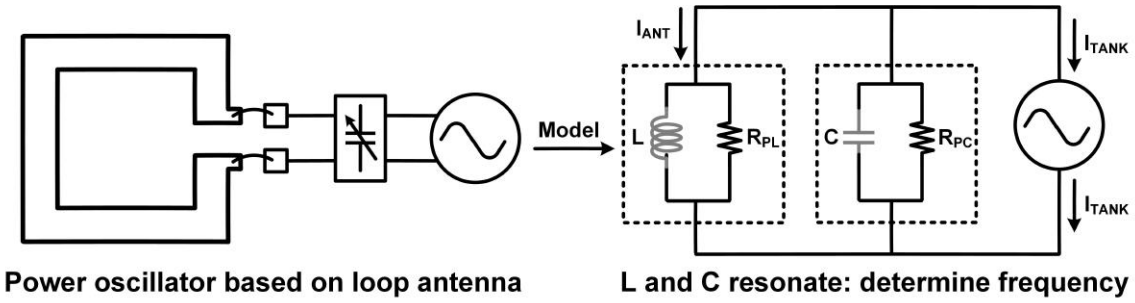

Figure 4.4: General architecture and first-order model of power oscillator

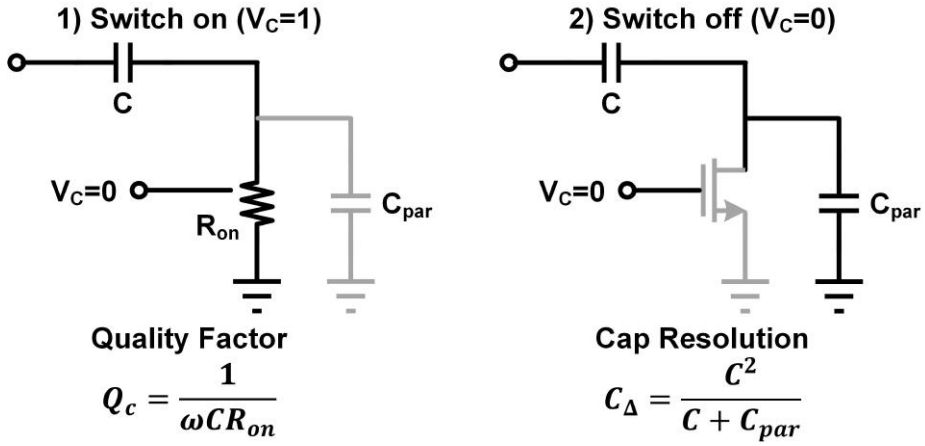

Figure 4.5: Analysis of a basic single-ended digitally switched capacitor

4.3.3 Resonant Capacitor Design

As explained in Section 4.3.2, high quality factor of capacitor is desired so that oscillator power (I_{TANK}) is radiates through loop antenna rather than wasted by equivalent series resistance (ESR) of resonant capacitance (R_{PC}). Meanwhile, resolution and tuning range of the capacitor array have to meet BLE standard. Figure 4.5 shows design trade-off of a basic single-ended digitally switched capacitor. When the switch transistor is turned on ($V_C = 1$), the unit capacitor C is connected and on-resistance (R_{ON}) determines quality factor. When the switch is turned off ($V_C = 0$), parasitic capacitance (mainly from drain to body capacitance) determines resolution. Therefore, a trade-off exists between quality factor and resolution when the switch transistor size (W/L) is designed.

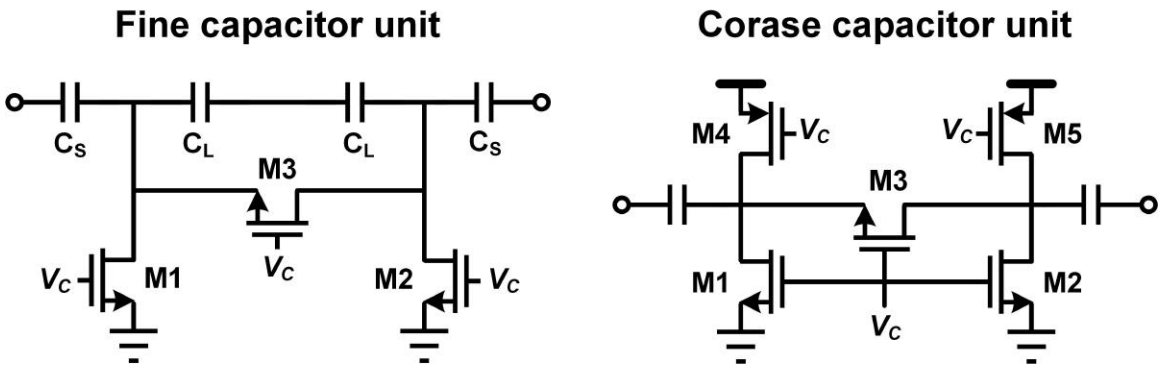

Figure 4.6: Schematics of digitally switched capacitor unit

The schematic of capacitor units that are actually implemented using CMOS is shown in Figure 4.6. For fine capacitor unit, a large capacitor C_L increases C_{par} on purpose, resulting in a ultra-small capacitor resolution [17]. Transistor $M3$ is the main switch, while $M1$ and $M2$ with minimum size are used to make sure drain and source of $M3$ are ground when $V_C = 1$ so that $M3$ is fully turned on. For coarse capacitor unit, for large capacitance resolution, capacitance deviation of C is much larger than C_{par} (as shown in Figure 4.6), making drain/source of M_3 oscillating with large amplitude when $V_C = 0$. Therefore, two PMOS transistors $M4$ and $M5$ with long enough channel length (for very large on-resistance) are utilized to clip drain/source of $M3$. In those designs, high quality factor is achieved by large enough size of LVT transistor switches.

Figure 4.7 shows layout floorplan of resonant capacitor array and simulation and measurement results. There are 3 arrays: fine, coarse and modulating array. Top two metal layers with $2.5mu$m width were interchangeably used to interconnect units, avoiding degradation of array Q and minimizing coupling capacitance. Measured frequency resolution and range of power oscillator show compliance to BLE compliant.

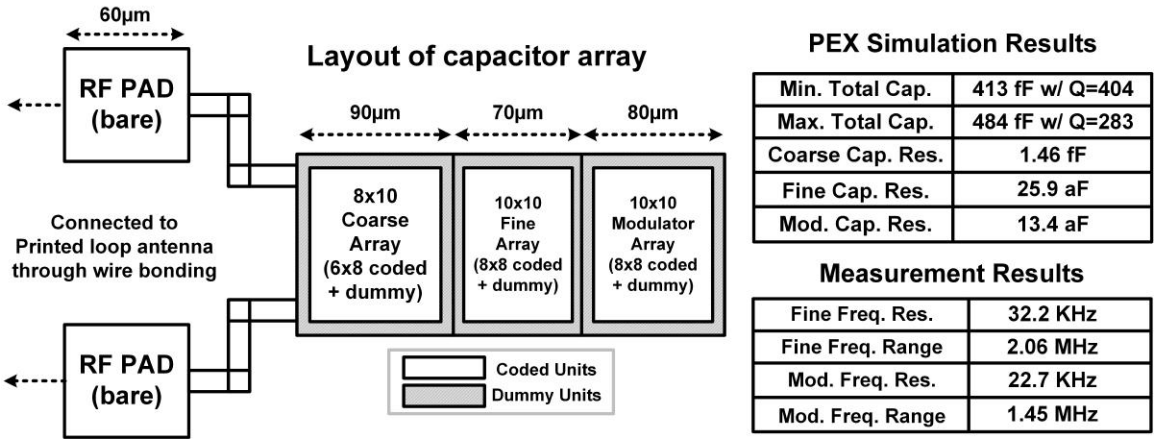

Figure 4.7: Layout floorplan of resonant capacitor array and simulation and measurement results

4.4 Transformer-boost Power Oscillator

As shown in Section 4.3.2, efficiency of power oscillator is desired to be as high as possible. Conventional class-B power oscillator with a tail current bias has a configuration same as the one shown in Figure 3.5. This configuration with planar loop antenna in this work is studied and PEX simulation result is shown in Figure 4.9 with green color. To realize larger output power, tail current can be increased and oscillation voltage increases, resulting in higher efficiency until the power oscillator leaves current limited region and enters voltage limited region [28]. Therefore, its peak transmit efficiency is achieved when tail current is tuned at the crossing region between current limited and voltage limited regions, which is simulated to be 22 μW output power with 28% efficiency. As bias current keeps increasing, output power increases but efficiency drops dramatically. Removing the tail current source results in maximum output power, limited by supply voltage, as shown in FIgure 4.9 with red color. PEX simulation shows that maximum output power of conventional power oscillator is 75 μW with 8.8% efficiency.

In order to improve output power and corresponding transmit efficiency, a transformer-boost technique is proposed in this work. Resulted schematic is shown in Figure 4.8.

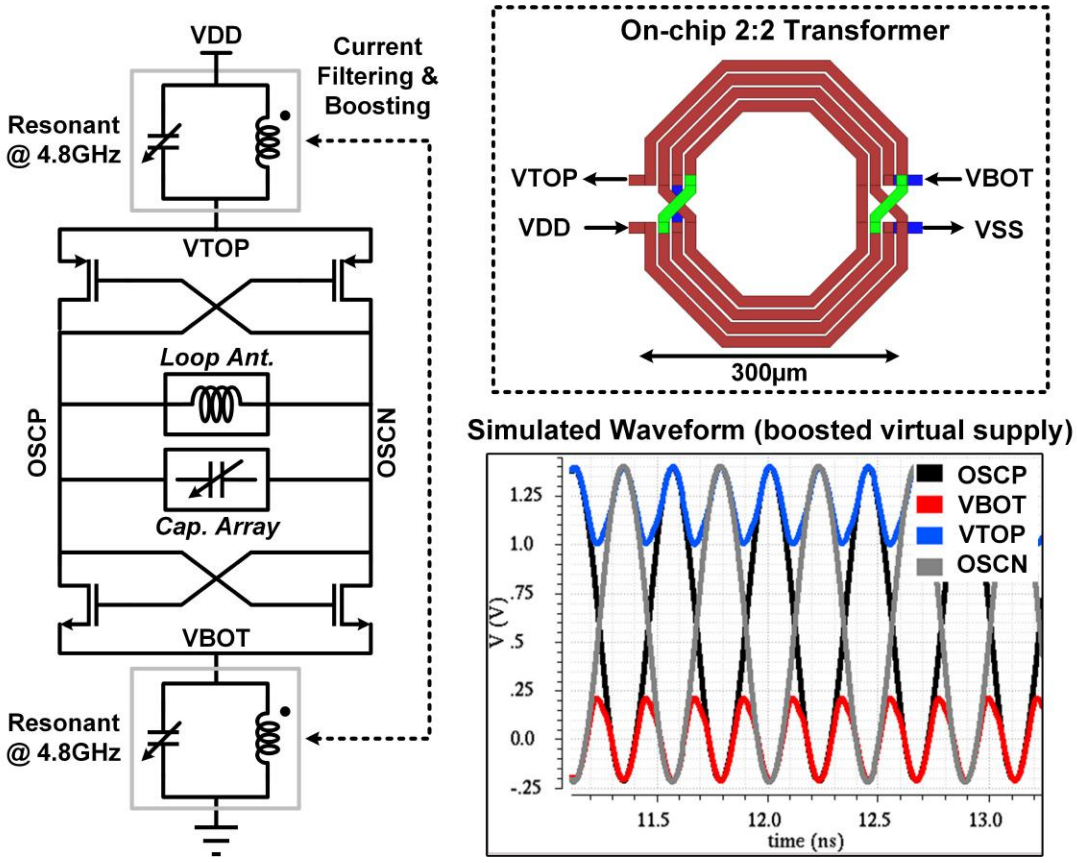

Figure 4.8: Schematic of proposed transformer-bosst power oscillator

With tail current source removed, the transformer is inserted to top and bottom of cross-coupled pair, forming two resonant tanks with tunable capacitor array at second harmonic frequency (4.8GHz). The resonant tanks exhibit a maximum impedance at 4.8GHz and thus second order current produces a swing voltage at VTOP and VBOT. Therefore, virtual supplies are generated, which boosts the output power by 1.2x. Another advantage of virtual supply is higher transmit efficiency. The reason is that when OSCP=OSCN, difference of VTOP and VBOT is smaller than actual supply voltage, resulting in a reduced DC current. Simulated result shows that proposed transformer-boost power oscillator generates 90 μW output power with 28% transmit efficiency. The 2:2 transformer is implemented on-chip using top metal layer achieving k=0.75 and Q=12.

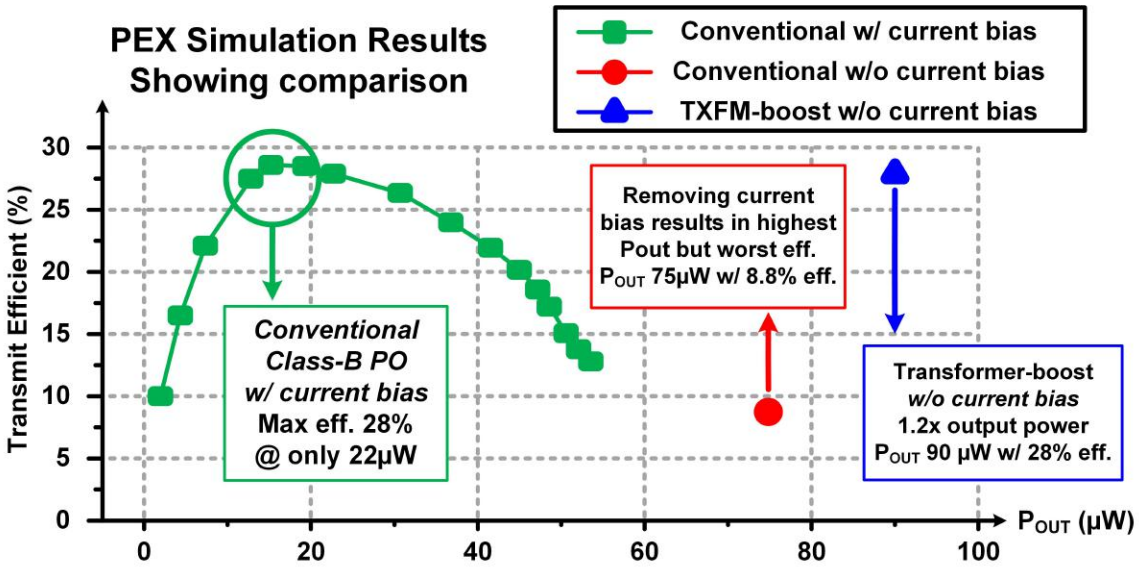

Figure 4.9: PEX simulation results showing comparison between proposed power oscillator and conventional configuration

4.5 Open-loop Modulation

Proposed transmitter utilizes open-loop GFSK modulation for energy saving [54] [5]. When BLE packet is ready at baseband, the ADPLL locks the frequency of DCPO to desired channel after 15 μs. An on-the-fly lock detector monitors the settling process of DCPO control word and averages it to eliminate dithering effect. When locking is achieved (triggered by lock detector), ADPLL is disabled and GFSK modulator is activated for packet length ($\sim$15μs). The open-loop nature eliminates the necessity to implement a high-resolution time-to-digital converter (TDC) [30]. Thus, we implemented an injection-locked TDC based on a 12-phases pseudo differential ring oscillator with 35ps resolution to avoid DCPO period calibration as shown in Figure 4.10. Measured power consumption of TDC is 280 μW. Ring oscillator frequency is tunable by bias current.

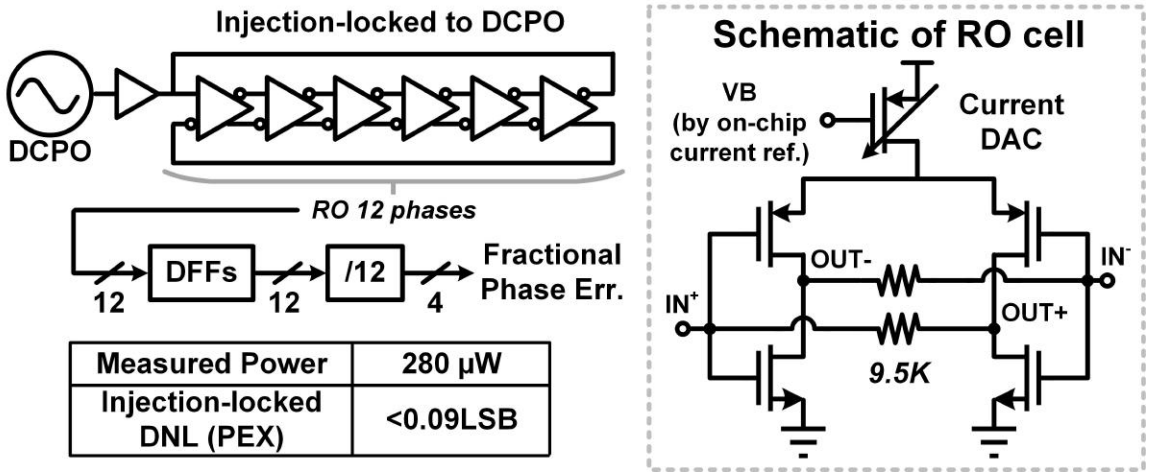

Figure 4.10: Schematic of TDC based on injection-locked ring oscillator

4.6 Measurement Results

Proposed BLE transmitter was fabricated using CMOS 65nm technology. Figure 4.11 shows the chip micrograph. Two pads connected to the loop antenna are on top side of the chip. Floorplan of antenna pads and corresponding resonant capacitor arrays are explained in Section 4.3.3.

The transformer-boost power oscillator consumes 445 μA from 1.2V power supply. The phase noise measured using spectrum analyzer is shown in Figure 4.12. External commercial low-noise amplifiers are used to boost output power level in order for low phase noise measurement. The oscillator has -118.45 dBc/Hz at 1MHz frequency offset when output frequency is around 2.48GHz. Measured transmitted harmonics is shown in Figure 4.13. HD2 is -47dBc and HD3 is -52dBc. Both of them are below BLE specification of -41.5dBc.

To measure the modulation performance of designed transmitter, transient and spectrum measurements were performed. Figure 4.14 shows transient result with modulation of frequency. The frequency drift is ¡10KHz during a 368 μs packet. The packet starts with preamble of 10101010 and peak-to-peak frequency deviation is 500 KHz, meeting the requirement of BLE standard. Figure 4.15 is output spectrum when

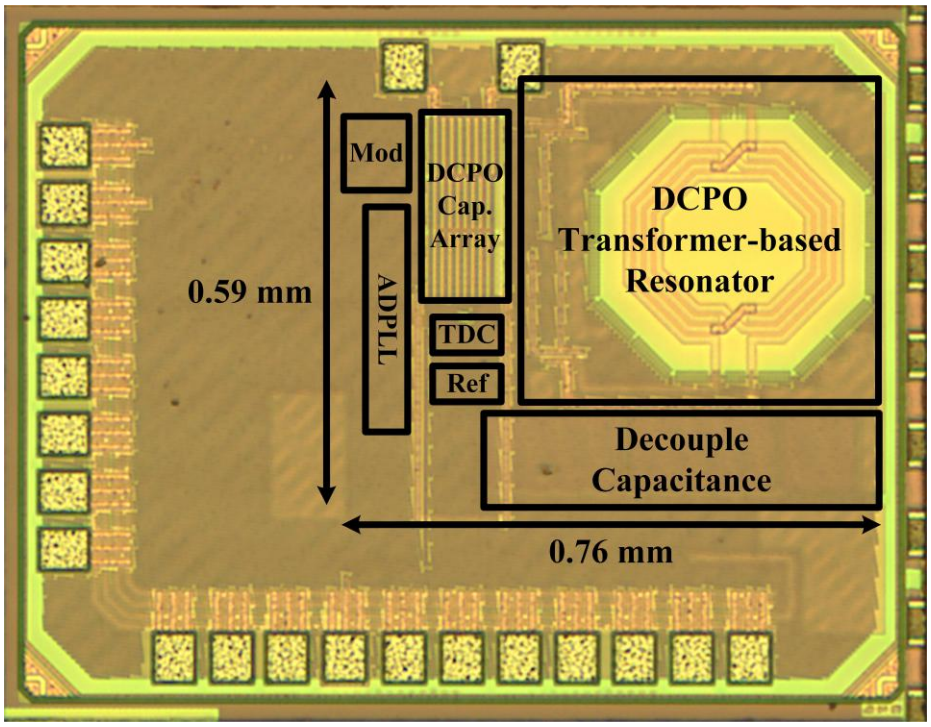

Figure 4.11: Die Photo

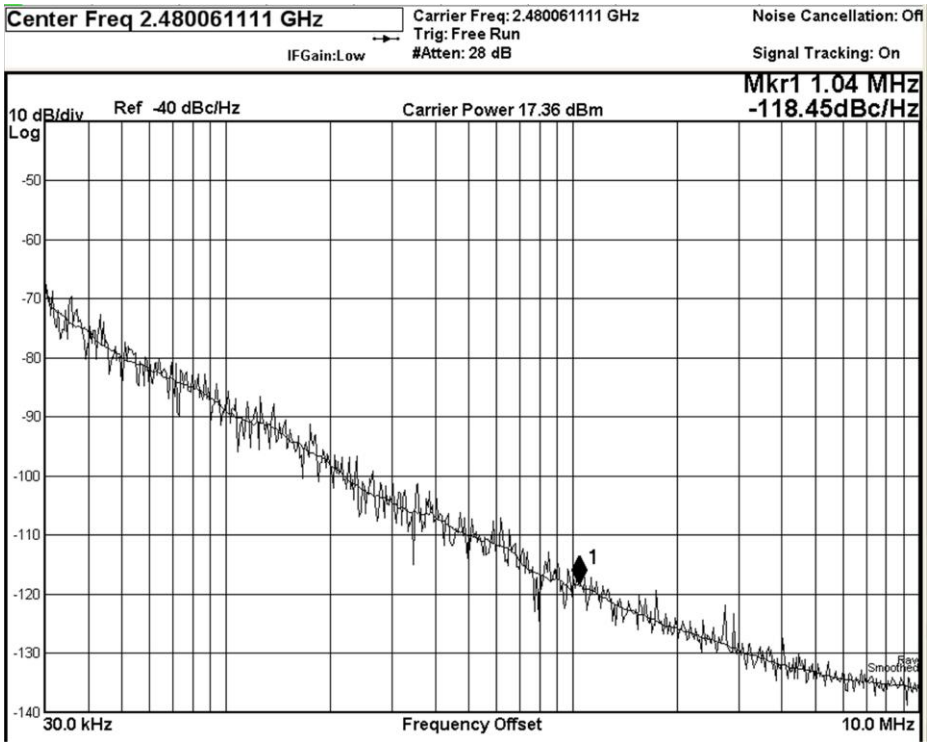

Figure 4.12: Measured phase noise of transformer boost power oscillator

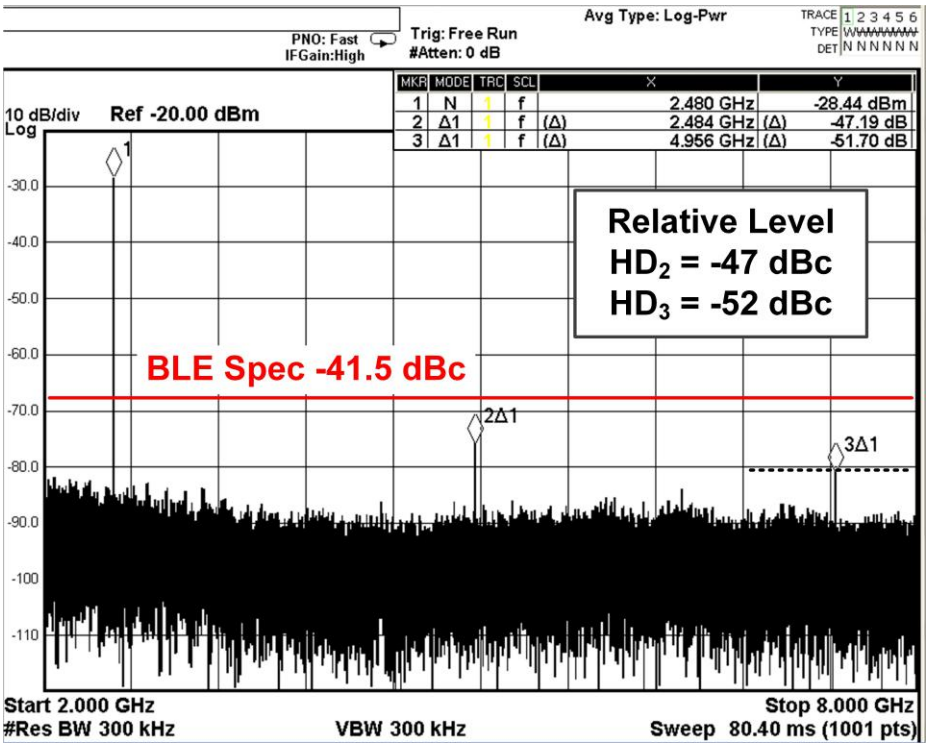

Figure 4.13: Measured transmission harmonics

transmitting GFSK-modulated signal, which is below BLE spectral mask. Figure 4.16 shows measured burst-mode eye diagram. The FSK error is only 2.1%.

Wireless testing is performed to measure EIRP. Figure 4.16 is the photo of prototype wireless circuit board with dimension of 4.5x18.6 mm^2. The average power for transmitting a 368μs packet is 606μW dominated by power oscillator.

4.7 Summary

An energy-efficient Bluetooth Low Energy (BLE) transmitter using a 3.5x3.5 mm^2 printed loop antenna is presented to enable BLE wireless communication for millimeter-scale computer. Proposed transmitter based on loop antenna and power oscillator was fabricated in CMOS 65nm technology. The dependence of loop antenna performance on its outer dimension is analyzed to determine maximum dimension. Integrated high-Q resonant capacitor arrays are designed for high transmit efficiency.

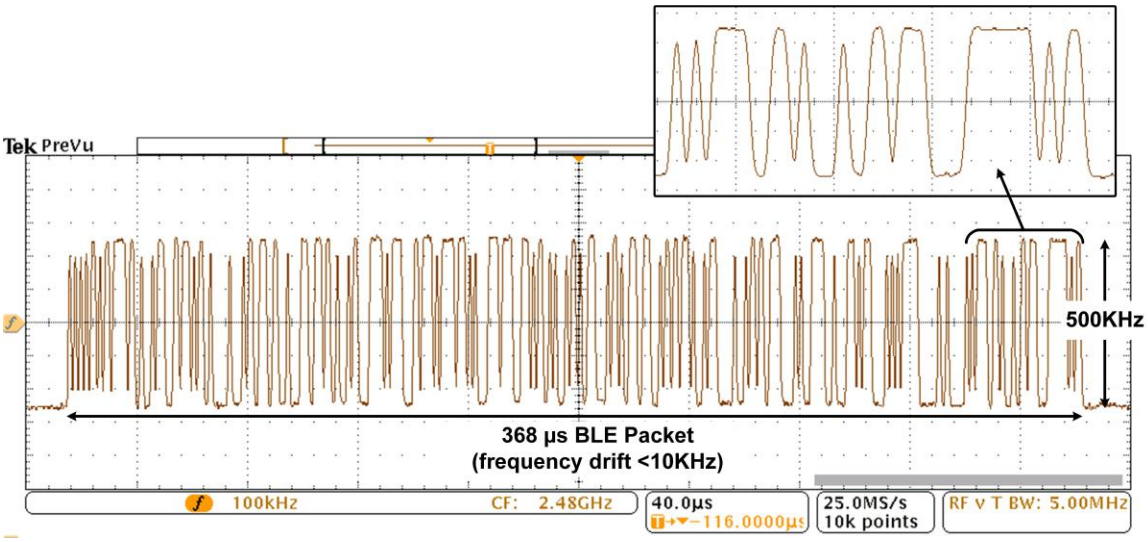

Figure 4.14: Measured transient of power oscillator frequency showing GFSK modulation

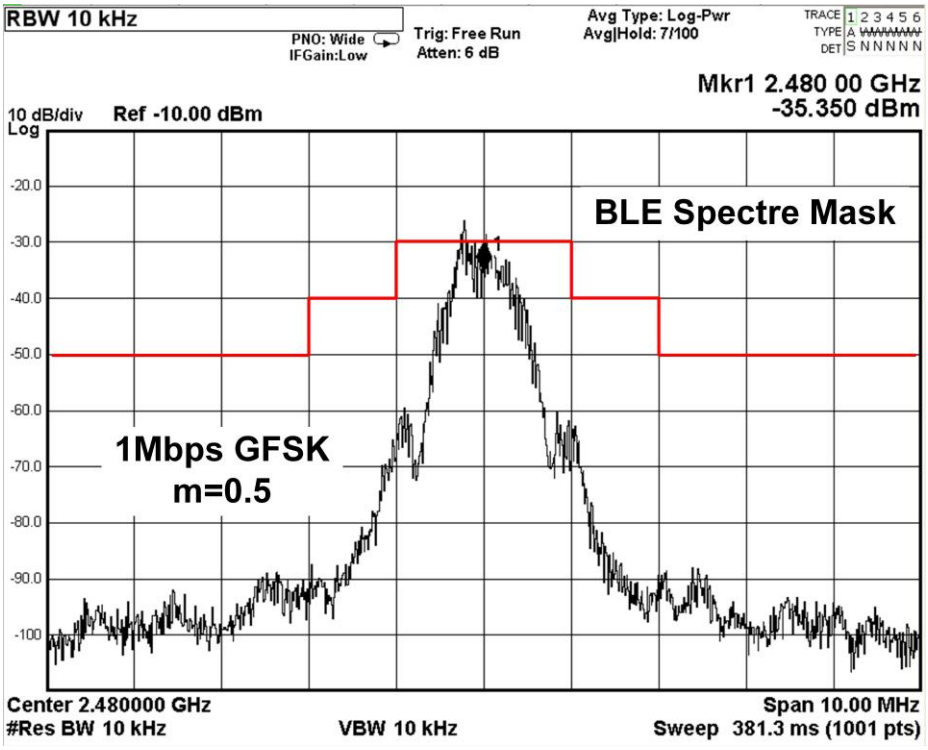

Figure 4.15: Measured spectrum when transmitting GFSK modulated RF signal

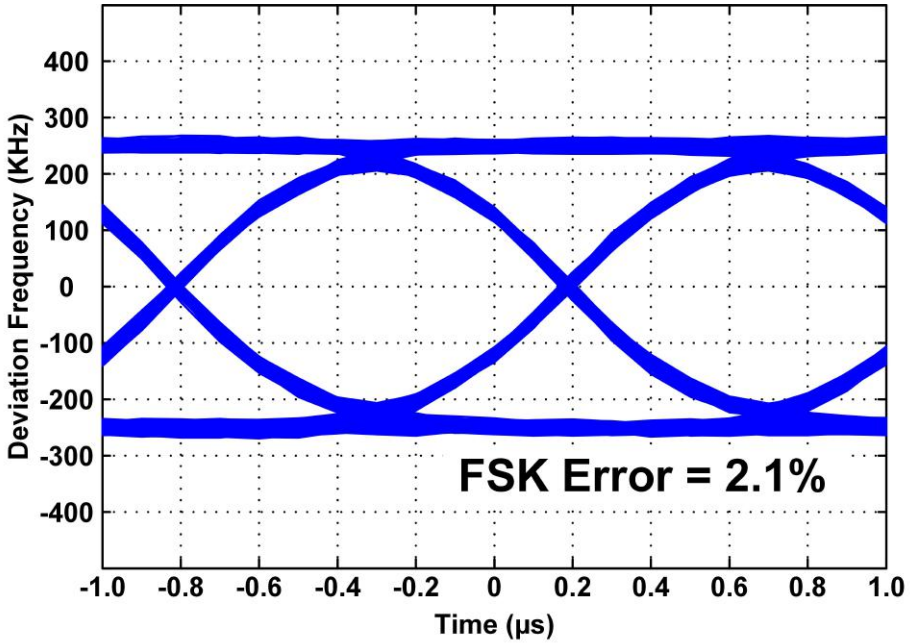

Figure 4.16: Measured burst-mode eye diagram

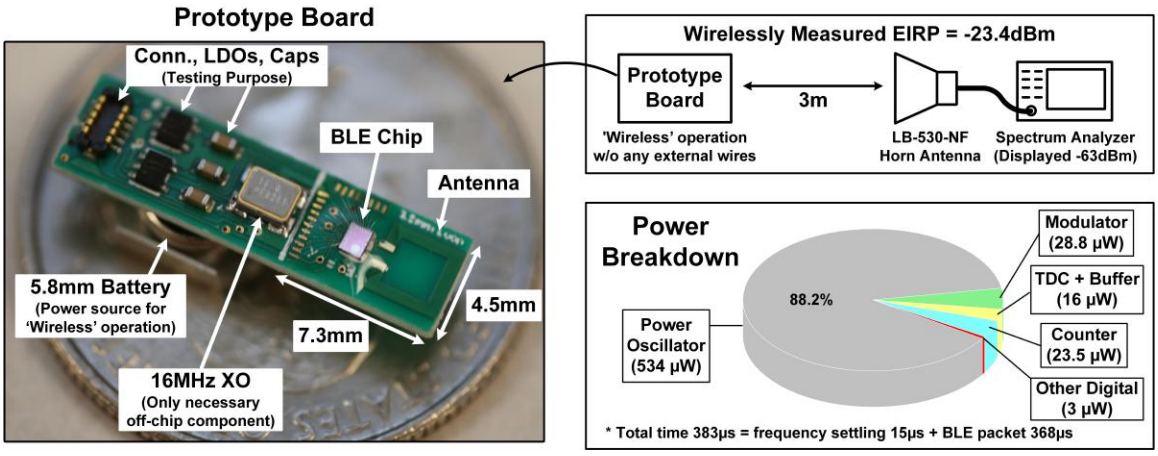

Figure 4.17: Prototype wireless circuit board and wirelessly measured EIRP with system power breakdown

		This Work	ISSCC 2017 Chuo et al.	JSSC 2015 Tabesh et al.	JSSC 2016 Babaie et al.	ISSCC 2015 Liu et al.	RFIC 2018 Chen et al.	JSSC 2011 Lei et al.
Technology		65 nm	180 nm	65 nm	28 nm	40 nm	40 nm	130 nm
Co-Designed Antenna		3.5x3.5 mm^2 Planar Loop	3x3x2 mm3 3D Loop	2.5 mm On-Chip Dipole	N/A	N/A	N/A	N/A
Carrier Frequency		2.4 GHz	915 MHz	60 GHz	2.4 GHz	2.4 GHz	2.4 GHz	400MHz
Standard		BLE	Propritary	Propritary	BLE	BLE	BLE	MICS
Modulation		GFSK	PPM	PPM	GFSK	GFSK	GFSK	BFSK
Data Rate		1 Mbps	30.3kbps	1.2 Mbps	1 Mbps	1 Mbps	1 Mbps	200 kbps
Supply Voltage		1.2 V	4 V	0.9 V	0.5/1 V	1 V	0.6 V	N/A
Power Consumption		0.61 mW [1]	2 mW	11 mW [4]	3.6 mW	4.2 mW	0.49 mW	0.09 mW
Energy Per Bit		0.61 nJ/b	66 nJ/b	9.1 nJ/b	3.6 nJ/b	4.2 nJ/b	0.49 nJ/b	0.45 nJ/b
TX Output Power		-8.4 dBm [2]	-2 dBm	-3 dBm	0 dBm	-2 dBm	-19 dBm	-17 dBm
Overall Efficiency		23.6%	32.4% [3]	4.5%	28%	15%	2.6%	22%
Modulation Error		2.1%	N/A	N/A	2.7%	4.8%	9%	N/A
Osc. Phase Noise @ 1MHz (dBc/Hz)		-118.5	N/A	N/A	-116	-110	-85	-104 [5]
Spur Level	HD2 (dBc)	-47	N/A	N/A	-50	-47	-42	N/A
	HD3 (dBc)	-52	N/A	N/A	-47	-51	-45	N/A

[1] Average power for transmitting one BLE packet w/ open-loop modulation. Power of external commercial XO is not included.
[2] Calculated based on wireless testing results: EIRP -23.4dBm and antenna gain -15dBi (omni-directional).
[3] Power oscillator only and high-Q off-chip capacitor used.
[4] Calculated based on simulated results: 250pC total charge for 3 pulses (width 680ps) from 0.9V supply.
[5] Measured phase noise of frequency multiplier output.

Figure 4.18: Comparison with recent low-power transmitters

A new technique using transformer-based resonator to improve performance of power oscillator, resulting in 1.2x output power and 3.16x transmit efficiency compared to conventional fashion (PEX simulation). Operating with designed loop antenna, the power oscillator is measured to generate -23.4dBm EIRP with 27% efficiency, consuming 445 μA current from 1.2V supply. When powered by a 5.8mm micro battery, the transmitter consumes only 0.61 nJ/bit (610μW average power) when transmitting 368 μs BLE packet with 1 Mbps. The transmitter demonstrates >8 meter wireless communication to typical mobile phones.

CHAPTER V

Conclusions and Future Work

This dissertation focuses on RF wireless systems with millimeter-scale dimensions and high energy efficiency, expanding the potential use cases of millimeter-scale computers. It is challenging to develop such RF wireless systems due to volume constraints. In order to solve such challenging problems, I studied, analyzed and understood the problems and then proposed novel solutions from different perspectives, including an electrically-small antenna, transceiver architecture and implementation using integrated circuits, system-level communication protocols, hardware fabrication and packaging, and others. The proposed solutions were implemented in three prototype RF wireless systems for demonstration and verification.

First prototype is a 10-mm^3 near-field radio system designed for implantable healthcare applications with tight space constraints, such as intraocular monitors, inner ear implants, neural sensors, and others. An inductive-coupled link is utilized since a magnetic field is less absorbed by tissue compared with an electric field. The fabricated radio system was measured to demonstrate a wireless communication distance greater than 20 cm, substantially expanding emerging applications of implantable sensors. The major contributions of this work include 1) new concept, theory, and design flow of antenna and carrier frequency co-design to maximize near-field inductive-coupled link strength and the resulting communication range; 2) a new

power oscillator configuration called 'pulse inject oscillator' with a 1-cycle start-up circuit and high-efficiency oscillation-sustaining feedback loop in CMOS technology; 3) a new transceiver architecture including co-designed circuits, sparse PPM transmitter and continuous OOK receiver for energy-constrained millimeter-scale computers; and 4) a new system-level communication protocol called 'sensor initiate synchronization, enabling the replacement of off-chip crystal oscillators by inaccurate on-chip time.

The second prototype is a 3x3x3 mm^3 far-field 915 MHz radio system with 20 meter NLOS range in an indoor environment. This work makes a significant contribution to incorporating millimeter-scale computers into ubiquitous IoT networks. The major contributions of this work include 1) the analysis of electrically-small magnetic dipole and electric dipole antennas with millimeter-scale dimensions, especially considering the quality factor of matching passives; 2) new concept and implementation of antenna and carrier frequency co-design to optimize path loss considering millimeter-scale antenna efficiency and ITU indoor model for NLOS communication; and 3) implementation of sensor initiated synchronization on an integrated baseband processor for controlling the operation of transceiver and power management.

The third prototype is a 606 μW BLE transmitter using a 3.5x3.5 mm^2 planar loop antenna, enabling more connectivity of millimeter-scale antennas with ubiquitous IoT BLE-compliant devices. The fabricated transmitter demonstrates approximately 10 m wireless communication to any BLE-compliant mobile phone. The major contributions of this work include 1) a new BLE transmitter architecture based on a planar loop antenna, power oscillator, GFSK modulator and ADPLL; 2) co-design of a millimeter-scale loop antenna and integrated capacitor array for BLE-compliant transmission with high efficiency; and 3) a new power oscillator technique using transformer-based resonator for improved output power and transmission efficiency.

The work presented in this dissertation improves use cases of millimeter-scale computers by identifying new methods for improving wireless communication. The

impact of this work is significant in the age of the IoT, where everything will be connected in daily life. However, many issues remain to be explored and solved in future work. First, for an implanted near-field radio system with an inductive-coupled link, the position of implantation will affect antenna performance significantly and thus the communication range due to variant temperature, humidity, and electrical performances of tissue (such as dielectric constant and loss tangent). The variation must be compensated for with a new method, which is challenging if a crystal-less solution is desired. Secondly, for a far-field millimeter-scale radio, although sub-1 GHz is desired for NLOS, as presented in Chapter III, millimeter-wave with 10 s of GHz would be preferred for LOS applications. Thus, more work on the design and optimization of energy efficiency is necessary at the transceiver architecture or circuit level. Third, the antennas implemented in this work are off-chip, requiring more fabrication process and packaging. It will be interesting to explore the possibility of integrated antennas in semiconductor technology such as CMOS. Fourth, to realize a complete BLE transceiver, it will be interesting to explore the possibility of a CMOS BLE receiver co-designed with a mm-scale loop antenna together with the BLE transmitter presented in Chapter IV.

BIBLIOGRAPHY

BIBLIOGRAPHY

[1] Ammar Abdo, Mesut Sahin, David S Freedman, Elif Cevik, Philipp S Spuhler, and M Selim Unlu. Floating light-activated microelectrical stimulators tested in the rat spinal cord. *Journal of neural engineering*, 8(5):056012, 2011.

[2] Jonas Andersson. Implantable heart stimulator, February 24 2004. US Patent 6,697,672.

[3] Bryan Atwood, Brett Warneke, and Kristofer SJ Pister. Preliminary circuits for smart dust. In *Proceedings of the 2000 Southwest Symposium on Mixed-Signal Design, San Diego, California*, pages 87–92, 2000.

[4] Luigi Atzori, Antonio Iera, and Giacomo Morabito. The internet of things: A survey. *Computer networks*, 54(15):2787–2805, 2010.

[5] Masoud Babaie, Feng-Wei Kuo, Huan-Neng Ron Chen, Lan-Chou Cho, Chewn-Pu Jou, Fu-Lung Hsueh, Mina Shahmohammadi, and Robert Bogdan Staszewski. A fully integrated bluetooth low-energy transmitter in 28 nm cmos with 36% system efficiency at 3 dbm. *IEEE Journal of Solid-State Circuits*, 51(7):1547–1565, 2016.

[6] Aydin Babakhani, Xiang Guan, Abbas Komijani, Arun Natarajan, and Ali Hajimiri. A 77-ghz phased-array transceiver with on-chip antennas in silicon: Receiver and antennas. *IEEE Journal of Solid-State Circuits*, 41(12):2795–2806, 2006.

[7] Suyoung Bang, Allan Wang, Bharan Giridhar, David Blaauw, and Dennis Sylvester. A fully integrated successive-approximation switched-capacitor dc-dc converter with 31mv output voltage resolution. In *Solid-State Circuits Conference Digest of Technical Papers (ISSCC), 2013 IEEE International*, pages 370–371. IEEE, 2013.

[8] Gordon Bell. Bell's law for the birth and death of computer classes: A theory of the computer's evolution. *IEEE Solid-State Circuits Society Newsletter*, 13(4):8–19, 2008.

[9] Steven R Best and Arthur D Yaghjian. The lower bounds on q for lossy electric and magnetic dipole antennas. *IEEE Antennas and Wireless Propagation Letters*, 3(1):314–316, 2004.

[10] SIG Bluetooth. Bluetooth core specification 5.0, 2016.

[11] Jose L Bohorquez, Anantha P Chandrakasan, and Joel L Dawson. A 350 μw cmos msk transmitter and 400 μw ook super-regenerative receiver for medical implant communications. *IEEE Journal of Solid-State Circuits*, 44(4):1248–1259, 2009.

[12] Jayant Charthad, Nemat Dolatsha, Angad Rekhi, and Amin Arbabian. System-level analysis of far-field radio frequency power delivery for mm-sized sensor nodes. *IEEE Transactions on Circuits and Systems I: Regular Papers*, 63(2):300–311, 2016.

[13] Gregory Chen, Matthew Fojtik, Daeyeon Kim, David Fick, Junsun Park, Mingoo Seok, Mao-Ter Chen, Zhiyoong Foo, Dennis Sylvester, and David Blaauw. Millimeter-scale nearly perpetual sensor system with stacked battery and solar cells. In *Solid-State Circuits Conference Digest of Technical Papers (ISSCC), 2010 IEEE International*, pages 288–289. IEEE, 2010.

[14] Gregory Chen, Hassan Ghaed, Razi-ul Haque, Michael Wieckowski, Yejoong Kim, Gyouho Kim, David Fick, Daeyeon Kim, Mingoo Seok, Kensall Wise, et al. A cubic-millimeter energy-autonomous wireless intraocular pressure monitor. In *Solid-State Circuits Conference Digest of Technical Papers (ISSCC), 2011 IEEE International*, pages 310–312. IEEE, 2011.

[15] Yajing Chen, Nikolaos Chiotellis, Li-Xuan Chuo, Carl Pfeiffer, Yao Shi, Ronald G Dreslinski, Anthony Grbic, Trevor Mudge, David D Wentzloff, David Blaauw, et al. Energy-autonomous wireless communication for millimeter-scale internet-of-things sensor nodes. *IEEE Journal on Selected Areas in Communications*, 34(12):3962–3977, 2016.

[16] Yen-Po Chen, Dongsuk Jeon, Yoonmyung Lee, Yejoong Kim, Zhiyoong Foo, Inhee Lee, Nicholas B Langhals, Grant Kruger, Hakan Oral, Omer Berenfeld, et al. An injectable 64 nw ecg mixed-signal soc in 65 nm for arrhythmia monitoring. *IEEE Journal of Solid-State Circuits*, 50(1):375–390, 2015.

[17] Vamshi Krishna Chillara, Yao-Hong Liu, Bindi Wang, Ao Ba, Maja Vidojkovic, Kathleen Philips, Harmke de Groot, and Robert Bogdan Staszewski. 9.8 an 860μw 2.1-to-2.7 ghz all-digital pll-based frequency modulator with a dtc-assisted snapshot tdc for wpan (bluetooth smart and zigbee) applications. In *Solid-State Circuits Conference Digest of Technical Papers (ISSCC), 2014 IEEE International*, pages 172–173. IEEE, 2014.

[18] Myungjoon Choi, Suyoung Bang, Tae-Kwang Jang, David Blaauw, and Dennis Sylvester. A 99nw 70.4 khz resistive frequency locking on-chip oscillator with 27.4 ppm/^{o}c temperature stability. In *VLSI Circuits (VLSI Circuits), 2015 Symposium on*, pages C238–C239. IEEE, 2015.

[19] Li-Xuan Chuo, Yao Shi, Zhihong Luo, Nikolaos Chiotellis, Zhiyoong Foo, Gyouho Kim, Yejoong Kim, Anthony Grbic, David Wentzloff, Hun-Seok Kim, et al. 7.4 a 915mhz asymmetric radio using q-enhanced amplifier for a fully integrated 3× 3× 3mm 3 wireless sensor node with 20m non-line-of-sight communication. In *Solid-State Circuits Conference (ISSCC), 2017 IEEE International*, pages 132–133. IEEE, 2017.

[20] Federal Communications Commission et al. Understanding the fcc regulations for low-power, non-licensed transmitters. *Office of Engineering and Technology*, 34, 1993.

[21] Rogers Corperation. R04000 series: High frequency circuit materials. *RO4000 Series datasheet*, 2015.

[22] Ming Ding, Xiaoyan Wang, Peng Zhang, Yuming He, Stefano Traferro, Kenichi Shibata, Minyoung Song, Hannu Korpela, Keisuke Ueda, Yao-Hong Liu, et al. A 0.8 v 0.8 mm 2 bluetooth 5/ble digital-intensive transceiver with a 2.3 mw phase-tracking rx utilizing a hybrid loop filter for interference resilience in 40nm cmos. In *Solid-State Circuits Conference-(ISSCC), 2018 IEEE International*, pages 446–448. IEEE, 2018.

[23] Matthew Fojtik, Daeyeon Kim, Gregory Chen, Yu-Shiang Lin, David Fick, Junsun Park, Mingoo Seok, Mao-Ter Chen, Zhiyoong Foo, David Blaauw, et al. A millimeter-scale energy-autonomous sensor system with stacked battery and solar cells. *IEEE Journal of Solid-State Circuits*, 48(3):801–813, 2013.

[24] Harald T Friis. A note on a simple transmission formula. *Proceedings of the IRE*, 34(5):254–256, 1946.

[25] Sami Gabriel, RW Lau, and Camelia Gabriel. The dielectric properties of biological tissues: Iii. parametric models for the dielectric spectrum of tissues. *Physics in Medicine & Biology*, 41(11):2271, 1996.

[26] Kaushik Gala, David Blaauw, Junfeng Wang, Vladimir Zolotov, and Min Zhao. Inductance 101: Analysis and design issues. In *Design Automation Conference, 2001. Proceedings*, pages 329–334. IEEE, 2001.

[27] HM Greenhouse. Design of planar rectangular microelectronic inductors. *IEEE Transactions on parts, hybrids, and packaging*, 10(2):101–109, 1974.

[28] Ali Hajimiri and Thomas H Lee. Design issues in cmos differential lc oscillators. *IEEE Journal of Solid-State Circuits*, 34(5):717–724, 1999.

[29] Sang Wook Han. Wireless interconnect using inductive coupling in 3d-ics. 2012.

[30] Cheng-Ru Ho and Mike Shuo-Wei Chen. A fractional-n dpll with calibration-free multi-phase injection-locked tdc and adaptive single-tone spur cancellation scheme. *IEEE Transactions on Circuits and Systems I: Regular Papers*, 63(8):1111–1122, 2016.

[31] John S Ho, Alexander J Yeh, Evgenios Neofytou, Sanghoek Kim, Yuji Tanabe, Bhagat Patlolla, Ramin E Beygui, and Ada SY Poon. Wireless power transfer to deep-tissue microimplants. *Proceedings of the National Academy of Sciences*, 111(22):7974–7979, 2014.

[32] Cletus Hoer and YC Love. Exact inductance equations for rectangular conductors with applications to more compli-cated geometries. *J. Res. Nat. Bureau Standards-C. Eng. Instrum.*, 69(2):127–137, 1965.

[33] Antoni Ivorra, Laura Becerra-Fajardo, and Quim Castellví. In vivo demonstration of injectable microstimulators based on charge-balanced rectification of epidermically applied currents. *Journal of neural engineering*, 12(6):066010, 2015.

[34] Seokhyeon Jeong, Yu Chen, Taekwang Jang, Julius Ming-Lin Tsai, David Blaauw, Hun-Seok Kim, and Dennis Sylvester. Always-on 12-nw acoustic sensing and object recognition microsystem for unattended ground sensor nodes. *IEEE Journal of Solid-State Circuits*, 53(1):261–274, 2018.

[35] Wanyeong Jung, Junhua Gu, Paul D Myers, Minseob Shim, Seokhyeon Jeong, Kaiyuan Yang, Myungjoon Choi, ZhiYoong Foo, Suyoung Bang, Sechang Oh, et al. 8.5 a 60%-efficiency 20nw-500μw tri-output fully integrated power management unit with environmental adaptation and load-proportional biasing for iot systems. In *Solid-State Circuits Conference (ISSCC), 2016 IEEE International*, pages 154–155. IEEE, 2016.

[36] Wanyeong Jung, Sechang Oh, Suyoung Bang, Yoonmyung Lee, Dennis Sylvester, and David Blaauw. 23.3 a 3nw fully integrated energy harvester based on self-oscillating switched-capacitor dc-dc converter. In *Solid-State Circuits Conference Digest of Technical Papers (ISSCC), 2014 IEEE International*, pages 398–399. IEEE, 2014.

[37] Gyouho Kim, Yoonmyung Lee, Zhiyoong Foo, Pat Pannuto, Ye-Sheng Kuo, Ben Kempke, Mohammad Hassan Ghaed, Suyoung Bang, Inhee Lee, Yejoong Kim, et al. A millimeter-scale wireless imaging system with continuous motion detection and energy harvesting. In *VLSI Circuits Digest of Technical Papers, 2014 Symposium on*, pages 1–2. IEEE, 2014.

[38] Hyeongseok Kim, Nikolaos Chiotellis, Elnaz Ansari, Muhammad Faisal, Taekwang Jang, Anthony Grbic, Hun-Seok Kim, David Blaauw, and David Wentzloff. A receiver/antenna co-design for a 1.5 mj per fix fully-integrated 10× 10× 6mm 3 gps logger. In *Custom Integrated Circuits Conference (CICC), 2018 IEEE*, pages 1–4. IEEE, 2018.

[39] Ye-sheng Kuo, Pat Pannuto, Gyouho Kim, Zhiyoong Foo, Inhee Lee, Ben Kempke, Prabal Dutta, David Blaauw, and Yoonmyung Lee. Mbus: A 17.5 pj/bit/chip portable interconnect bus for millimeter-scale sensor systems with 8 nw standby power. In *Custom Integrated Circuits Conference (CICC), 2014 IEEE Proceedings of the*, pages 1–4. IEEE, 2014.

[40] In Hee Lee. Power management circuits for miniature sensor systems. 2014.

[41] Inhee Lee, Yoonmyung Lee, Dennis Sylvester, and David Blaauw. Low power battery supervisory circuit with adaptive battery health monitor. In *VLSI Circuits Digest of Technical Papers, 2014 Symposium on*, pages 1–2. IEEE, 2014.

[42] Inhee Lee, Dennis Sylvester, and David Blaauw. A constant energy-per-cycle ring oscillator over a wide frequency range for wireless sensor nodes. *IEEE journal of solid-state circuits*, 51(3):697–711, 2016.

[43] Yoonmyung Lee, Bharan Giridhar, Zhiyoong Foo, Dennis Sylvester, and David Blaauw. A 660pw multi-stage temperature-compensated timer for ultra-low-power wireless sensor node synchronization. In *Solid-State Circuits Conference Digest of Technical Papers (ISSCC), 2011 IEEE International*, pages 46–48. IEEE, 2011.

[44] Yoonmyung Lee, Gyouho Kim, Suyoung Bang, Yejoong Kim, Inhee Lee, Prabal Dutta, Dennis Sylvester, and David Blaauw. A modular 1mm 3 die-stacked sensing platform with optical communication and multi-modal energy harvesting. In *Solid-State Circuits Conference Digest of Technical Papers (ISSCC), 2012 IEEE International*, pages 402–404. IEEE, 2012.

[45] Yao-Hong Liu, Christian Bachmann, Xiaoyan Wang, Yan Zhang, Ao Ba, Benjamin Busze, Ming Ding, Pieter Harpe, Gert-Jan van Schaik, Georgios Selimis, et al. 13.2 a 3.7 mw-rx 4.4 mw-tx fully integrated bluetooth low-energy/ieee802. 15.4/proprietary soc with an adpll-based fast frequency offset compensation in 40nm cmos. In *Solid-State Circuits Conference-(ISSCC), 2015 IEEE International*, pages 1–3. IEEE, 2015.

[46] Gerald E Loeb, Raymond A Peck, William H Moore, and Kevin Hood. Bion system for distributed neural prosthetic interfaces. *Medical Engineering and Physics*, 23(1):9–18, 2001.

[47] Michael Mark, Yuhui Chen, Christopher Sutardja, Chongxuan Tang, Suraj Gowda, Mark Wagner, Dan Werthimer, and Jan Rabaey. A 1mm 3 2mbps 330fj/b transponder for implanted neural sensors. In *VLSI Circuits (VLSIC), 2011 Symposium on*, pages 168–169. IEEE, 2011.

[48] Keith Mathieson, James Loudin, Georges Goetz, Philip Huie, Lele Wang, Theodore I Kamins, Ludwig Galambos, Richard Smith, James S Harris, Alexander Sher, et al. Photovoltaic retinal prosthesis with high pixel density. *Nature photonics*, 6(6):391, 2012.

[49] Patrick P Mercier, Saurav Bandyopadhyay, Andrew C Lysaght, Konstantina M Stankovic, and Anantha P Chandrakasan. A sub-nw 2.4 ghz transmitter for low data-rate sensing applications. *IEEE journal of solid-state circuits*, 49(7):1463–1474, 2014.

[50] Patrick P Mercier, Andrew C Lysaght, Saurav Bandyopadhyay, Anantha P Chandrakasan, and Konstantina M Stankovic. Energy extraction from the biologic battery in the inner ear. *Nature biotechnology*, 30(12):1240, 2012.

[51] Rikky Muller, Hanh-Phuc Le, Wen Li, Peter Ledochowitsch, Simone Gambini, Toni Bjorninen, Aaron Koralek, Jose M Carmena, Michel M Maharbiz, Elad Alon, et al. 24.1 a miniaturized 64-channel 225μw wireless electrocorticographic neural sensor. In *Solid-State Circuits Conference Digest of Technical Papers (ISSCC), 2014 IEEE International*, pages 412–413. IEEE, 2014.

[52] Pavel V Nikitin, KVS Rao, and Steve Lazar. An overview of near field uhf rfid. In *RFID, 2007. IEEE International Conference on*, pages 167–174. IEEE, 2007.

[53] Sechang Oh, Yao Shi, Gyouho Kim, Yejoong Kim, Taewook Kang, Seokhyeon Jeong, Dennis Sylvester, and David Blaauw. A 2.5 nj duty-cycled bridge-to-digital converter integrated in a 13mm 3 pressure-sensing system. In *Solid-State Circuits Conference-(ISSCC), 2018 IEEE International*, pages 328–330. IEEE, 2018.

[54] Arun Paidimarri, Nathan Ickes, and Anantha P Chandrakasan. 13.7 a+ 10dbm 2.4 ghz transmitter with sub-400pw leakage and 43.7% system efficiency. In *Solid-State Circuits Conference-(ISSCC), 2015 IEEE International*, pages 1–3. IEEE, 2015.

[55] Arun Paidimarri, Nathan Ickes, and Anantha P Chandrakasan. A+ 10 dbm ble transmitter with sub-400 pw leakage for ultra-low duty cycles. *IEEE Journal of Solid-State Circuits*, 51(6):1331–1346, 2016.

[56] Ronald Pethig and Douglas B Kell. The passive electrical properties of biological systems: their significance in physiology, biophysics and biotechnology. *Physics in Medicine & Biology*, 32(8):933, 1987.

[57] Jan Prummel, Michail Papamichail, John Willms, Rahul Todi, William Aartsen, Wim Kruiskamp, Johan Haanstra, Enno Opbroek, Søren Rievers, Peter Seesink, et al. A 10 mw bluetooth low-energy transceiver with on-chip matching. *IEEE Journal of Solid-State Circuits*, 50(12):3077–3088, 2015.

[58] P Series. Propagation data and prediction methods for the planning of indoor radiocommunication systems and radio local area networks in the frequency range 900 mhz to 100 ghz. *Recommendation ITU-R*, pages 1238–7, 2012.

[59] Yao Shi, Myungjoon Choi, Ziyun Li, Gyouho Kim, Zhiyoong Foo, Hun-Seok Kim, David Wentzloff, and David Blaauw. 26.7 a 10mm3 syringe-implantable near-field radio system on glass substrate. In *Solid-State Circuits Conference (ISSCC), 2016 IEEE International*, pages 448–449. IEEE, 2016.

[60] Atsushi Shirane, Yiming Fang, Haowei Tan, Taiki Ibe, Hiroyuki Ito, Noboru Ishihara, and Kazuya Masu. Rf-powered transceiver with an energy-and spectral-efficient if-based quadrature backscattering transmitter. *IEEE Journal of Solid-State Circuits*, 50(12):2975–2987, 2015.

[61] Robert Bogdan Staszewski and Poras T Balsara. *All-digital frequency synthesizer in deep-submicron CMOS*. John Wiley & Sons, 2006.

[62] Warren L Stutzman and Gary A Thiele. *Antenna theory and design*. John Wiley & Sons, 2012.

[63] Maryam Tabesh, Nemat Dolatsha, Amin Arbabian, and Ali M Niknejad. A power-harvesting pad-less millimeter-sized radio. *IEEE Journal of Solid-State Circuits*, 50(4):962–977, 2015.

[64] Philip R Troyk. Injectable electronic identification, monitoring, and stimulation systems. *Annual Review of Biomedical Engineering*, 1(1):177–209, 1999.

[65] Brett Warneke, Matt Last, Brian Liebowitz, and Kristofer SJ Pister. Smart dust: Communicating with a cubic-millimeter computer. *Computer*, 34(1):44–51, 2001.

[66] Brett A Warneke and Kristofer SJ Pister. An ultra-low energy microcontroller for smart dust wireless sensor networks. In *Solid-State Circuits Conference, 2004. Digest of Technical Papers. ISSCC. 2004 IEEE International*, pages 316–317. IEEE, 2004.

[67] Alan Wong, Mark Dawkins, Gabriele Devita, Nick Kasparidis, Andreas Katsiamis, Oliver King, Franco Lauria, Johannes Schiff, and Alison Burdett. A 1v 5ma multimode ieee 802.15. 6/bluetooth low-energy wban transceiver for biotelemetry applications. In *Solid-State Circuits Conference Digest of Technical Papers (ISSCC), 2012 IEEE International*, pages 300–302. IEEE, 2012.

[68] Xiao Wu, Yao Shi, Supreet Jeloka, Kaiyuan Yang, Inhee Lee, Yoonmyung Lee, Dennis Sylvester, and David Blaauw. A 20-pw discontinuous switched-capacitor energy harvester for smart sensor applications. *IEEE Journal of Solid-State Circuits*, 52(4):972–984, 2017.

[69] Anatoly Yakovlev, Ji Hoon Jang, and Daniel Pivonka. An 11 μw sub-pj/bit reconfigurable transceiver for mm-sized wireless implants. *IEEE transactions on biomedical circuits and systems*, 10(1):175–185, 2016.

[70] Jun Yin, Shiheng Yang, Haidong Yi, Wei-Han Yu, Pui-In Mak, and Rui P Martins. A 0.2 v energy-harvesting ble transmitter with a micropower manager achieving 25% system efficiency at 0dbm output and 5.2 nw sleep power in 28nm cmos. In *Solid-State Circuits Conference-(ISSCC), 2018 IEEE International*, pages 450–452. IEEE, 2018.

[71] Fan-Gang Zeng, Stephen Rebscher, William Harrison, Xiaoan Sun, and Haihong Feng. Cochlear implants: system design, integration, and evaluation. *IEEE reviews in biomedical engineering*, 1:115–142, 2008.

[72] Babak Ziaie, Mark D Nardin, Anthony R Coghlan, and Khalil Najafi. A single-channel implantable microstimulator for functional neuromuscular stimulation. *IEEE Transactions on Biomedical Engineering*, 44(10):909–920, 1997.